RECEIVER FUNCTION ANALYSIS OF CRUSTAL AND UPPER MANTLE STRUCTURE BENEATH SOUTHERN AFRICA

Submitted in fulfillment of the requirements for the degree of

Master of Science,

University of Cape Town

Jacek Maciej Stankiewicz

February 2001

Receiver function analysis of crustal and upper mantle structure beneath Southern Africa.

Jacek Maciej Stankiewicz

A dissertation submitted to the Department of Geological Sciences,
University of Cape Town,
In fulfillment of the requirements for the Degree of Master of Science

Abstract

The technique of receiver functions is used to identify converted phases of seismic waves from teleseismic events. These phases are then used to study the variations of crustal thickness and upper mantle discontinuities beneath southern Africa.

The seismic data used in the study comes from the 82 broadband stations that comprise the regional array deployed in southern Africa from April 1997 to April 1999, as well as from a dense array of 32 stations near Kimberley. The latter was in operation for 7 months, starting in December 1998.

Arrival times for phases converted at the Moho are used to determine crustal thickness. The Moho depth in the south-western section of the craton was found to vary between 37 and 40km, except for one station that recorded a depth of 43km (SA23). Further north along the western block of the craton (into Botswana) the depth increases up to 43km. The depth increases even further in the north-eastern section of the craton, where results vary from 40 to 52km. Just north of the Kaapvaal craton, in the neighbouring Zimbabwe craton, the crustal thickness drops significantly. The results obtained there varied from 36 to 40km.

For the Kimberley area, using the dense array, the Moho depth was found to be 37.3 ± 1.5 km. Following that, arrivals of the Ps and Ppps phases were used to determine the Poisson's ratio in the region. This was found to have a

value of 0.264 ± 0.007, slightly larger than 0.25 expected for a perfectly elastic solid.

Arrivals of phases from the 410- and the 660-km mantle discontinuities are used to interpret the relative positions of these discontinuities, as well for comparison of the mantle temperatures and seismic velocities in the region to the global averages.

In the Kimberley area the 410- and 660-km discontinuities were found at their expected depths, and this implied the mantle temperature in the region is close to the global average. The seismic velocities in the region were found up to 5% faster than the averages from the global IASP91 model, which is fast even by Precambrian standards.

In other sections of the Kaapvaal craton the velocities remain faster than global averages, but not as fast as beneath Kimberley. In these sections the '410' is also slightly elevated, while the '660' is depressed, which implies a slightly low mantle temperature relative to the global average.

The technique of beamforming, used to study surface waves, is introduced using the Kimberley array. Two Rayleigh waves were identified in the signal, and their directions of propagation and particle motions were analyzed. These could be used for studies of anisotropy or surface wave tomography.

Acknowledgements

I would like to thank Prof. Maarten de Wit for supervising this project, his continued interest in my work, guidance and advice.

I was introduced to the Kaapvaal craton project by Dr Moctar Doucouré and Dr Marian Tredoux, and since then they were very involved in my research, as was Prof. Rod Green, with whom I had many valuable discussions.

During the course of my study I was very fortunate to work with scientists at institutions in the United States of America. For that I would like to extend my gratitude to the following:

Dr David James, Dr Paul Silver and Dr Steve Gao at the Carnegie Institution of Washington and

Prof. Rob van der Hilst, Dr Sébastien Chevrot and Dr Frederik Simons at the Massachusetts Institute of Technology.

Financial support for this thesis has been provided by the National Research Foundation, while the logistics for the above mentioned trips to the USA were taken care of by Prof. de Wit, Dr James and Prof. van der Hilst, as well as the US National Science Foundation.

Lastly I would like to thank my parents for their support and encouragement, and all my friends from the University of Cape Town Mountain & Ski Club for helping me remain sane during the course of this study.

Table of Contents

List of Figures

7.3. P-S conversion depth stack using the 4 events.

7.4. Crustal thickness and Vp/Vs calculation graph for the event from:
a) 99087; b) 99093; c) 99126.

7.5. S-P conversion depth stack using the 4 events.

8.1. Q-components of individual traces of the 99063 event showing the consistent long period noise.

8.2 Response of the Kimberley array.

8.3 Power spectrum of the pre-P arrival signal of the 99063 event.

The following figures were constructed using General Mapping Tools (GMT) developed by Wessel & Smith (1991, 1995a, 1995b, 1998):
2.1, 2.2, 3.1, 3.2, 5.1, 5.2, 5.3, 6.1, 6.2, 6.3, 6.4, 6.5, 7.1.

Chapter 1

The Kaapvaal Craton Project

1.1 Introduction to Southern Africa's geology

Southern Africa is blessed with a rich geologic record of the Early Earth. Clues to the origin of Earth's earliest continents are stored in the Kaapvaal craton (discussed in detail in Chapter 2), the foundations of which were constructed before 3500 million years ago (Tankard *et al.* 1982). By the end of the Archean (2500 Ma) this continental fragment covered an area of at least 1.2 million km^2, and was underlain by a cratonic mantle root of unusual geochemistry down to at least 250 km. By all accounts, the Kaapvaal craton is a small remnant of one of Earth's oldest continents.

The surface geology of the Kaapvaal craton is well known. Unfortunately the same cannot be said for the geology at depth. Kimberlites and their entrained mineral, crustal and mantle xenoliths have provided exciting glimpses of the craton's deep secrets. But ultimately seismic probing is needed to unravel the third dimension; and extensive modern geochronology is necessary to track the fourth, its development through deep time.

1.2 The Kaapvaal craton project

In 1996, a major interdisciplinary, multi-institutional project was started to investigate the origin and evolution of the Kaapvaal craton (Carlson *et al.* 1996, 2000). The central goal of this project is to produce a tomographic image of the deep lithospheric roots of the craton. The major institutions

participating in the project are Carnegie Institution of Washington, Massachusetts Institute of Technology, Cambridge, University of Cape Town, University of Witwatersrand, University of Botswana and University of Zimbabwe.

To help achieve the objectives of the project, in April 1997, portable broadband seismometers were deployed and placed in an array of 82 recording sites along a SW-NE axis from Cape Town to Harare. Over the next 2 years natural teleseismic events and local mine-induced seismic activity were monitored. In addition a closely spaced array of 32 stations was deployed around Kimberley in December 1998 for a period of 7 months. Both these arrays are discussed in detail in Chapter 3.

A large number of crustal and mantle geology, geochemistry and geophysical projects are linked to this project.

Geoscientists involved in these projects meet every year to discuss their results. These meetings were held in Cape Town (1996), Pretoria (1997), Kimberley (1998), Vredefort (1999) and Gaborone (2000). For 2001 a meeting in Boston is planned. Further information about the project can be found on the internet, either on the Carnegie Institution website (www.ciw.edu/kaapvaal), or on that of the UCT Centre for Interactive and Graphical Computing of Earth Systems (www.uct.ac.za/depts/cigces).

1.3 This thesis and the Kaapvaal project

Along with the projects mentioned in the preceding sections, a number of postgraduate theses at South African universities are being funded by the National Research Foundation.

This thesis is one of them, and is connected to one of the geophysical projects I have been involved with since 1997. It aims to examine geological

discontinuities in the Earth's crust and upper mantle beneath the craton by studying the seismic waves that pass through or are deflected from these discontinuities.

1.4 The African superswell

Southern Africa is abnormally elevated (Nyblade & Robinson 1994). Average elevation of most cratons worldwide is between 400 and 500 meters above sea level, yet the craton of southern Africa lies more than 1 km above sea level. This region of elevated topography, termed locally the South African Highveld, extends to the surrounding oceans, which possess residual bathymetry in excess of 500 meters.

The origin of continental and oceanic swells has received considerable attention over the past 2 decades. There are many possible causes for the uplift. A number of isostatic mechanisms, some related to the unique chemistry of the craton, have been reviewed (McGetchin *et al.* 1980) and the dynamic support of uplifted regions has been investigated (e.g. McNutt & Judge 1990). It is difficult to argue convincingly for any of the possible interpretations for the superswell – indeed, it could be a result of a combination of different mechanisms. However, several observations in the Tanzania craton region suggest that such superswell may be connected to the heating of the lithosphere (Nyblade *et al.* 1990; Nyblade & Pollack 1993).

From a comparison of heat flow in southern Africa to the global averages from similarly aged terrains (table 1.1) it is clear that there exists a positive heat flow anomaly. Heat flow observations from the southeastern Atlantic Ocean also suggest thermal perturbations beneath this area of the superswell (Stein & Stein 1992).

Table 1.1

Heat flow in southern Africa compared to global averages

Archean terrains	**Heat Flow (mW/m^2)**	**Reference**
Global average	41 +/- 1	Nyblade & Pollack 1993
Southern Africa	47 +/- 2	Nyblade *et al.* 1990
Proterozoic terrains		
Global average	55 +/- 1	Nyblade & Pollack 1993
Southern Africa	64 +/- 3	Nyblade *et al.* 1990

The high values for heat flow do not necessarily imply a heated lithosphere, although this has sometimes been assumed in the past. Morgan (1982) combined this with the fact that Southern Africa moved across several hotspots during the Mesozoic to suggest that the superswell is connected to the supposedly heated lithosphere.

A breakthrough in understanding the anomalous heat flow came from the studies of the flow in the Witwatersrand Basin and the Vredefort structure (e.g. Hart 1978; Nicolaysen *et al.* 1981; Welke & Nicolaysen 1981, Jones 1988). These studies found that the excessive heat production comes from the crust, and not from the asthenosphere. Nicolaysen *et al.* (1981) computed the average heat generation in the crust as a function of depth, and found that at 30 km the value is about 0.1 $\mu W/m^3$, which is a very significant drop from the 1.5 $\mu W/m^3$ produced just in the upper crust (<20km). Jones & Bottomley (1986) studied the rock temperatures in the Witwatersrand mining arc, and found these much higher than expected. All this suggests that the high heat flow across the Kaapvaal craton is due to the properties of the crust, and not necessarily the asthenosphere. In fact, if the upper mantle temperatures were unusually high, the conditions would not be conducive to preservation of old

diamonds in the mantle keel of the Kaapvaal craton (Jones 1988). The excess heat flow is now attributed to the radioactivity of the high uranium content of the upper crust (Nicolaysen *et al.* 1981).

There also exists deep mantle support for the African Superswell. It has been suggested that the excess elevation is due to an active upwelling of hot mantle material in the lower mantle, originating from the core-mantle boundary (Lithgow-Bertelloni & Silver 1998). This flow would extend all the way to the base of the African plate, where it would elevate the southern part of the continent. This upwelling can be inferred from the low velocity anomalies imaged by seismic topography. To test this suggestion an 'instantaneous flow' calculation has been performed to predict both the mantle flow that would develop from the buoyant lower-mantle feature, and the resulting dynamic topography of the Earth's surface (Lithgow-Bertelloni & Silver 1998). The calculated pattern of surface topography resembled very closely the actual topography of southern Africa.

Further testing of these hypotheses is one of the main objectives of the Kaapvaal craton project. A closer understanding of the composition and structure of the upper mantle below South Africa is a prerequisite for such tests. This thesis examines some of the internal structure of this upper (lithospheric) mantle.

Chapter 2

The Kaapvaal Craton

2.1 Archean age rocks

Granite-greenstone assemblages of Archean age have been found on all continents. They are usually subdivided according to their age into Late Archean (2.5 – 3.0 Ga) and Early Archean (3.0 – 4.0 Ga) and represent remnants of Earth's earliest preserved continents (de Wit 1998).

Globally, well preserved Late Archean crust accounts for just 7% of the exposed continental surface area, while the corresponding value for Early Archean rocks is just about 0.5% (the actual areas are $11 \cdot 10^6$ km^2 and $0.8 \cdot 10^6$ km^2 respectively). This means there is relatively little rock record from which to reconstruct the workings of the early Earth (de Wit 1998), and none from the first $500 \cdot 10^6$ years of its evolution (no terrestrial rock older than 4.1 Ga has ever been found on Earth).

2.2 Archean cratons

The Archean rocks described above exist in only about 10 small kernels embedded within the lithosphere of the present continents. These kernels are known as Archean cratons. Many of the cratons consist predominantly of granite-greenstone sequences formed in the Late Archean (de Wit *et al.* 1992). The areas with older history (the Early Archean) have generally been deformed and metamorphosed, losing much of their original character. The only regions that have retained substantial portions of pristine Early Archean

rocks are the Kaapvaal craton in Southern Africa and the much smaller Pilbara craton of northwest Australia.

The table below shows a summary of the data from selected Archean cratons (from de Wit 1998; Kopylova *et al* 1999; Bostock & Cassidy 1997):

Table 2.1

Summarized data for selected Archean cratons

Craton	Location	Area [$*10^6 km^2$]	Age (%) (peak in Ga) Early Arch. Late Arch.
Kaapvaal	South Africa	1.20	60(3.6-3.2); 40(2.6-3.0)
Pilbara	Australia	0.06	90(3.6-3.1); 10(2.8-3.0)
Superior	Canada	1.57	10(3.0-3.3); 90(2.7-2.8)
Yilgarn	Australia	1.00	10(3.7-3.3); 70(2.6-2.8); 20(2.8-3.0)
Sao Francisco	Brazil	0.82	30(3.0-3.5); 50(2.7-2.9); 20(1.9-2.1)
Zimbabwe	Zimbabwe	0.27	10(3.0-3.3); 90(2.6-2.7)
Slave	Canada	0.15	Dominated by 2.6-2.7Ga rocks, but contains oldest terrestrial rocks found (~ 4.1Ga)

It is clear that the Kaapvaal craton is the oldest reasonably sized piece of Archean continental crust that has been well preserved.

2.3 Regional framework of the Kaapvaal craton

The Kaapvaal craton covers an area of about $1.2*10^6$ km^2 (Figure 2.1). While the limits have been largely defined by geological mapping,

geophysics and image processing have further helped in locating the exact boundaries of the craton (e.g. Corner 1991). To the north it is bounded by the Limpopo belt, which separates the Kaapvaal and Zimbabwe cratons. To the west and south it borders with the mobile Mesoproterozoic Natal-Namaqua belts; and to the east with the Lebombo monocline of Jurassic volcanics associated with the break-up of Gondwana (de Wit *et al.* 1992).

Seismologists have made contributions to defining the framework of the craton by studying waveforms passing through the craton in order to determine its 3-D structure (tomography studies). The aim of this thesis is to perform a similar study, and therefore only a quick overview of the depth phenomena will be given in this section.

Cratons have a crust of granitic composition, which is underlain by a relatively stiff mantle component. Together the two layers are referred to as the continental lithosphere; the mantle component is referred to as the lithospheric mantle, in contrast to the more mobile asthenospheric mantle beneath it (Jordan 1975).

Results obtained so far suggest that the depth to the base of the crust of the surrounding Natal-Namaqua Proterozoic belt is greater than that of the craton, and also contains a substantially higher portion of the intermediate velocity crustal rocks (Green & Durheim 1990).

Velocity inversions show that the seismic velocities beneath the Kaapvaal craton in the depth range from 50 up to 300-350km are substantially greater than the global average – from this it can be concluded that this is in fact the maximum depth of the lithospheric mantle of the craton (Vinnik *et al.* 1996a, 1996b). This is consistent with the association of other cratons with high-velocity anomalies extending to the depth of 300-400km (the tectosphere of Jordan 1975, 1988). Recent seismic data give reasons to

believe that the root of the Kaapvaal craton may actually come closer to 400km (Vinnik *et al.* 1996a, 1996b). The limited seismological data, together with mantle xenoliths brought to the surface by kimberlites, provides a glimpse of what appears to be a very complex lithospheric keel with an extended evolutionary history (Boyd 1989; de Wit 1998; Carlson *et al.* 2000). Figure 2.2 shows a schematic cross section of the craton with the above-mentioned features, constructed from the data prior to the Kaapvaal Craton seismic experiment.

Below the craton velocity "jumps" across the 410- and the 660-km discontinuities in the asthenospheric upper mantle are expected. These two discontinuities are found (at slightly varying depths) under the continents throughout the Earth, and are believed to be caused primarily by phase changes in olivine (from α to β spinel) and other minerals, that result from the increasing pressure and temperature with increasing depth (e.g. Katsura & Ito 1989; Ito & Takahashi 1989). These changes will be discussed in greater detail in chapter 6. Detection of these discontinuities and determining their precise depths underneath the craton are also the aims of this project.

The craton can be subdivided geologically into a number of Archean subdomains. The oldest of these occur in the eastern region of the craton: the Ancient Gneiss terrain and the southern Barberton terrain (see Figure 2.1). The comagmatic mafic and ultramafic rocks of the southern Barberton region represent a remnant of very early oceanic lithosphere (~3.5Ga), while the Ancient Gneiss terrain contains continental tonalitic rocks up to the age of 3.65 Ga (de Wit *et al.* 1992).

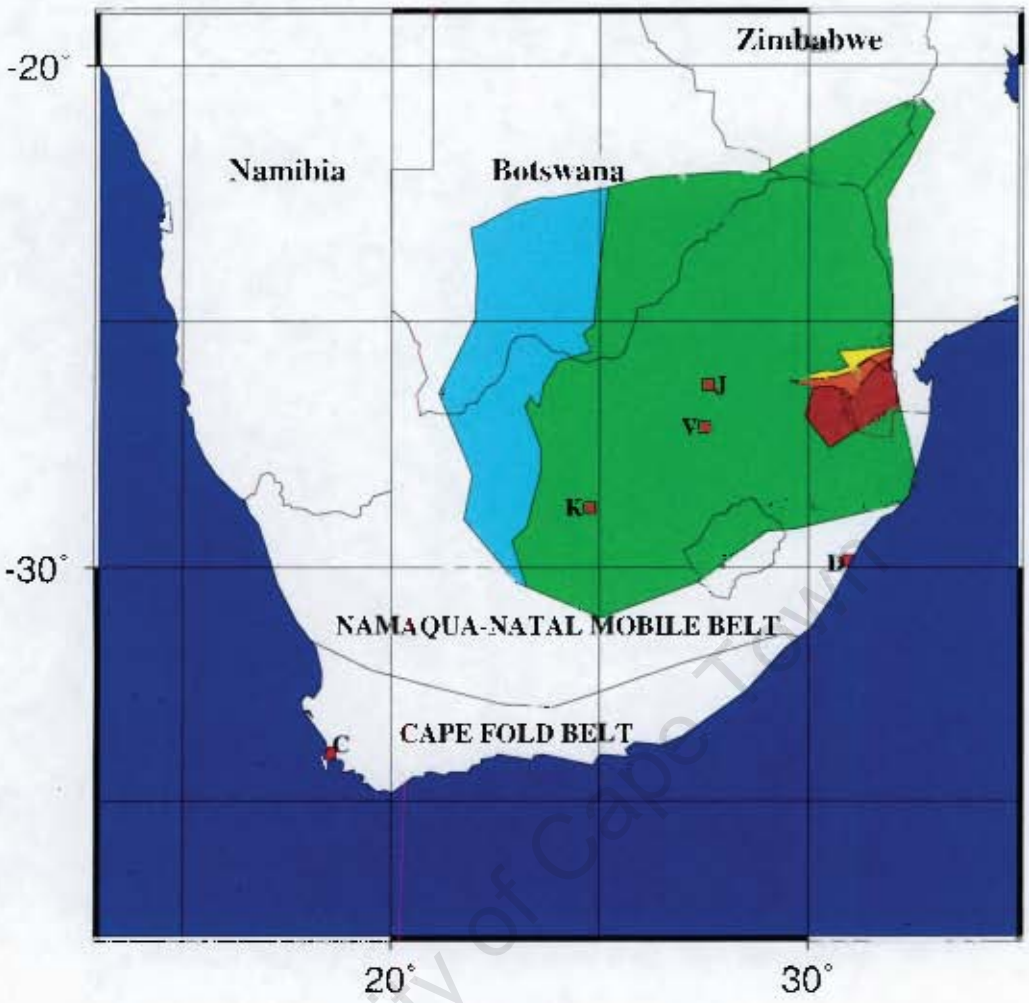

Fig 2.1

Map of Southern Africa illustrating the location of the Kaapvaal craton (blue and green). The blue area is the 'thin skinned' Proterozoic belt. In the east three subdomains mentioned in the text are shown: Northern Barberton terrain (yellow), Southern Barberton terrain (orange) and the Ancient Gneiss terrain (brown). As points of reference cities of Cape Town (C), Durban (D),Kimberley (K),Vredefort (V) and Johannesburg (J) are shown.

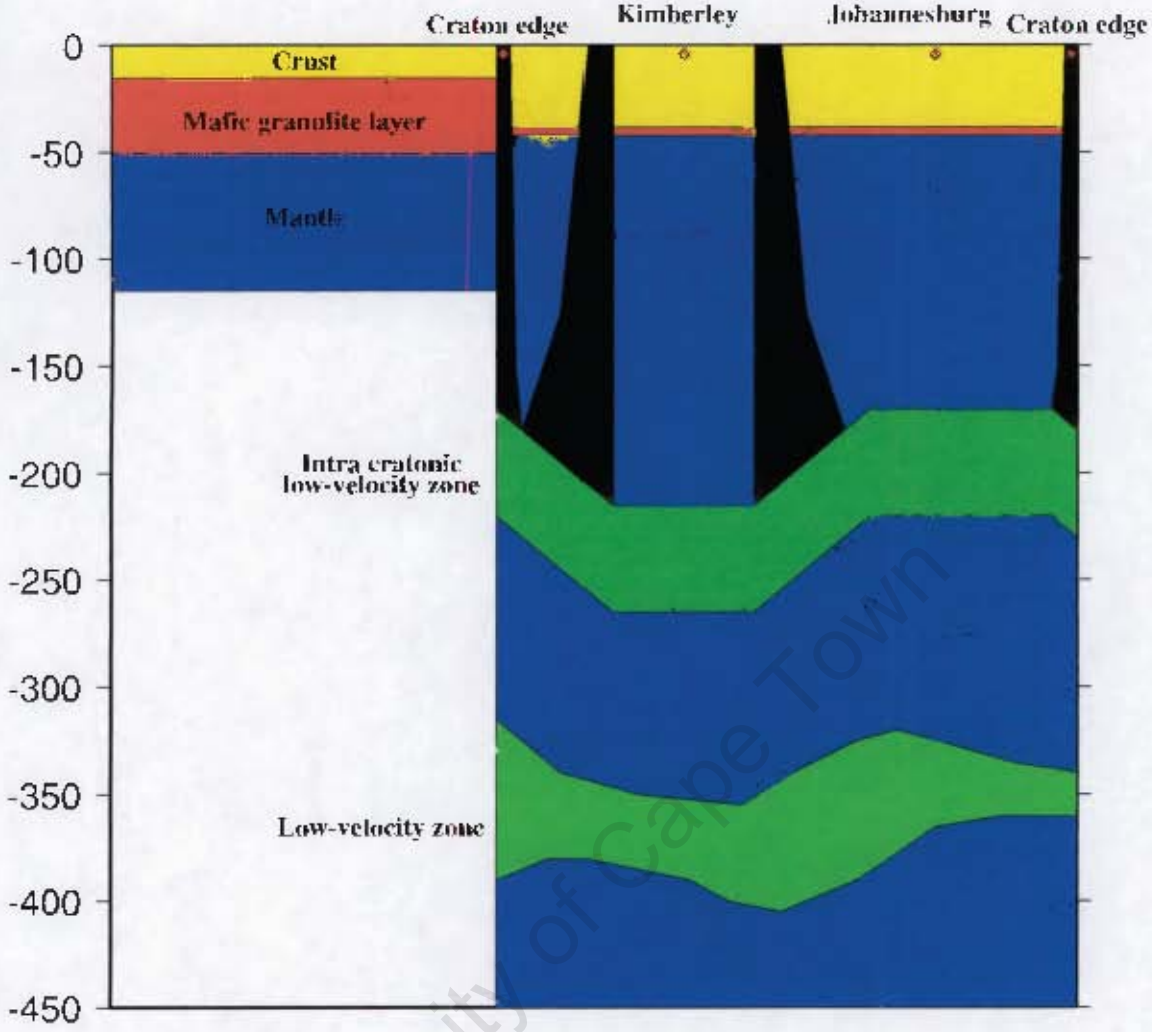

Fig 2.2

Schematic NE-SW cross-section of the Kaapvaal craton based on pre-Kaapvaal Project seismological and geological studies, compared to a section of the Natal-Namaqua belt to the left. Speculated deep shear zones are shown in black. Adapted from de Wit (1998) using data from Vinnik *et al.* (1995, 1996a).

2.4 Formation of the craton

There are essentially three competing models for the formation of Archean cratons, and they are illustrated in Figure 2.3. The first views the peridotitic component forming as high-pressure residues after extraction of komatiitic and basaltic lavas from the primitive Archean mantle (e.g. Boyd 1989). This process is thought to have taken place above rising mantle plumes that compressed the eclogites, leaving the extrusive rocks exposed in greenstone belts. Basalts that have been sunk below the surface have undergone the phase transition to eclogites at depth through this burial (see model 1 if Fig. 2.3).

The second model (de Wit *et al.* 1992) proposes that cratons were constructed during the subduction of Archean oceanic crust. This ancient crust contained a large ultramafic component, which was intensely hydrated, hence relatively buoyant. This Mg-rich lithosphere would have resisted a subduction-like process, leading instead to obduction-dominated tectonics. The nucleus of the Archean continent would therefore have formed through regional intraoceanic obduction, giving rise to stacking, tectonic loading, subsidence and secondary modification of the hydrated oceanic thrust stacks (see model 2 in Fig. 2.3).

The third model (e.g. Parman *et al.* 2001) views the craton lithosphere forming as low pressure residues above subduction zones similar to present day ones. It suggests that the accretion of eclogites and peridotites also occurred during Proterozoic accretion of subducted oceanic lithosphere (basalt), which metamorphosed to form the eclogites (see model 3 in Fig. 2.3).

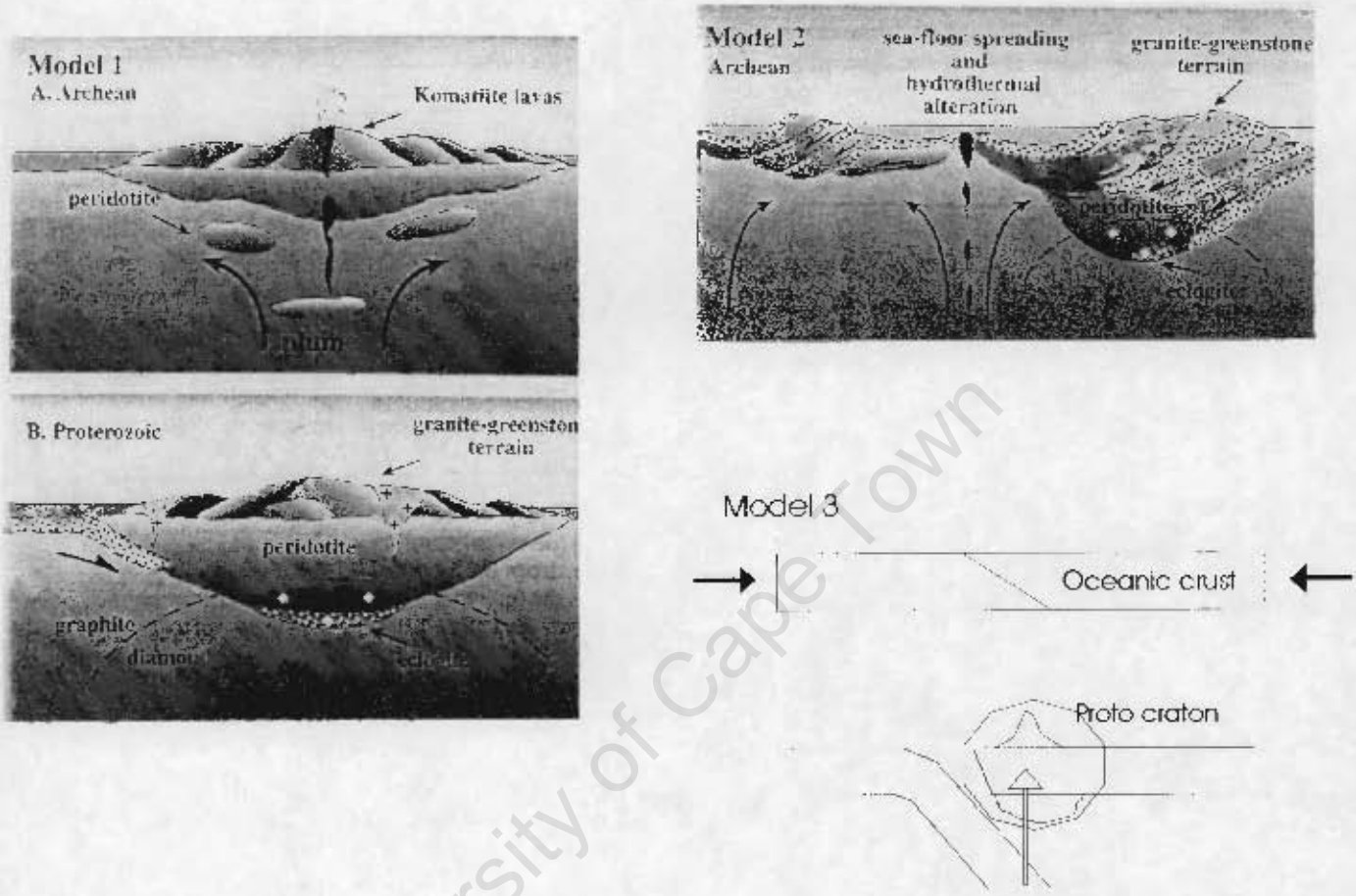

Fig 2.3

Schematic illustrations of the 3 models proposed for the formation of the craton. Models 1 and 2 taken from Hart *et al.* (1997); model 3 is after Parman *et al.* (2001).

2.5 Tectonic framework of the region

Since the stabilization of the Kaapvaal craton about 2.6 Ga ago, crustal blocks have accreted to and surrounded it during successive orogenic events. The Namaqua-Natal mobile belt formed in the early to middle Proterozoic during a series of tectonic events (Tankard *et al.* 1982). During these events oceanic crust was thrust across the Kaapvaal Craton as a series of nappe sheets (Matthews 1990). Tectonism ceased by 1.0 Ga when the Namaqua-Natal belt finally accreted to the craton forming the "Kalahari Shield" (Tankard *et al.* 1982).

During the late Precambrian, the blocks that assembled Gondwana were accreted together along Pan African mobile belts, such as the Saldanian rocks of the Cape region. Thereafter, the Cape Fold Belt and its adjacent geology formed over a period of ~250 Ma. The early Paleozoic was a period of extension which resulted in a rift which was covered by up to 8km of clastic sediments of the Cape Supergroup (Tankard *et al.* 1982). Compression occurred in Hercynian times (~250Ma) during a series of tectonic events that caused extensive folding, faulting and thrusting of the Cape sediments and the formation of the Cape fold mountains.

Extension process occurred again circa 200 – 120 Ma resulting in the final break up of Gondwana and the formation of southern oceans (Dingle *et al.* 1983). Relaxation of the southern margin of southern Africa is continuing today – the evidence for it can be seen in the numerous listric normal faults found striking east-west (e.g. Kango and Worcester faults) along the southern margins of South Africa (Harvey 1999). These faults are weak zones from previous tectonism and the formation of the Cretaceous basins in the area, and some are still active today, as evidenced by the Tulbach earthquake (6.8 on the Richter scale) in 1949 (Brown *et al* 1995).

Other areas where Mesozoic to Quaternary extension has occurred are the offshore Agulhas Ridge and Falklands Fracture Zones. These are both areas of enormous relief on the Indian Ocean. Recent experiments showed that on the Agulhas Ridge up to 1200m of sediments have deposited on a hummocky basement which itself is erosional. The nature of this basement is related to voluminous flood basalts attributed to mantle plumes in extensional regimes (Nyblade & Robinson 1994).

All this evidence suggests a long history of tectonic inversions along the southern margins of Southern Africa – this had a significant effect on the variation of the depth to the Moho discontinuity in this region (Harvey 1999).

Chapter 3

Distribution of Seismic Stations

3.1 The regional array of stations

When the Kaapvaal Seismic Project was initiated in April 1997, 55 broad band seismic stations were deployed across southern Africa in an approximately 1000km wide and 2000km long SW-NE axis from Cape Town to Harare. After one year, about two-thirds of the western-most stations were moved to the eastern part of the area and left for another year. This gave a total of 82 recording sites, separated from each other by about 100km, each of them being given a specific number. Throughout the project these stations are referred to as SA01 to SA82. The location of each site is given in table 3.1, and their distribution can be seen in figure 3.1. In this thesis these stations are used to determine the crustal thickness throughout southern Africa.

Stations SA06, SA21 and SA41 never recorded any activity due to technical problems.

3.2 The Kimberley array

In December 1998 an additional, detailed array of 32 stations was deployed around the Kimberley area for a period of 7 months. These stations are referred to as BB01 to BB32. They were placed much closer together (see Figure 3.2) than in the regional array (a few kilometers from each other), and

in this thesis are used to study details of the structure of the crust, as well as the upper mantle. Their arrangement is illustrated in Figure 3.2, while Table 3.2 shows the locations of each station. This array will be referred to as the Kimberley array.

3.3 Stations used in the Kaapvaal Craton Project

Each recording station has a fixed location and consists of three geophones orthogonal to each other. They record seismic events in the three basic directions: north-south, east-west and vertical. Thus the record of any seismic event will consist of three seismograms; labeled n, e and z after the direction of each.

The stations were designed, developed and produced by the STS-2 factory in Switzerland. The system was then standardized by Incorporated Research Institutions for Seismology (IRIS). The stations were operated on a continuous recording mode at 20sps. The data were archived at the IRIS DMC (Data Management Center), and event data were extracted from the continuous records using software developed by the DMC. These data were then converted to SAC format at Carnegie. The frequency band for the records was very broad – frequencies from as low as 0.008Hz up to 10Hz were recorded. This made it possible to analyze both high and low frequency signals by using high pass or low pass filters (filters are discussed in detail in section 4.6.1). The very low frequency records also enabled us to study surface waves (see chapter 8).

The technical design and the electronics involved are beyond the scope of this thesis, but the interested reader can consult the Carnegie Institution website on www.ciw.edu/kaapvaal, or that of IRIS on www.iris.edu.

Table 3.1

Station coordinates of the regional array

Station	Lat. S	Lon. E	Station	Lat. S	Lon. E	Station	Lat. S	Lon. E
SA01	34.294	19.246	SA30	27.072	24.165	SA58	23.518	31.397
SA02	33.735	20.266	SA31	26.995	25.021	SA59	24.837	24.464
SA03	33.632	21.335	SA32	26.865	26.285	SA60	23.852	24.959
SA04	32.851	19.621	SA33	26.899	27.179	SA61	23.948	24.022
SA05	32.605	21.535	SA34	26.814	28.099	SA62	24.851	25.135
SA07	31.978	20.226	SA35	27.018	29.088	SA63	23.658	26.082
SA08	31.910	22.073	SA36	26.877	30.125	SA64	22.969	26.202
SA09	30.922	22.986	SA37	25.971	23.721	SA65	22.818	27.222
SA10	30.972	23.914	SA38	25.933	25.085	SA66	21.900	26.373
SA11	29.965	20.947	SA39	25.895	26.151	SA67	21.886	27.274
SA12	29.849	22.253	SA40	25.898	27.149	SA68	21.950	28.188
SA13	29.979	23.140	SA42	25.665	29.222	SA69	22.305	29.266
SA14	29.868	24.023	SA43	25.787	30.067	SA70	21.088	26.335
SA15	29.902	25.031	SA44	26.032	30.902	SA71	20.926	27.141
SA16	28.950	22.195	SA45	24.879	26.164	SA72	20.143	28.611
SA17	28.932	23.226	SA46	24.838	27.109	SA73	21.854	30.278
SA18	28.633	24.306	SA47	24.847	28.162	SA74	21.923	30.936
SA19	28.906	24.833	SA48	24.895	29.216	SA75	20.860	28.999
SA20	29.022	26.195	SA49	24.960	30.309	SA76	20.636	29.846
SA22	27.966	22.009	SA50	23.872	27.166	SA77	20.756	30.919
SA23	27.930	23.405	SA51	23.863	28.157	SA78	19.467	30.772
SA24	27.883	24.236	SA52	23.798	28.897	SA79	20.021	30.517
SA25	27.846	25.126	SA53	24.113	29.333	SA80	19.959	31.318
SA26	27.545	26.180	SA54	23.729	30.668	SA81	30.925	21.268
SA27	27.862	27.294	SA55	22.980	28.298	SA82	30.977	22.247
SA28	27.898	28.066	SA56	23.006	29.074			
SA29	26.932	23.035	SA57	22.981	30.020			

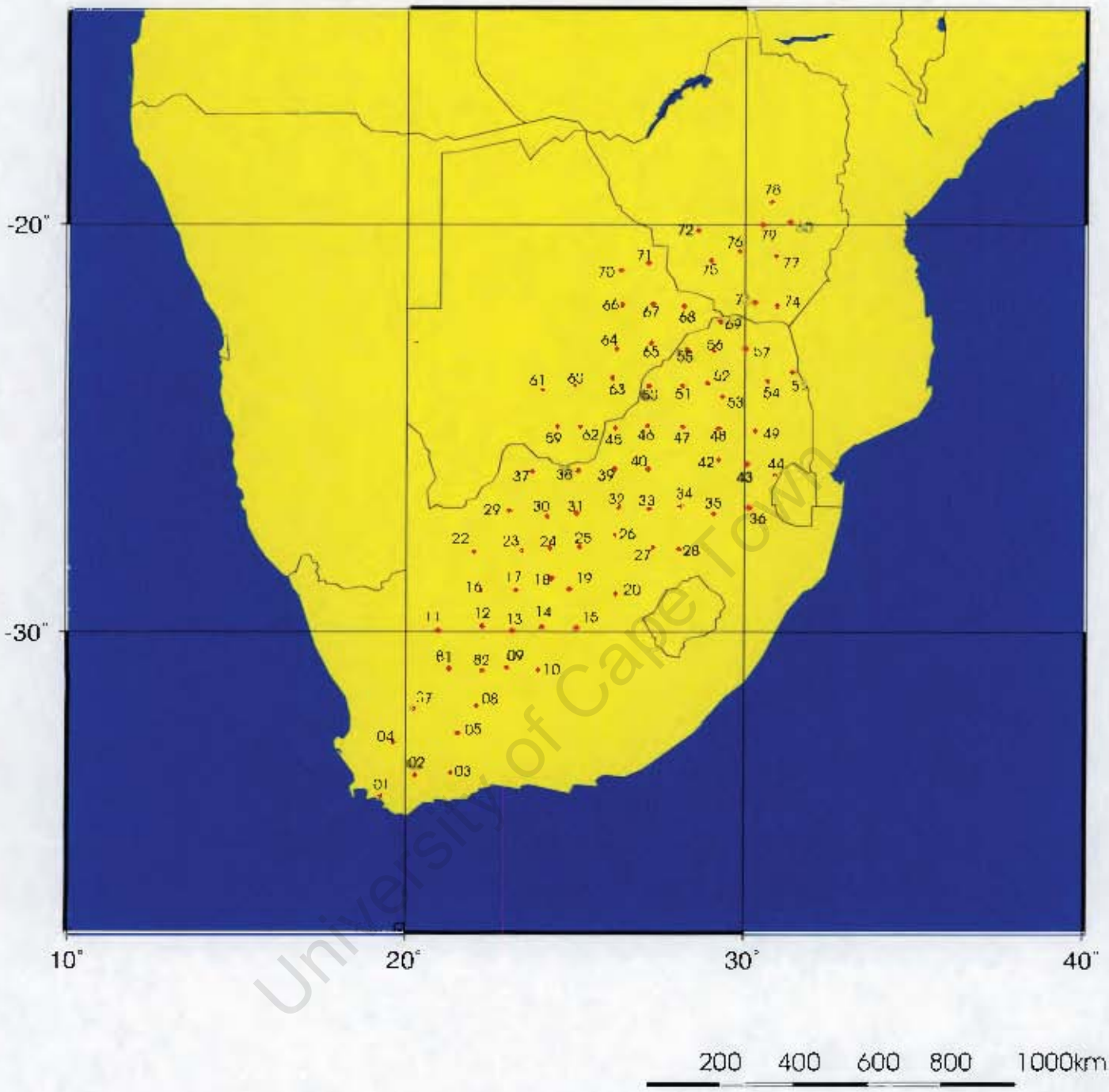

Fig 3.1

Positions of the 82 recording sites from the regional array across southern Africa

Table 3.2

Station coordinates of the Kimberley array

Station	Lat. S	Lon. E	Station	Lat. S	Lon. E	Station	Lat. S	Lon. E
BB01	28.307	24.754	BB12	28.528	24.711	BB23	28.645	24.823
BB02	28.382	24.591	BB13	28.539	24.735	BB24	28.625	24.671
BB03	28.407	24.625	BB14	28.540	24.677	BB25	28.671	24.883
BB04	28.404	24.589	BB15	28.600	24.897	BB26	28.672	24.968
BB05	28.440	24.580	BB16	28.579	24.538	BB27	28.676	24.521
BB06	28.451	24.623	BB17	28.559	24.707	BB28	28.690	24.568
BB07	28.416	24.691	BB18	28.669	24.936	BB29	28.705	24.843
BB08	28.428	24.628	BB19	28.602	24.833	BB30	28.795	24.865
BB09	28.449	24.638	BB20	28.632	24.684	BB31	28.793	24.925
BB10	28.449	24.754	BB21	28.642	24.633	BB32	28.815	24.977
BB11	28.466	24.547	BB22	28.629	24.787			

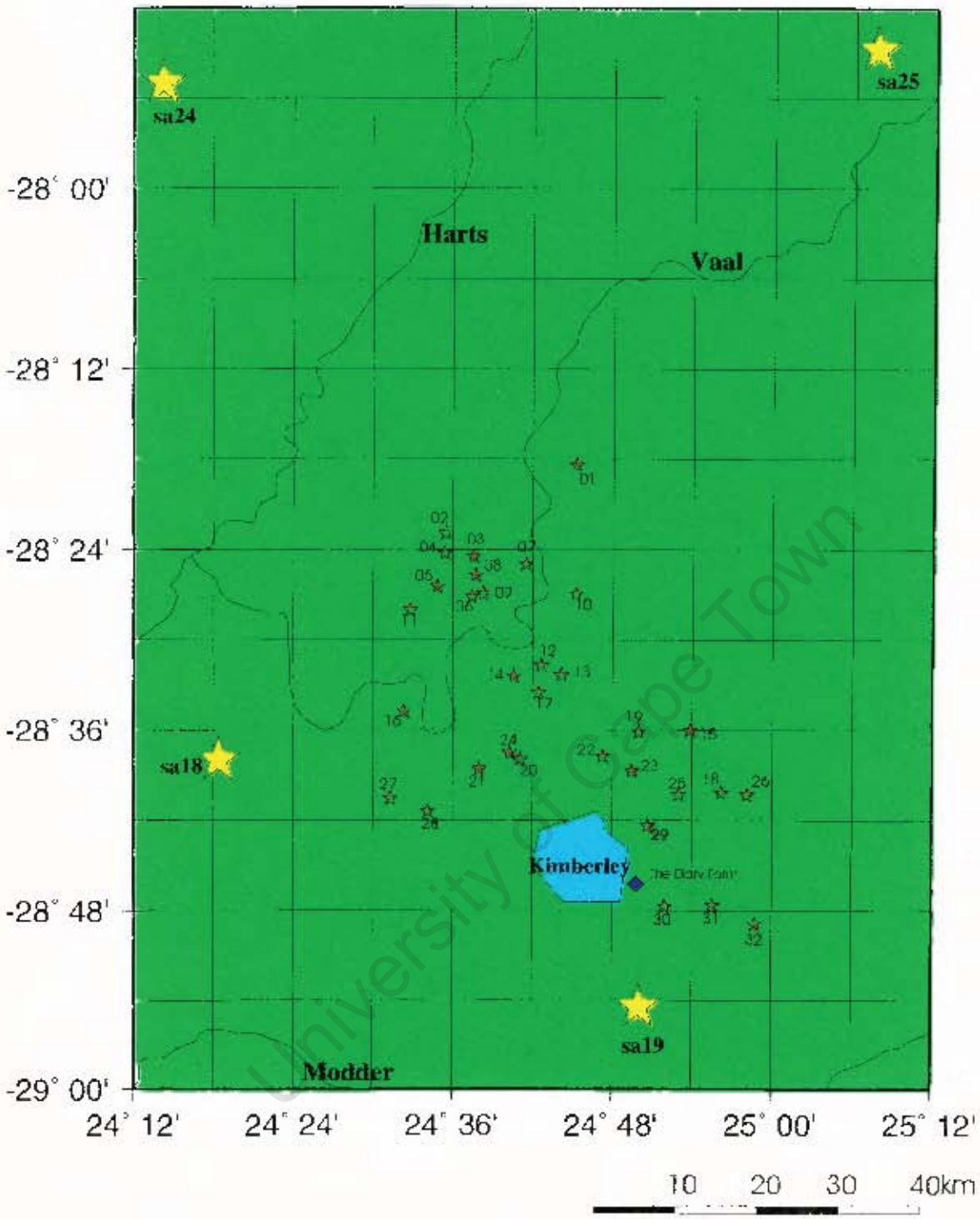

Fig 3.2

Positions of the 32 stations in the dense array and of the 4 stations from the regional array placed near Kimberley. The Diary Farm is the name of the De Beers' geological laboratory just outside the town.

Chapter 4

Receiver Functions as a Method of Studying Upper Mantle Discontinuities

4.1 Introduction

A commonly used technique to estimate the structure of the Earth's crust and upper mantle from a single three-component seismogram is to deconvolve these components to produce source equalised radial and transverse records (e.g. Langston 1977; Owens *et al.* 1987; Chevrot & Girardin 2000). These 'receiver functions' can be used to display the relative response of the Earth's structure near the receiver. The horizontal components are deconvolved by the vertical component to produce a trace dominated by Ps conversions and converted S-wave reverberations (Gurrola *et al.* 1994). Figure 4.1 shows raypaths of synthetic converted waves and the corresponding receiver function (taken from Ammon 1990). The amplitudes of the different phases in the receiver function are dependent on the angle of incidence of the impinging P-wave and the velocity contrast generating the Ps conversion (as well as the reflected multiples; see Figure 4.1). The arrival times of the converted phases (and the multiples) depend on the depth at which the conversion occurs due to the velocity contrast; the P- and S-wave velocities between the contrast and the surface; and the P-wave angle of incidence, known as the ray parameter, p. The amplitudes of the arriving phases depend on the nature of the velocity transition, i.e. on how sharp the velocity boundary is. The earthquake generating the waves needs to be sufficiently far from the recording station so that the waves arrive at a high angle to the surface.

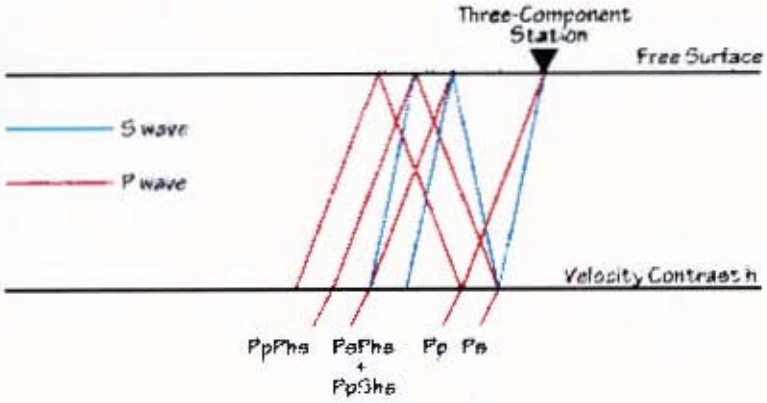

Fig 4.1a

Raypaths of synthetic direct and converted phases

Taken from Ammon (1990)

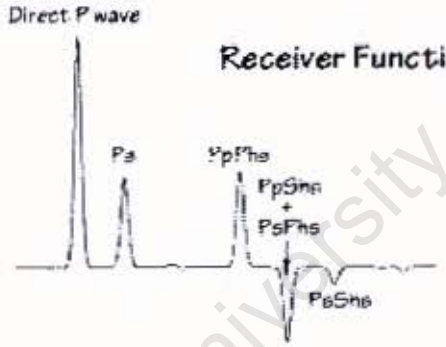

Fig 4.1b

Receiver function corresponding to a)

Taken from Amon (1990)

The earliest receiver function studies were computed by Phinney (1964) who used spectral rotation. The first true receiver functions were computed by Langston (e.g. 1977, 1979). Since then these functions have been used by many scientists to study the Earth's structure in different parts of the world (e.g. Owens *et al.* 1988; Given & Helmberger 1980; Ryabov 1989).

4.2 Theory

Langston (1979) developed the source equalization procedure to isolate the near-receiver structure, the receiver function, from the effects of near-source structure and the source functions.

The procedure assumes that three components of the response at a station due to a teleseismic P-wave, D(t), can be theoretically represented by:

$$D_v(t) = I(t)*S(t)*E_v(t)$$
$$D_r(t) = I(t)*S(t)*E_r(t)$$
$$D_t(t) = I(t)*S(t)*E_t(t) \qquad (4.1)$$

where v,r,t are respectively the vertical, radial and tangential components, I(t) is the impulse response of the recording instrument, S(t) the seismic source function, E(t) the impulse response of the earth's structure and * the convolution operator.

E(t) is of the form:

$$E(t) = \sum_{i=1,n} \{\alpha_i \delta(t-\tau_i) + \beta_i H[\delta(t-\tau_i)]\} \qquad (4.2)$$

where α_i and β_i are constants related to the product of reflection-transmission coefficients, $\delta(t)$ is the Dirac delta function, τ_i the travel time of the i^{th} of the n rays and H[] the Hilbert transform operator.

From observations of the vertical component of ground motion of deep teleseismic

earthquakes, it can be assumed that $E_v(t)$ behaves approximately like a Dirac delta function, hence

$$E_v(t) \approx \delta(t) \qquad (4.3)$$

This implies that

$$D_v(t) \approx I(t)*S(t) \qquad (4.4)$$

Therefore by deconvolving $D_v(t)$ from $D_r(t)$ and $D_t(t)$ respectively, and transforming into frequency domain, it is possible to isolate $E_r(t)$ and $E_t(t)$, with the following result:

$$E_r(\omega) = D_r(\omega)/[I(\omega)S(\omega)] = D_r(\omega)/D_v(\omega)$$
$$E_t(\omega) = D_t(\omega)/[I(\omega)S(\omega)] = D_t(\omega)/D_v(\omega) \qquad (4.5)$$

where ω is the frequency.

While we used the convolution operator in equation (4.1) here we have simple arithmetic division, as the convolution operator in the time domain corresponds to multiplication in the frequency domain.

This deconvolution can be performed by dividing the Fourier transform of the horizontal components by that of the vertical components after introducing a minimum allowable level for the amplitude spectrum of the vertical component.

The procedure in (4.5) (Langston, 1979) is numerically unstable, as the signals are band-limited and contain random noise, so the method of Helmberger and Wiggins (1971) is used to estimate the deconvolution. The result is smoothed out by a Gaussian function to exclude high-frequency noise, giving the following expression for the radial receiver function:

$$|E_r(\omega)|^2 = [\, D_r(\omega)D^+_r(\omega) / \varphi(\omega) \,]\, G(\omega) \qquad (4.6)$$

where

$$\varphi(\omega) = \max(D_v(\omega)D^+_v(\omega), c \max[D_v(\omega)D^+_v(\omega)]) \quad (4.7)$$

and

$$G(\omega) = e^{-(\omega/2\alpha)^2} \quad (4.8)$$

where c is the allowable spectral amplitude of the vertical component (known as the water level, which will be discussed in detail later), expressed as a fraction of the maximum amplitude; α controls the width of the Gaussian pulse and D^+_v represents the complex conjugate of D_v. Transformation back into equation (4.6) will produce an estimate of $E_r(t)$.

$G(\omega)$ is the low-pass Gaussian filter used to 'clean-up' high-frequency noise in the receiver function. The frequency content is controlled by the Gaussian filter-width parameter, α. The Fourier transform of a Gaussian is a Gaussian, so the filter is gentle. To quantify the filter by the frequency at which it has a value of 0.1, the following table can be constructed (Ammon, 1990):

Table 4.1

Dependence of frequency on the filter-width parameter

Value of 'α'	Frequency (Hz) for which G(f) = 0.1
10	4.8
5	2.4
2.5	1.2
1.25	0.6
0.625	0.3
0.5	0.24
0.4	0.2
0.2	0.1

4.3 Water-level deconvolution

In the spectra that we are dealing with, very small spectral amplitudes can be encountered. This may lead to singularities (as the denominator in equation (4.6) tends toward zero), possibly causing disturbance in the final result (Ammon 1990). In water-level deconvolution, division in the spectra by the small values discussed above during the computation of receiver functions can be avoided by introducing the trough filler, c, which was mentioned above. It is a fraction of the maximum value of the denominator. All small numbers of amplitude are then replaced with that fraction. Figure 4.2 illustrates the water-level deconvolution in graphic terms. The value of c, which can act as a high-pass, low-pass or a notch filter, is chosen by trial and error. This value should be as small as possible. Ideally it should be equal to zero for theoretically purest results, but then we will encounter the same problems we would have had without using the trough filler at all. However, if the chosen value is too high, the water level can cover up significant features of the spectrum, causing distortions in the receiver function.

4.4 The averaging function

The averaging function is computed by deconvolving the vertical component from itself using a chosen water-level filler, c. If c is zero, the averaging function is a perfect Gaussian. As c increases, the averaging function broadens, and often distorts for the large values. This assumption of the averaging function is valid if the data are not noisy and all the underlying assumptions in the deconvolution procedure hold.

4.5 Values of α and c for computing the receiver functions

The values of α, (the Gaussian width), and c, (the trough filler), used to create individual receiver functions were chosen by trial and error – receiver functions

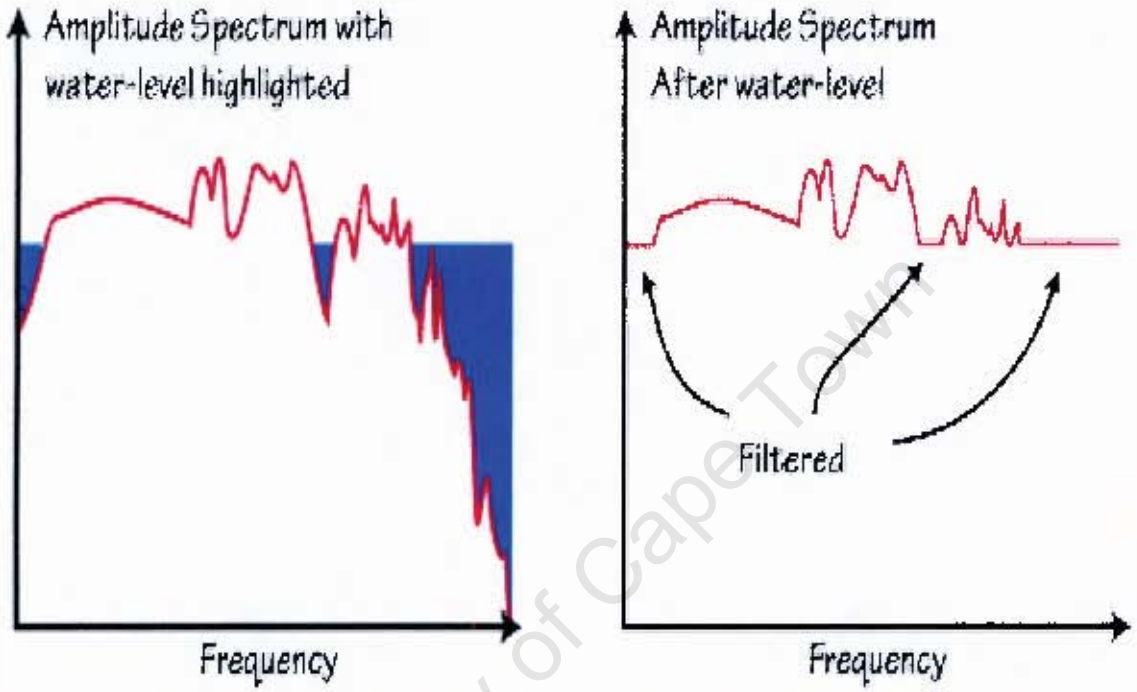

Fig 4.2

Graphic representation of water level deconvolution.
Taken from Ammon (1990)

were computed using different sets of parameters, and then the best resulting function was chosen.

Figure 4.3 shows different receiver functions computed (radial components only) using different values for α and c from a single event (Iran earthquake from the 10th of May 1997) recorded by a particular station (sa32). Figure 4.3(a) shows receiver functions that were obtained using the Gaussian width of 1, while the trough filler was varied: .0003 for the top function, and increasing to .003, .03 and .3 for the other three. For figure 4.3(b) and (c) Gaussian widths of 3 and 5 respectively were used, while the value of c was varied in the same way as for figure 4.3(a).

It can be observed from figure 4.3 that using a Gaussian width of 1 produces receiver functions of quite low frequency – they are very smooth and possibly smooth out important features of the function. Larger Gaussian width values will create higher frequency receiver functions. An optimum choice for this parameter is $\alpha = 3$, where important features are clearly visible. Unless otherwise stated, the value of $\alpha = 3$ is used for the computation of the receiver functions in the next sections.

The other parameter we need to choose is the trough filler, c. Looking at figure 4.3(b) we can see that that the two bottom receiver functions (with $c = 0.03$ and 0.3 respectively) are very broad, and lose potentially important features. The top function, with $c = 0.0003$, has, on the other hand, too many sharp features that would make interpretation difficult. The value of $c = 0.003$ produces a good balance, so this will be the value used to make receiver functions in the later chapters.

Figure 4.4 shows all 3 components of the receiver function calculated using a Gaussian width of 3 and a trough filler of 0.003.

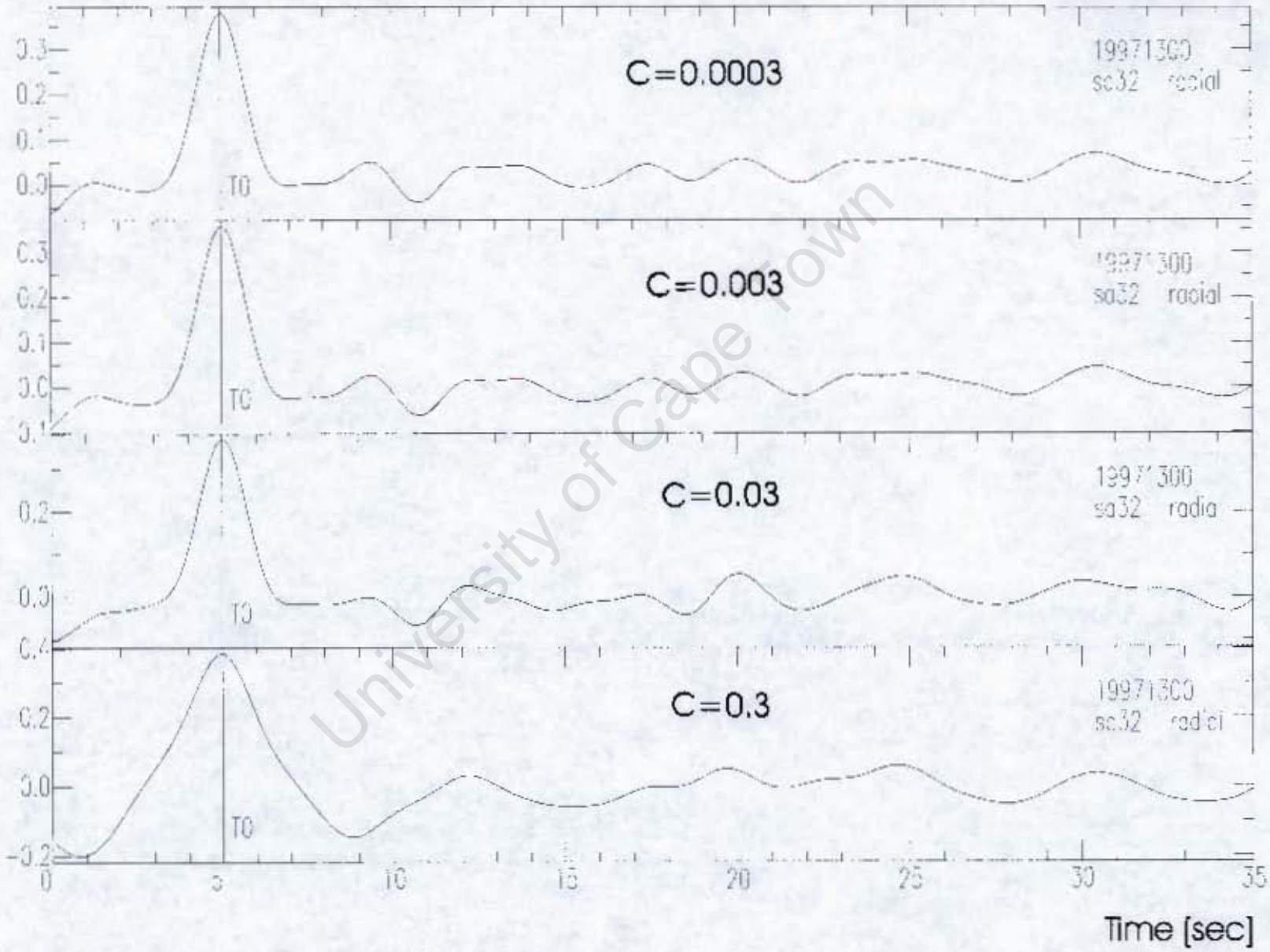

Fig 4.3a

Radial components of receiver functions computed for different values for the trough filler c using a Gaussian width of 1

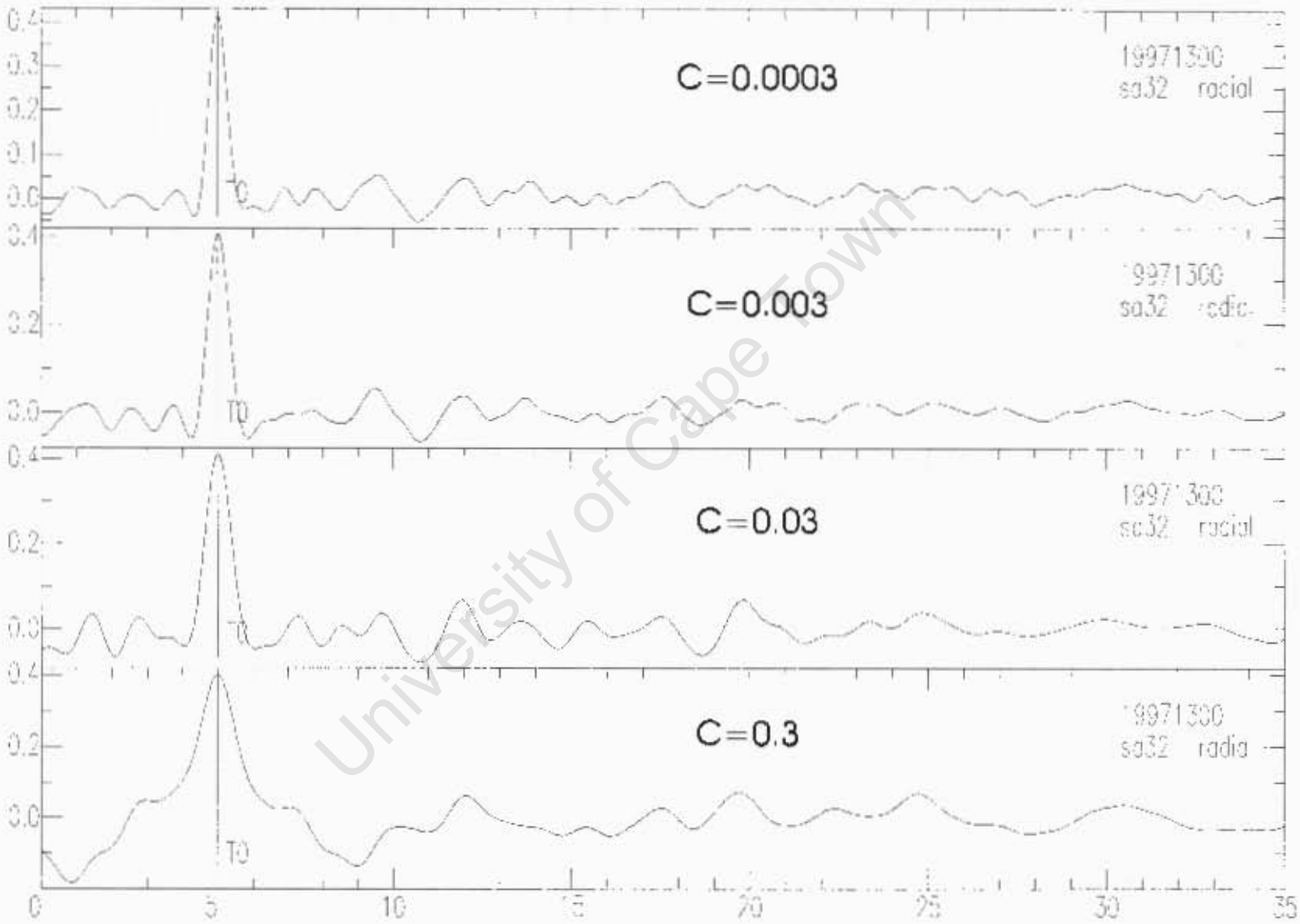

Fig 4.3b

Radial components of receiver functions computed for different values for the trough filler c using a Gausslan width of 3

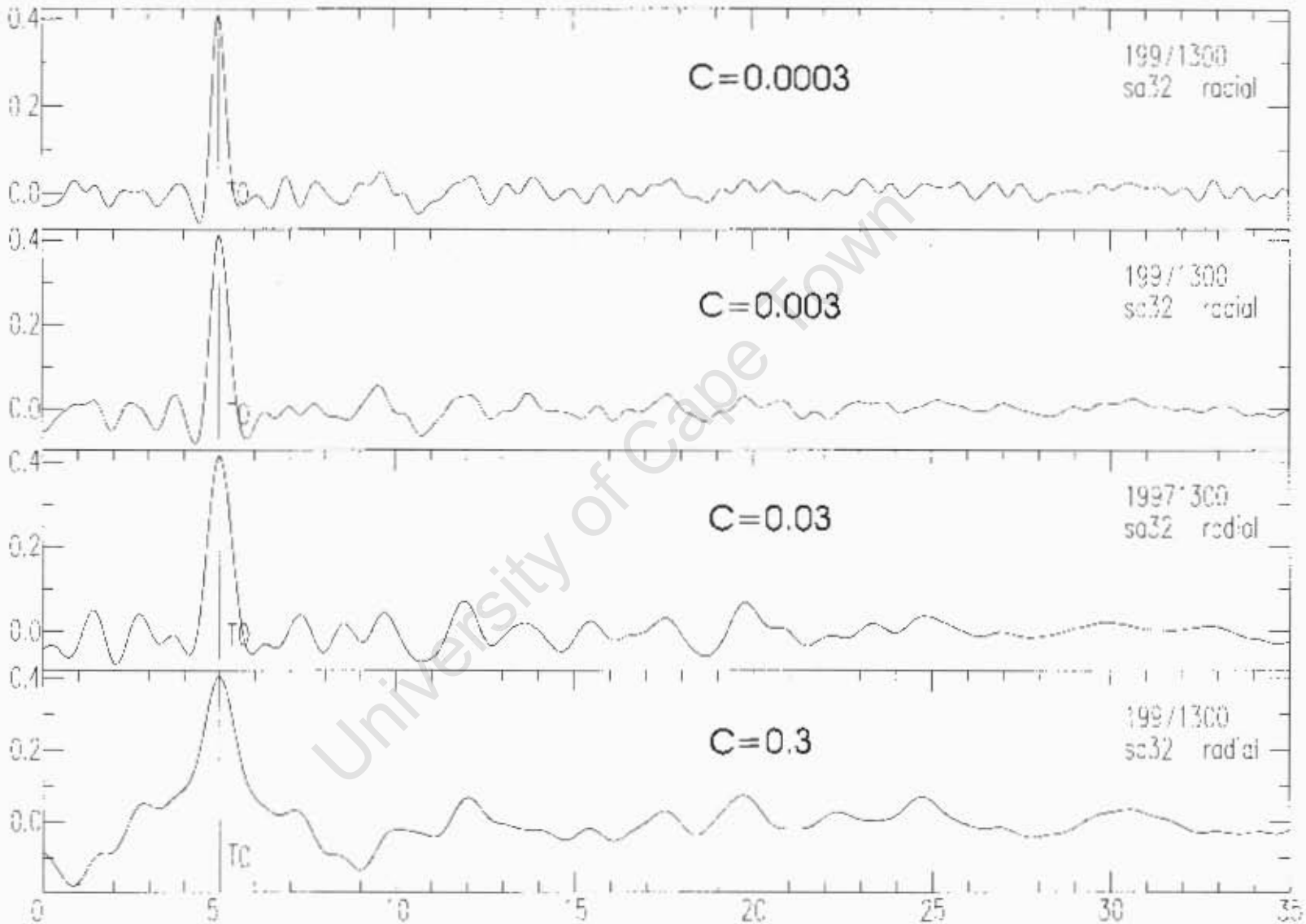

Fig 4.3c

Radial components of receiver functions computed for different values for the trough filler c using a Gaussian width of 5

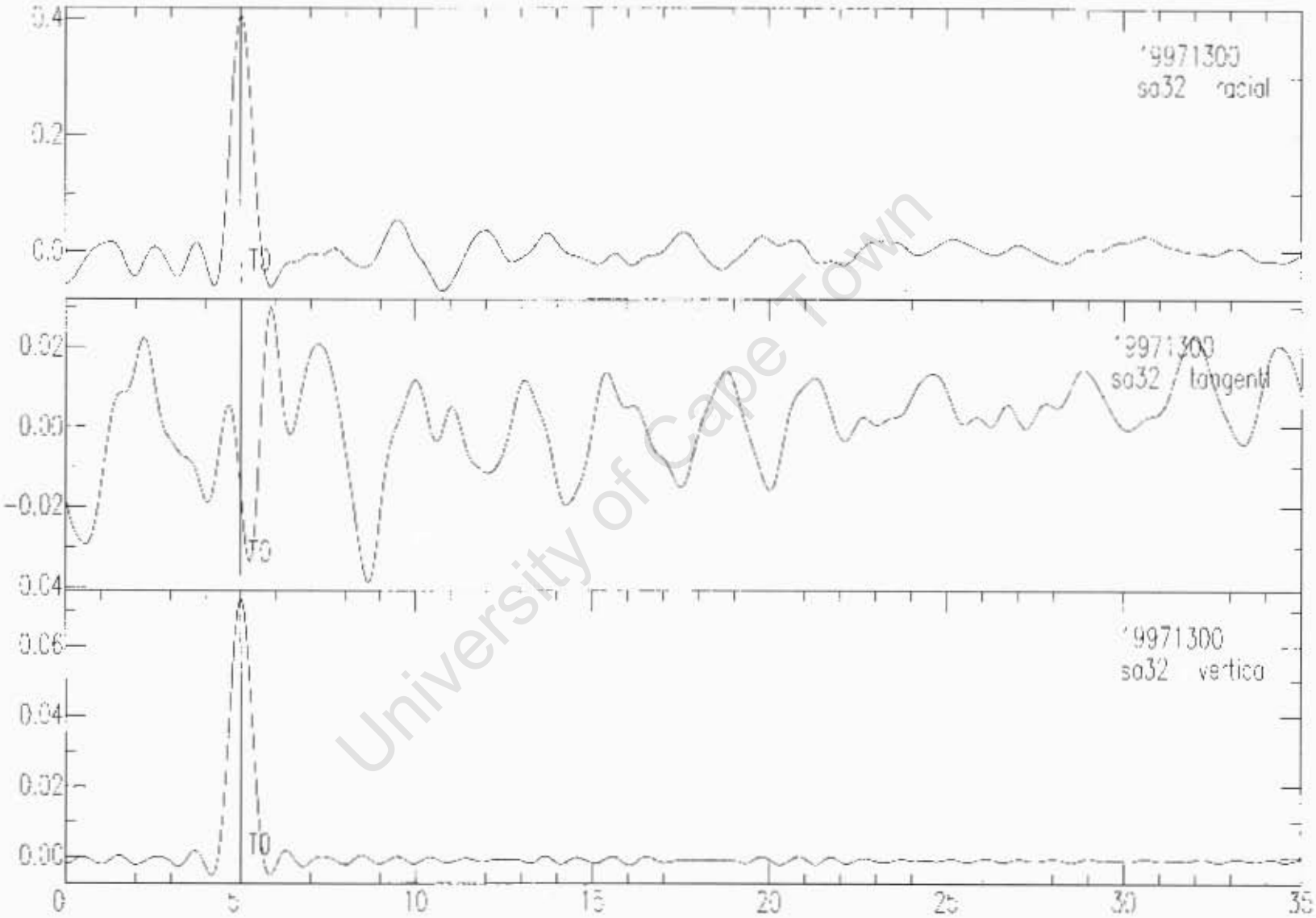

Fig 4.4

Radial, tangential and vertical components of the best receiver function.
Obtained using a trough filler of 0.003 and a Gaussian width of 3.

4.6 Data preparation and processing

The data were manipulated using the Seismic Analysis Code (SAC), developed at Lawrence Livermore National Laboratory (Tapley & Tull, 1992).

The raw data were read in as single events using SAC. Noisy events (i.e the ones where seismic noise overrode the signal of the actual event) were discarded. From the remaining events the offset (mean noise level) and trend were removed, using the RTR procedure in SAC. This procedure is based on a least squares curve fit to the data. The seismograms were then filtered if necessary (this is described in detail in section 4.6.1).

After picking the P-wave arrival time and setting the time window to a required length, receiver functions were computed from the data using the program PWAVEQN (Ammon, 1990), which performs the source equalization (Langston, 1979). The standard time window length to identify crustal structure is 35 seconds – 5 seconds before and 30 seconds after the P-wave arrival. For the analysis of upper mantle discontinuities, windows of length up to 2 minutes were used.

Program PWAVEQN rotates the components to their theoretical radial and tangential components, deconvolves the vertical component from the horizontal, and the averaging function is normalized to unity amplitude. The output of PWAVEQN is 3 files (in SAC format), i.e. the radial and tangential components of the receiver function and the averaging function.

4.6.1 Filtering data

Different events require different filters. Some can produce good results without using filters. Most events, however, need to have noise filtered out of them before they can be processed.

When a noisy event is read in, the filter to be used is normally chosen by trial and error - trying different ones until a clear seismogram is obtained. When the noise is

in the low frequencies, a high-pass Butterworth filter is used to reject frequencies below the given limit. This limit should be as low as possible, as while all noise should be eliminated, the actual signal will be affected by the filter as well, and this will in turn affect the analysis. Usually the limit used is 0.2 or 0.3 Hz, but in some cases values as high as 0.6 Hz must be used. The most gentle (2 pole) filters will be used here.

On the other hand when the frequency of the seismic noise is higher than that of the actual event signal, a Butterworth low-pass filter can be used. In this case the cut-off limit is usually under 0.1 Hz.

It is also possible to use band-pass filters that eliminate all signals except the ones between two specified frequencies. This is normally used for very noisy data, in attempt to isolate the frequency of the event signal from the noise. Band rejections can also be done – here all signal with the frequency between the two specified limits is eliminated from the record. This is used when the frequency of the noise can be identified precisely, which is very rarely the case.

4.6.2 Stacking

Stacking is a specific property of receiver functions, as all the signal, no matter how complicated, is compressed to a spike series. Stacking is a very powerful tool for improving the signal-to-noise ratio. For a given station one can stack together receiver functions from similar distances. If the distances of the incoming events are significantly different, one has to take this into account, and the stacking procedure becomes more difficult, and special computer programs need to be used.

Stacking is always used instead of all single seismograms seperately because of the ever-present noise. As the noise is fairly random and incoherent, for a sufficiently large set of signals it will largely average out towards a predicted signal. The real features, on the other hand, that appear consistantly in the same place on all the

seismograms, will all be clearly seen after averaging the signals. Thus after completing a stack, the features should be more prominent, as they will no longer be obscured by noise. Also after cleaning out the noise from the waveforms, weak but coherent signals will become visible (Schimmel and Paulssen, 1997).

SAC is equipped with a stacking programme called ROSTACK. Unless otherwise stated, this programme will be used to stack waveforms in this thesis.

4.7 Basic features of receiver functions

Observations of the radial components of receiver functions reveal several significant features. The function is dominated by the direct P-wave arrival, by far the most prominent peak. A few seconds after this peak is a much smaller, but still clearly visible (in most cases) peak that corresponds to the arrival of the P-wave that has been converted to an S-wave at the Mohorovicic boundary (the Moho), the first significant discontinuity, which seperates the Earth's crust from the mantle. This wave is referred to as the Ps wave.

The next visible phase of the receiver function is the arrivals of waves reflected once off the Earth's surface and once off the Moho, and being converted from P-wave to S-wave at either the Moho or the surface (see figure 4.1b). The near vertical reverberations ending as an S-wave (e.g. Ppps) contribute much more energy to the horizontal components than those arriving as a P-wave, like Pspp (Gurrola *et al.* 1994). For this reason the Pppp wave is not visible, and the first clear multiple arrival is the sum of all reverberations with 2 P-wave legs and an S-wave leg, for convenience collectively labelled P2p1s or Ppps.

The next arrival, shortly after the P2p1s is the P1p2s (also refered to as Ppss), i.e. sum of the reverberations with 2 S-wave legs and a P-wave leg. This has reversed polarity, and therefore appears in the receiver function as a trough instead of a peak – this property makes the P1p2s easily distinguishable. Unfortunately the multiples

require ideal conditions to be detected, and are not always visible, even though the Moho converted phase may be clear.

Looking further down in the time window are the converted Ps signals from deeper discontinuities. For those, only the direct Ps is studied, as the multiples would be too far away in the time window.

4.8 Estimating the depth of the discontinuity

By measuring the difference between the arrival times of the direct P-wave and the converted Ps reverberation we are able to estimate the depth of the discontinuity at which the conversion took place.

Figure 4.5 shows the geometry of the conversion. Part of the incoming wave refracts at the boundary, but remains a P-wave – this arrives at the seismic station as the direct P-signal after time t_p from the point of refraction. The part of the wave front that converts into an S-wave reaches the station after time t_s from the discontinuity.

If the planar wave front is parallel to the surface, then the distance traveled by the P- and S-waves between the discontinuity and the surface is the same, and is equal to the depth, h, at which the conversion took place. Then

$$t_p = h / v_p$$
$$t_s = h / v_s \qquad (4.9)$$

where v_p and v_s are the velocities of P- and S-wave above the discontinuity. The time difference between the arrivals is then

$$\Delta t = t_s - t_p = h \cdot (v_p - v_s) / (v_p \cdot v_s) \qquad (4.10)$$

and solving for h gives

$$h = \Delta t \cdot (v_p \cdot v_s) / (v_p - v_s) \qquad (4.11)$$

It can be seen that h is directly proportional to Δt. The constant of proportionality

can be determined if the velocities of the waves are known. Taking $v_p = 6.0$ km/s and $v_s = 3.5$ km/s (typical values for crustal velocities used to determine the crustal thickness, i.e. with the Moho as the discontinuity) makes the equation read

$$h = 8.4 \cdot \Delta t \qquad \textbf{(4.11a)}$$

if Δt is in seconds and h in km.

However, the planar wave front cannot be assumed to be parallel to the surface. From figure 4.5 it can be seen that in reality the angle of incidence of the incoming P-wave, or the corresponding ray parameter, is a significant factor. Also the refracted P-wave and the converted S-wave travel different distances, and the short traveltime labelled t_h is present.

Considering all the above mentioned factors, the time delay of the Ps reverberation is going to be

$$\Delta t\,(p, h, v_p, v_s) = t_s + t_h - t_p \qquad \textbf{(4.12)}$$

The dependence on the 4 parameters can be made explicit through manipulation of equation (4.12), similar to the development of the reflection moveout (Sheriff & Geldart 1982; Yilmaz 1987):

$$\Delta t\,(p, h, v_p, v_s) = h \cdot [\,(v_s^{-2} - p^2)^{1/2} - (v_p^{-2} - p^2)^{1/2}\,] \qquad \textbf{(4.13)}$$

where p is the ray parameter.

Solving for h gives

$$h = \Delta t \,/\, [\,(v_s^{-2} - p^2)^{1/2} - (v_p^{-2} - p^2)^{1/2}\,] \qquad \textbf{(4.14)}$$

It is clear that h is still directly proportional to Δt, (i.e. $h = a \cdot \Delta t$) and for $p = 0$ eqation (4.14) simpifies to equation (4.11). Table 4.2 below shows how the constant of proportionality, a, behaves as the ray parameter changes for $v_p = 6.0$ and $v_s = 3.5$ km/s.

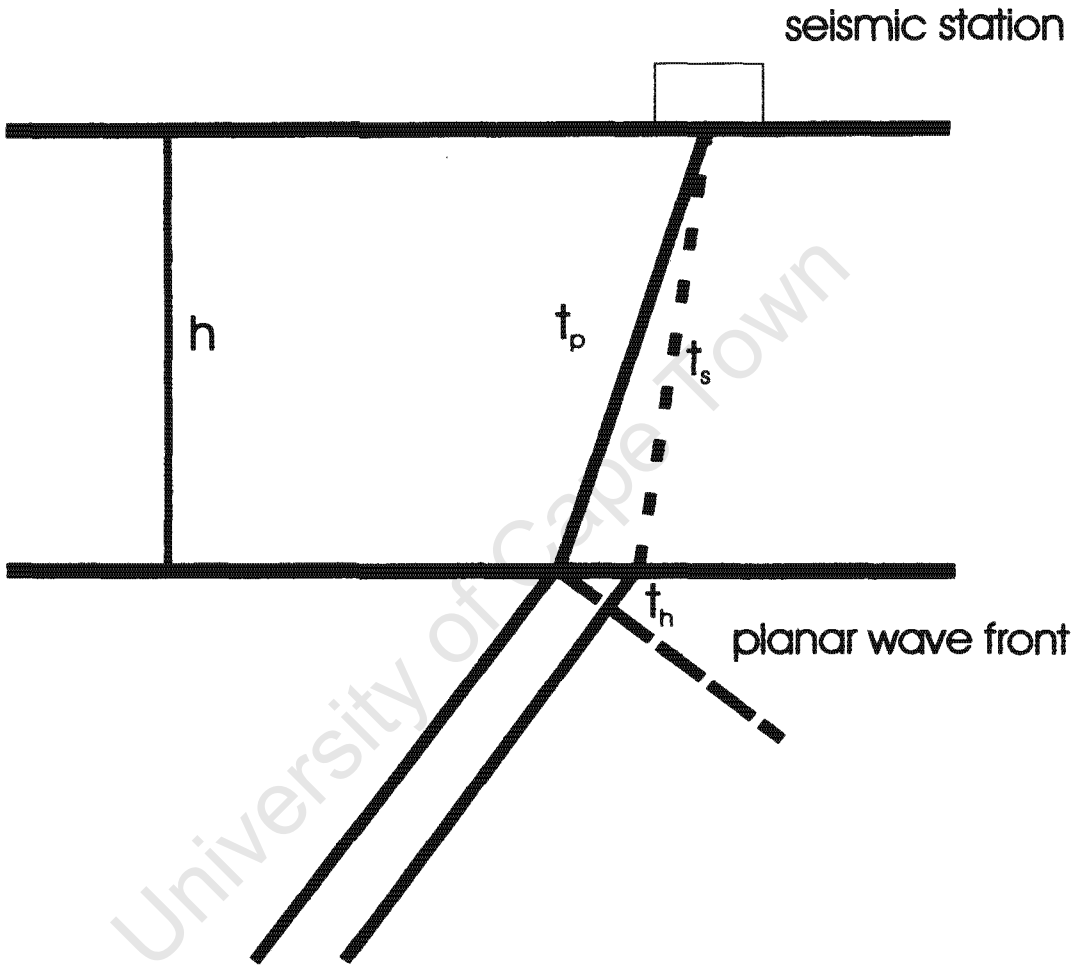

Fig 4.5

Raypaths for the Ps relative to the direct P
with a non-zero ray parameter

Table 4.2

Effect of the ray parameter on the arrival time of converted phases

p(s/km)	a	p(s/km)	a	p(s/km)	a
0.000	8.400	0.030	8.320	0.060	8.074
0.005	8.398	0.035	8.291	0.065	8.016
0.010	8.391	0.040	8.257	0.070	7.952
0.015	8.380	0.045	8.219	0.075	7.883
0.020	8.365	0.050	8.176	0.080	7.808
0.025	8.345	0.055	8.127	0.085	7.727

We see that the constant of proportionality decreases as the ray parameter increases, so assuming h is constant the time delay is going to increase with p. In terms of the delay of Ps relative to the direct P-wave arrival at vertical incidence, and using the velocity ratio $r = v_p/v_s$ (usually assumed to be $\sqrt{3}$ – see section 7.3.5) we have (Gurrola *et al.* 1994), in terms of slightly new parametres,

$$\Delta t\,(\Delta t_0, p, v_s, r) = [(1 - p^2 v_s^2)^{0.5} - (r^{-2} - p^2 v_s^2)^{0.5}] \cdot (r \cdot \Delta t_0) / (r - 1) \qquad \textbf{(4.15)}$$

where Δt_0 is the time delay of the Ps reverberation for the case of a vertical incidence ($p = 0$), i.e. again in terms of p, h, v_p and v_s

$$\Delta t_0 = \Delta t\,(0, h, v_s, v_p) \qquad \textbf{(4.13a)}$$

4.9 Receiver functions in this study

As mentioned before, the aim of this paper is to investigate discontinuities in the crust and the upper mantle under Southern Africa. Receiver functions will be used to identify the discontinuities.

Records of seismic events will be converted to SAC format, and afterwards receiver functions will be computed from them.

For the regional array of stations these functions from different events will be stacked for each station. From the stacks produced it will be possible to identify the existence and depth of any discontinuities under a particular station. These results will then be mapped to show how the crustal and upper mantle structure varies over the whole area.

For the dense array in the Kimberley area a similar procedure will be used. However, since the stations are very close to each other it will be feasible to stack receiver functions obtained at different stations. This would present a problem if the structure under the stations was significantly different, which is very unlikely as they are closely packed – usually only a few kilometers apart. We will be able to check that by examining records for individual stations, or groups of few stations. If all the receiver functions are stacked together, the noise to signal ratio will be substantially reduced, and features of the receiver function more clearly visible.

After obtaining the depths of discontinuities we will then be able to use them to create a seismic wave velocity model as a function of depth. The procedure for this will be discussed later.

Chapter 5

Crustal Thickness Beneath Southern Africa

5.1 Introduction

The thickness and structure of the crust of Southern Africa has been the subject of a number of studies in the recent past (Harvey 1999; Nguuri, 2000). In this thesis measuring crustal thickness is used as an example to illustrate how receiver functions can be used to study discontinuities deep underneath the Earth's surface.

The crustal thickness is determined by finding the depth of the Moho, which is the most shallow world-wide discontinuity of the solid Earth, separating the Earth's crust from the mantle.

5.2 Seismic events used

Data from 10 seismic events from different parts of Asia have been used in this study. The details of these events are given in the table below, and the locations of their epicentres are illustrated in Figure 5.1.

These events have ray parameters varying from 0.015 to 0.050, so stacking them was far from ideal, but with data availability being a major problem there was no real alternative. The events with the lowest ray parameters (97168, 98123 and 98245) possibly contained core phases, which are rarely used for receiver functions due to a complicated signal in a narrow window. They were, however, used anyway with no other data available.

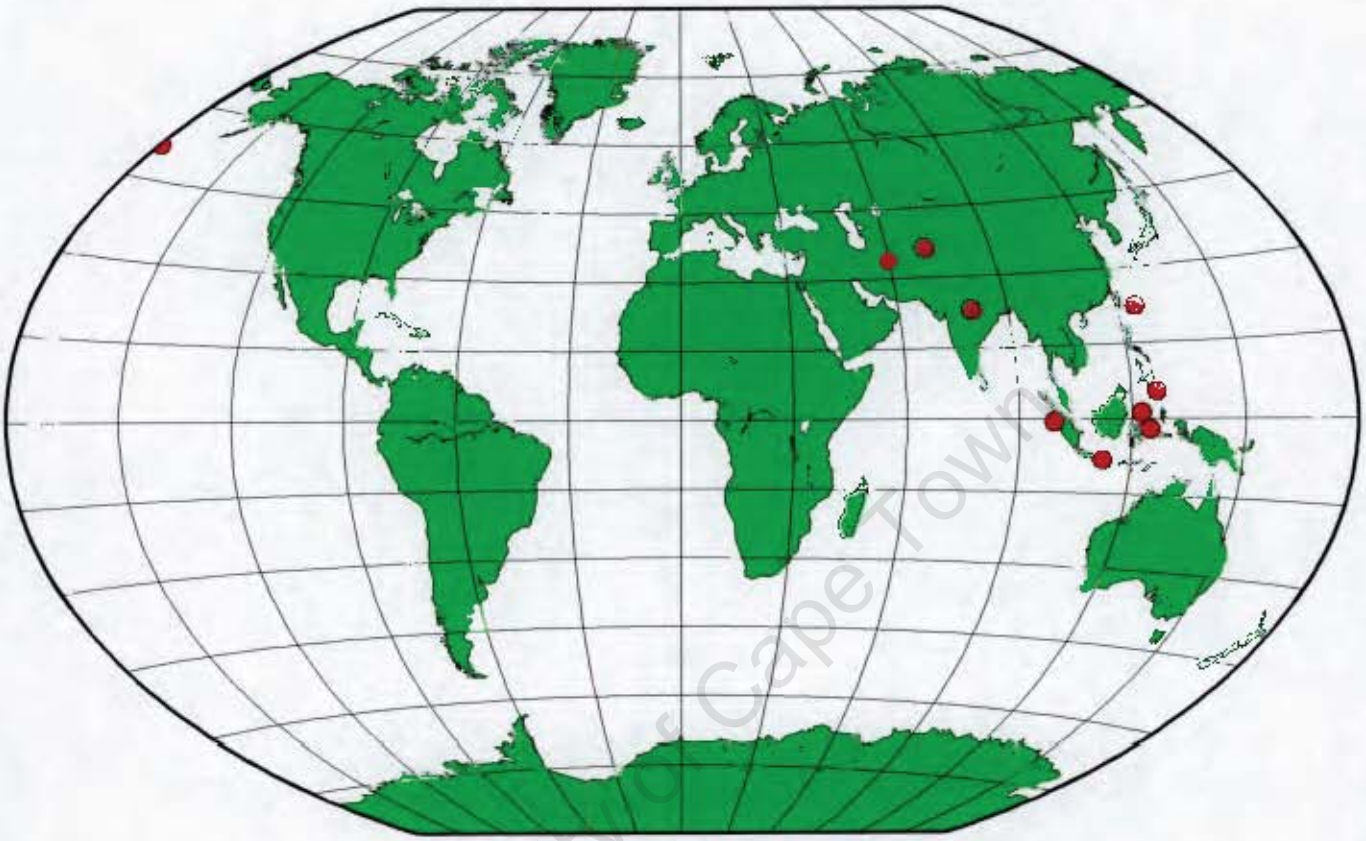

Fig 5.1

Locations of the 10 earthquakes used in this study

Table 5.1

Time and locations of the seismic events used in this study

Date	Latitude	Longitude	Location	Magnitude
97130	33.825N	59.809E	Iran	6.4
97133	36.411N	70.945E	Afghanistan	6.1
97141	23.083N	80.041E	India	6.0
97168	51.347N	179.332W	North Pacific	6.4
97329	1.241N	122.536E	Indonesia	6.1
98091	0.544S	99.261E	Indonesia	6.2
98123	22.306N	125.308E	Chinese Sea	6.4
98245	5.410N	126.764E	Philippines	6.6
98271	8.194S	112.413E	Indonesia	6.4
98333	2.071S	124.891E	Indonesia	6.5

The dates used are in numerical format, i.e. 97130 refers to the 130th day of 1997, or the 10th of May 1997. The date in that format will be used as the index for referring to individual events.

5.3 Data processing

The seismograms from the above events were recorded by 42 of the stations in the regional array described in section 3.2. Receiver functions were then computed using the procedures discussed in chapter 4. The functions from different events were stacked for each of the individual stations, and the arrivals of the Ps waves produced at the Moho discontinuity were picked on these 42 individual stacks.

Using seismic velocities of v_p = 6.5 km/s and v_s = 3.8 km/s, appropriate for an Archean craton (e.g. Drummond & Collins 1986), and an average parameter of 0.030 s/km, equation (4.14) becomes:

$$h = 9.0 * \Delta t \qquad (5.1)$$

5.4 Results

The stacks produced for the 42 stations are included in Appendix A. In each case the P-wave coherence peak can be seen clearly as the most prominent peak. The time windows were set to have this peak 5 seconds from the start. For stations SA27, SA36, SA56, SA60, SA66 and SA81 this value is not exactly 5 seconds, and this was taken into account for all calculation.

The arrivals of the Ps-wave produced at the Moho were also marked on each of the stacks, and the difference between the two arrivals was calculated for each station.

In most cases picking the Ps arrival was straight forward, but for some of the stations it was not obvious. For SA24, for example, there were 2 peaks of equal height next to each other, the earlier of the two being at the same time as the clear Ps arrival for SA25, and just before the one for SA23 – both of these stations are next to SA24. For all 3 of the above mentioned stations the P2p1s (which was discussed in detail in chapter 4) arrival can be seen at times between 20 and 21 seconds – the position of these peaks confirms that the earlier of the two possible Ps arrivals is the real one. Similar checks have been made for SA38 and SA66.

For some stations, prominent peaks were ignored as they were far too early to be candidates for the Moho discontinuity Ps arrivals. These included SA45 with a peak less than 3 seconds after the P arrival, SA48 with just over 3 seconds, and SA51 with about 3.5 seconds. These arrivals are most probably caused by phase conversions from inside the crust, as these time shifts correspond to a depth of just under 30 km. A possible place where this conversion could have taken place was the boundary between the lower mafic crust and the upper felsic, which is slower than the mafic and a conversion there would results in a positive peak in the radial component of

the receiver function. Results for station SA51 will discussed in more detail later in this chapter.

The time differences between the two arrivals at each station are shown below in table 5.2. The table also includes the crustal thickness beneath the station, calculated using equation (5.1). The calculated depths are shown in Figure 5.2.

5.5 Discussion

It can be seen from Figure 5.2 that in the south-western section of the craton the Moho depth is between 37 and 40.0km, except for station SA23, which recorded a depth of 43km. The 3 stations placed off the craton boundaries in that region (SA11, SA12 and SA81) gave depths of 40, 43 and 45km.

Further north along the western block of the craton the crustal thickness decreases (to as low as 36km for SA37), but increases significantly (up to 44km) in southern Botswana. The crust is also thicker near Vredefort and Johannesburg, with results from 40 up to 46.0km. The single reading from the Ancient Gneiss Terrain (SA36) gave a depth of 38km, while the result for the Barberton Region (SA44) was 43km.

In the northern section of the craton the crust becomes much thicker. The lowest reading from that area is 41km recorded by SA57, while most of the other results are over 45km, some of them even over 50km. SA47 recorded a depth of 52km.

Over the northern boundary of the Kaapvaal craton (in southern Zimbabwe) the crustal thickness decreases rapidly. Just over the boundary with the Zimbabwe craton it drops to 38-40km, while the northern-most station there (SA78) gave a reading as shallow as 36km.

Table 5.2

Crustal thickness (h) computed for different stations in this study and compared to results of Nguuri (2000)

Station	Δt (sec)	h (this study)	h (Nguuri)	Station	Δt (sec)	h (this study)	h (Nguuri)
SA11	4.5	40	42	SA47	5.8	52	50
SA12	4.8	43	45	SA48	5.3	48	45
SA17	4.1	37	36	SA50	5.0	45	43
SA18	4.1	37	36	SA51	5.0	45	50
SA19	4.1	37	36	SA52	4.6	41	42
SA22	4.3	39	35	SA55	4.8	43	45
SA23	4.8	43	44	SA56	4.7	42	45
SA24	4.4	40	38	SA57	4.6	41	43
SA25	4.4	40	38	SA59	4.9	44	45
SA27	5.1	46	40	SA60	4.8	43	45
SA30	4.1	37	35	SA62	4.9	44	45
SA31	4.3	39	38	SA65	5.0	45	45
SA32	4.5	40	40	SA66	5.5	49	50
SA36	4.2	38	37	SA67	5.1	46	46
SA37	4.0	36	34	SA68	5.7	51	48
SA38	4.1	37	38	SA74	4.8	43	44
SA39	4.7	42	42	SA76	4.2	38	35
SA40	4.8	43	45	SA78	4.0	36	35
SA44	4.8	43	40	SA79	4.4	40	35
SA45	5.7	51	44	SA80	4.2	38	36
SA46	5.2	47	44	SA81	5.0	45	47

The results calculated here can be compared to those obtained by Nguuri (2000). These are illustrated in Figure 5.3, and are also presented in Table 5.2. Mostly the results are similar, but there are some significant differences.

In Nguuri's results the crustal thickness in the southern region of the craton varies between 35 and 38km, with the exception of SA23, which recorded a depth of 44km. These results, based on significantly more data, are very close to the results in this study.

In the central section of the craton the results of both studies are very similar, results presented here being slightly higher; this is also the case for the Ancient Gneiss and Barberton regions in the eastern section of the craton.

There are some discrepancies in the northern section. I calculate the crust to be much thicker in that area, as does Nguuri. Results from individual stations, however, sometimes differ by up to 5km. The biggest difference in the studies are the results for station SA45. I calculate this to be 51km, 7km more than the 44km obtained by Nguuri. Another significant discrepancy is SA51, where Nguuri's 50km is 5km more than 45km computed here.

Looking at the stack of receiver functions for SA51 it can be seen that while there is a possible Ps arrival peak 1.5 seconds before the arrival of the S-wave produced at the Moho, there are no prominent peaks after the one that was chosen. This means there is no evidence in this study to suggest the crust is thicker than the 45km calculated. Similar checks can be made for other stations in the area.

As the stations move off the Kaapvaal craton, the results begin to agree again, with both models suggesting a rapid decrease in the crustal thickness of the Zimbabwe craton.

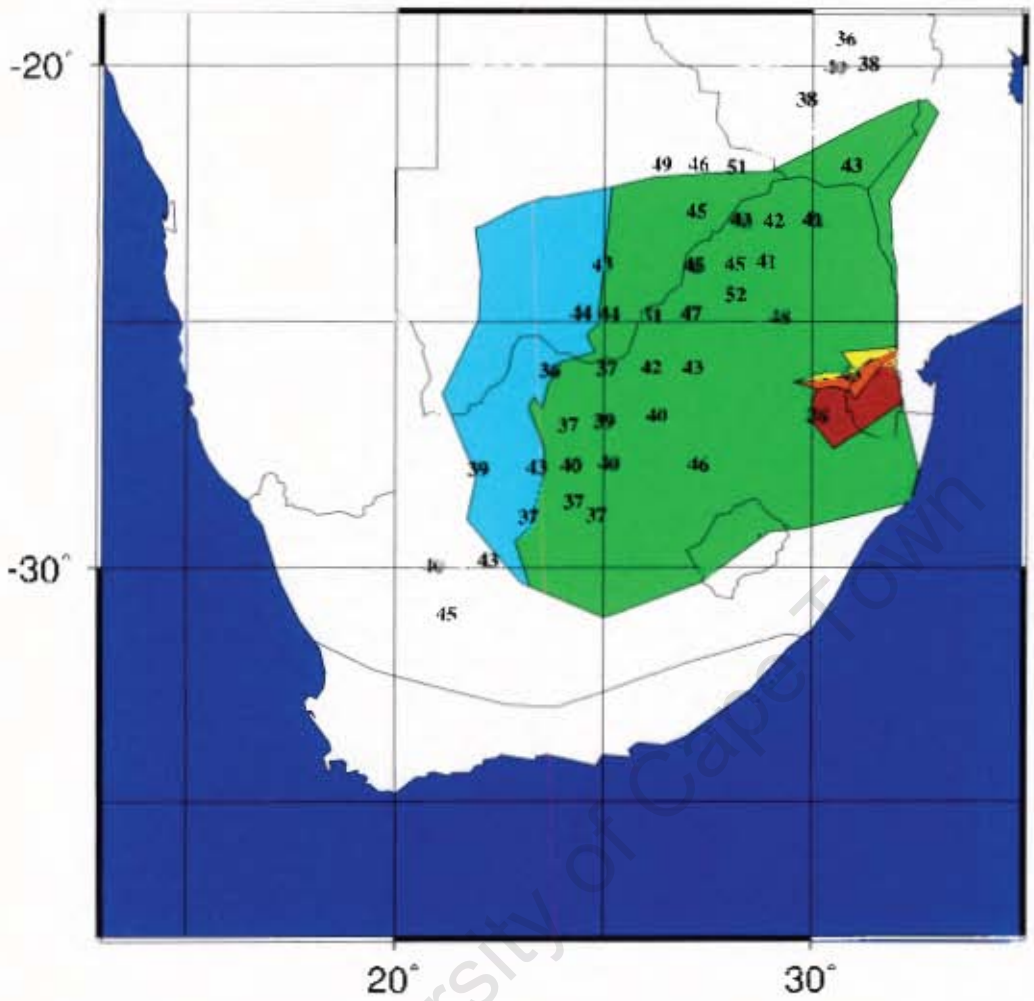

Fig 5.2

Crustal thickness (in km) for the 42 recording sites obtained in this study

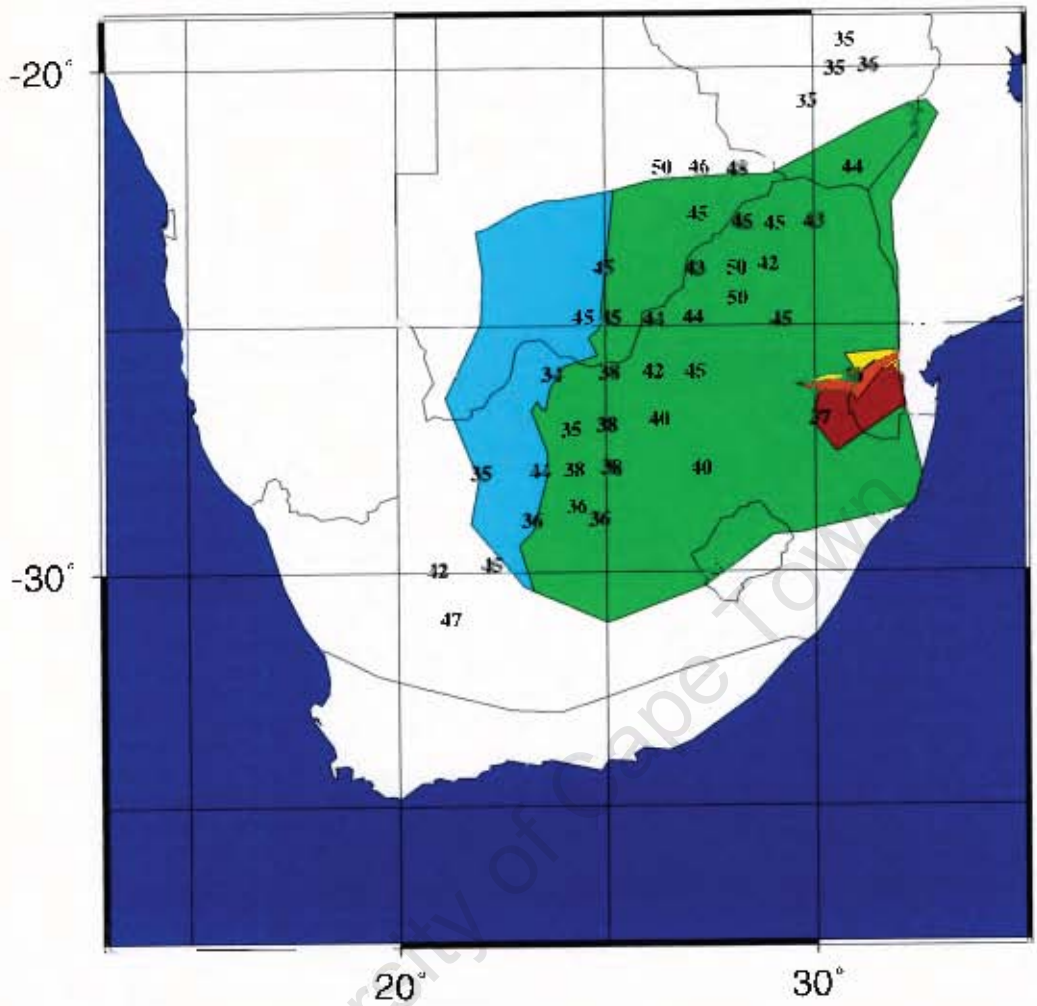

Fig 5.3

Crustal thickness (in km) calculated by T.Nguuri (2000)

Chapter 6

Upper Mantle Structure Beneath Southern Africa

6.1 Introduction

In the previous chapter receiver functions were used to determine the thickness of the continental crust underneath Southern Africa. Similar techniques can be used to study discontinuities in the upper mantle.

The data used came from 9 of the 10 seismic events recorded by the regional array and used in the previous chapter. The 97168 event from the North Pacific was not used, as stacking it with the 9 Asian events would not be feasible. The seismic waves would reach the stations from a completely different direction, and would therefore pass through different areas of the upper mantle. An ideal study would consider many earthquakes from different areas and then produce stacks of receiver functions for each geographical area, but unfortunately there were not enough events available for such a comprehensive study. It was therefore necessary to ignore the single event from the Pacific and only use the Asian earthquakes. Combining areas for a study of the crust was not a problem, as the Moho is shallow enough to assume lateral homogeneity for the crust around the recording site.

The events were recorded by the regional broad band array stations, and receiver functions were computed from them in 2 minute time windows – from 10 seconds before the P-arrival until 110 seconds after it. Stacks for

individual stations are compiled in Appendix B.

The problem associated with event selection (discussed in Chapter 5) is also going to be present in this chapter. Data used in this study is not sufficient to provide conclusive evidence on any mantle features, but a study will be undertaken with the available data.

The stacks were studied for arrivals of S-waves created when the primary wave passed a significant anomaly in the mantle and a conversion occurs. This would be represented on the receiver function by either a peak, if the wave velocity decreased on its way towards the recording station, or by a trough, if the velocity increased.

From the arrival time of the converted phase, the depth of the discontinuity can be calculated (see section 4.8). To do this it necessary to know how seismic velocities of the P- and S-waves vary with depth – these values were obtained from the IASP91 model (e.g. Kennett & Engdahl 1991; Vasco *et al.* 1994). This model has been developed by Kennett (1991) and contains information about the changes with depth in the upper concerning seismic velocities, density, temperature and other data. The model does not deal with different parts of the Earth, the values in it are considered global averages, and therefore do not necessarily apply to the South African mantle. The results obtained in this chapter will be used to study how the seismic velocities from the Kaapvaal craton compare to the global averages.

The relevant parts of the model are given in Table 6.1, and the P- and S-wave velocities given in it are drawn as a function of increasing depth in Figure 6.1.

Table 6.1

Global average seismic velocities from the IASP91 model

Depth(km)	Vp(km/s)	Vs(km/s)	Depth(km)	Vp(km/s)	Vs(km/s)
0	5.8	3.36	360	8.8475	4.783
20	5.8	3.36	410	9.03	4.87
20	6.5	3.75	410	9.36	5.07
35	6.5	3.75	460	9.528	5.176
35	8.04	4.47	510	9.696	5.282
77.5	8.045	4.485	560	9.864	5.388
120	8.05	4.5	610	10.032	5.494
165	8.175	4.509	660	10.2	5.6
210	8.3	4.518	660	10.79	5.95
210	8.3	4.522	710	10.9229	6.0797
260	8.4825	4.609	760	11.0558	6.2095
310	8.665	4.696	809.5	11.144	6.2474

Using the model and the mathematics from section 4.8, a computer program DEPTH (described in Appendix C) was written to calculate the depth at which a particular converted phase was produced. The assumed Moho depth of the model (35km) can be changed in the program to whatever value was obtained underneath the concerned station in the previous chapter. The model can also be changed as exact details of each discontinuity are calculated.

6.2 The 410-km discontinuity

This is the most significant discontinuity in the upper mantle. It is generally interpreted as a transition in the α-phase to the β-phase of olivine

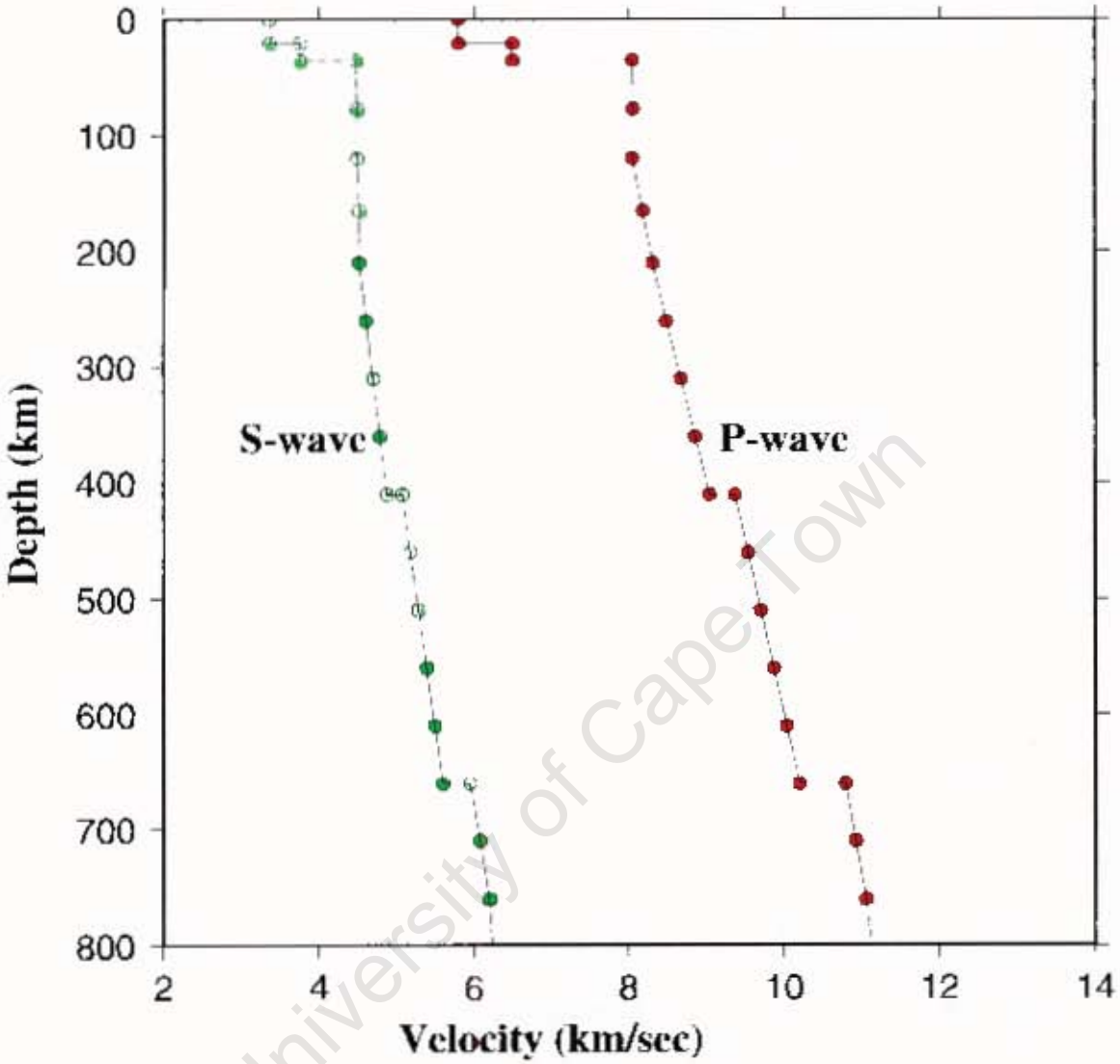

Fig. 6.1

P and S wave velocities as a function of depth from the IASP91 model

$(Mg,Fe)SiO_4$ (Bina & Helffrich 1994). Theoretically this transition should not cause a sharp discontinuity, but could occur over a depth of up to a few kilometers (Shearer & Flanagan 1999). The arrival of the Ps converted phase from that depth (labeled the $P_{410}s$) should be around 40-45 seconds after the P arrival.

Unfortunately the data used were very noisy and only 17 stations could be used for identifying this discontinuity. These stations, and the calculated depths to 410-km discontinuity are listed in table 6.2 below, and the depths (obtained using the global average seismic velocities) are illustrated in figure 6.2.

Table 6.2

Depths to the '410' discontinuity using the IASP91 seismic velocities

Station	Depth (km)	Station	Depth (km)
SA12	403	SA47	397
SA18	399	SA50	399
SA19	390	SA55	403
SA23	403	SA59	394
SA24	400	SA62	406
SA31	398	SA76	413
SA32	401	SA78	413
SA38	389	SA79	411
SA46	391		

Predictably, the peaks implying a Ps conversion at that depth are not nearly as prominent as the ones used to measure the depth of the crust-mantle boundary. The discontinuity is not as clear as the Moho, and the converted

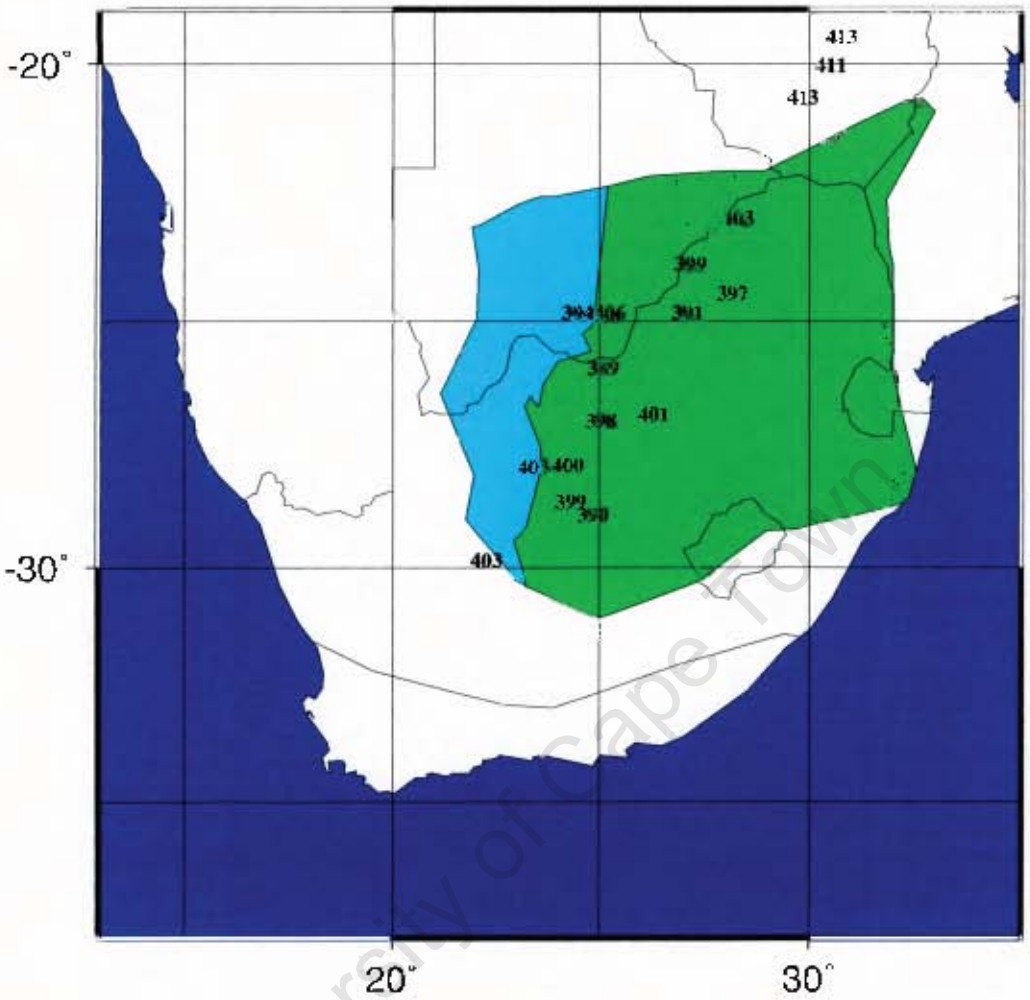

Fig. 6.2

Depths to the 410-km discontinuity calculated using the velocities from the IASP91 model

phase signal had to travel approximately 10 times as far as the ones from the Moho. Some signals (like the ones recorded by SA12 or SA50) were relatively clear to pick, while others were difficult to identify from the background noise. Often in these cases, the frequency of the signal helped to distinguish the peak – the best example of this is SA31. The peak about 41 seconds after the main arrival is not higher than any of the surrounding ones, but there is a clear difference in frequency from the rest of the receiver function, implying that this feature cannot be part of the noise.

It must be stated that the results obtained in this study are not very convincing. A lot more events would have to be studied for a comprehensive study of the mantle from the regional array. The discussion that follows depends entirely on reliable results, and therefore could prove irrelevant.

Unfortunately the only stations off the southern boundary of the Kaapvaal craton that gave a result was SA12, which gave a depth of 403km. Unreliability of most of the southern stations was possibly the most significant shortcoming on the Kaapvaal craton project.

6.2.1 Discussion of Results

The values obtained for stations at the surface of the Kaapvaal craton are very low. This can be interpreted in two different ways – either the 410km discontinuity is shifted upwards by up to 20km, or the wave velocities beneath the craton are up to 5% faster than elsewhere. It is also possible that the anomalous results come from a combination of both these factors.

After obtaining results for the 660km discontinuity it will be possible to determine which of these factors causes the early arrivals of this phase.

The fact that the arrivals of the converted $P_{410}s$ phase are not very prominent could imply that the discontinuity is not a very well defined boundary, but is

in fact a complicated structure underneath some sections of the Kaapvaal craton. Several of the stations (e.g. SA47 and SA59) registered multiple peaks near the expected time of the arrival of this phase – this can be taken as further evidence that in some parts the 410km discontinuity is not sharp.

Only three stations located off the Kaapvaal craton (SA76, SA78 and SA79) produced positive results, and they all registered depths of between 411 and 413km. These stations are placed on the neighbouring Zimbabwe craton. The significant difference in the results for the two cratons implies that the two are very different.

6.3 The 660-km discontinuity

This is the next significant discontinuity in the mantle found throughout the planet. Its nature has been widely discussed, but relatively little is known about it. Even its name has not been universally agreed on – Ringwood and Irifune (1988) refer to the 650-km seismic discontinuity, while Tackley *et al.* (1993) talk about phase transition at 670 km. Collier and Helffrich (1997) call it the "660"km, but claim it can be deeper than 700km.

The most popular theory states that the discontinuity is caused by an isochemical phase transformation of Mg_2SiO_4 spinel to $MgSiO_3$ perovskite plus (Mg,Fe)O magnesiowustite (Shearer 1991). This interpretation permits whole mantle convection to occur freely between upper and lower mantles. An alternative hypothesis (Ringwood & Irfune 1988) maintains that the discontinuity is associated with a change in chemical composition from an overlying upper mantle dominated by Mg_2SiO_4 olivine and spinel minerals, to a relatively silica-rich lower mantle composed essentially of $MgSiO_3$ perovskite. This interpretation implies that the convective systems of the upper and lower parts of the mantle are independent of each other, and are

separated by the 660-km discontinuity.

The solid-solid phase change from spinel to perovskite and magnesiowustite at this discontinuity is unusual in that it is an endothermic phase change, i.e. heat is absorbed when the less dense spinel converts to the more dense perovskite and magnesiowustite (Ito & Takahashi 1989; Schubert & Tackley 1995).

It has been accepted for a long time that the phase change at the 660km depth holds the key to explaining the observations and understanding the dynamical state of the mantle and in particular mantle convection (Machetel & Weber 1991).

Near cold downwellings, some of the phase transformations could occur deeper than in the ambient mantle; if deep enough, the positive buoyancy could prevent downwelling slabs from penetrating into the lower mantle. However, mineral physics experiments and seismological observations indicate that the Clapeyron slope of the phase transition is probably too small to cause long term stratification (Albarede & van der Hilst 1999).

For layering to occur, the intrinsic density of lower mantle material would have to be at least 2% larger than that of the upper mantle (Kellogg *et al.* 1999). Seismological evidence that in the past 200 Myr many slabs of former oceanic plates have penetrated into the lower mantle demonstrates that the density contrast cannot be this large (van der Hilst *et al.* 1997).

Tomographic studies (van der Hilst *et al.* 1997) also provide evidence for a whole-mantle convection system as opposed to two systems separated by a mantle discontinuity. Structural complexity probably persists down up to 1000km (Karason & van der Hilst 2000), but the significance of this depth is not known, and many former oceanic slabs sink even deeper than that.

6.3.1 Results

The arrivals of the Ps conversion from a depth of 660km are expected between 60 and 70 seconds after the P-wave arrival. Once again the arrivals are not very prominent, and only 15 stations produced results. The calculated depths are given in table 6.3 below, and the depths obtained are illustrated in figure 6.3.

Table 6.3

Depths to the '660' discontinuity using the IASP91 seismic velocities

Station	Depth (km)	Station	Depth (km)
SA12	652	SA46	657
SA18	635	SA50	655
SA19	641	SA55	669
SA24	664	SA56	651
SA25	639	SA59	652
SA31	658	SA76	659
SA38	659	SA78	653
SA39	653		

We can see that the depths found on and off the craton are nearly all less than 10km away from the depth of 660km. The three stations near Kimberley: SA18, SA19 and SA25, which all produced values near 640km, are significantly shallower.

Once again there were no results off the southern edge of the Kaapvaal craton, making it impossible to study the mobile belts located there.

Only two stations (SA76 and SA78) on the Zimbabwe craton produced results – values of 659 and 653 km, respectively, were similar to the ones from the Kaapvaal craton.

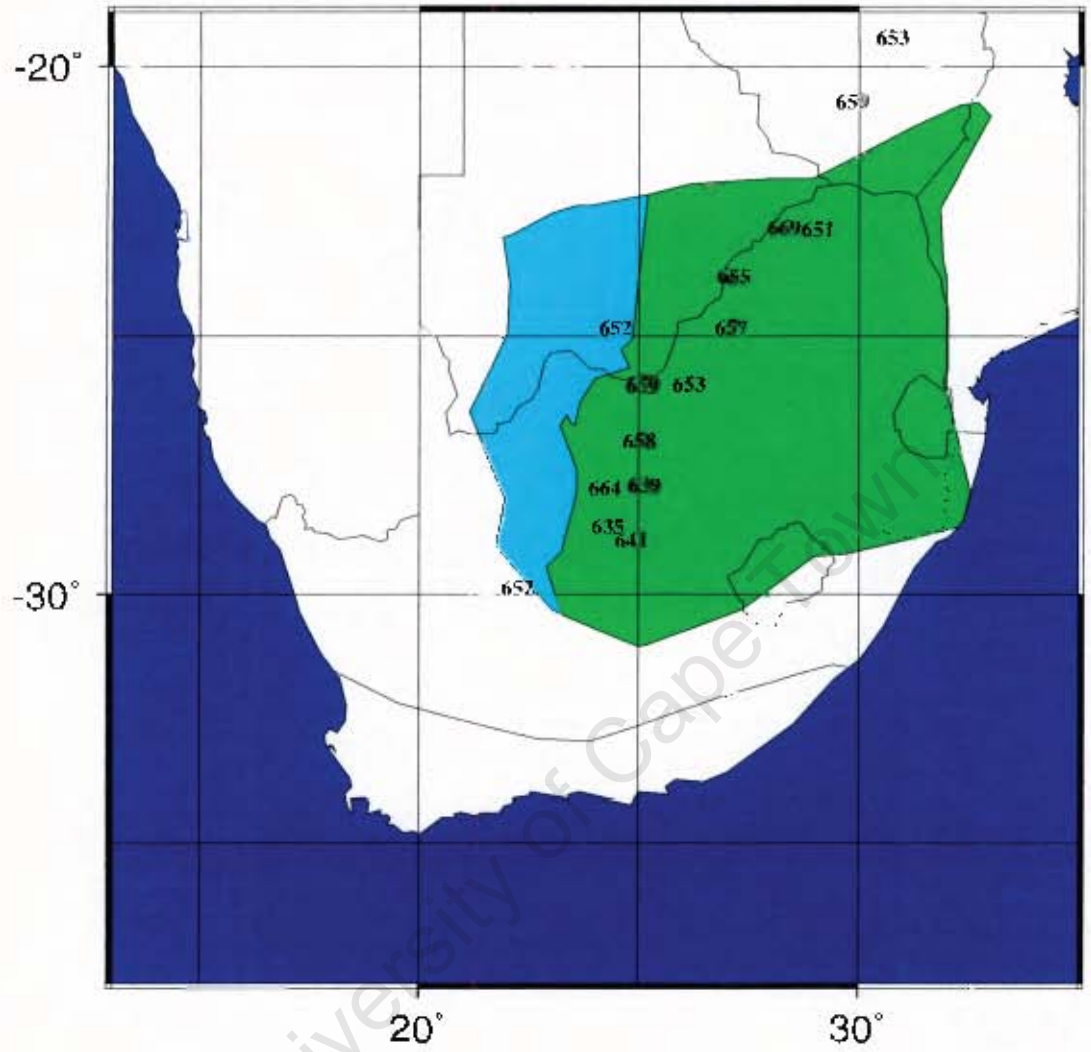

Fig. 6.3

Depths to the 660-km discontinuity calculated using the velocities from the IASP91 model

6.4 The transition zone

6.4.1 Discussion

Due to the chemical nature of the 660-km discontinuity, it is expected to be shifted upwards in regions of high temperature, and downwards if the temperature is below the global average (Schubert & Tackley 1995). This behaviour is the direct opposite to that of the 410-km discontinuity (Bina & Helffrich 1994).

The section of the mantle between these two discontinuities is known as the transition zone (e.g. Nyblade *et al.* 2000). It is clear how the size of this zone is going to depend on the mantle temperature – in hot regions the '410' will be shifted downwards and the '660' upwards, making the transition zone smaller than it would be in cooler regions. This enables us to determine whether the mantle is relatively "hot" or "cold" by calculating the distance between the two discontinuities.

Combining the size of the transition zone with the recorded travel times for the converted phases can be used to determine the velocities of the seismic waves in the region relative to the global averages. For example, assume the $P_{410}s$ phase arrived at the time the IASP91 model predicts it, but an abnormally large transition zone suggests that the discontinuity is elevated. It would then be concluded that the seismic velocities in the region concerned are lower than the global averages, as average velocities would cause the elevated discontinuity to produce early arrivals of the converted phase.

For the stations located on the Kaapvaal craton the $P_{410}s$ arrivals were earlier than expected, while the $P_{660}s$ arrived close to the expected time for most stations (the exceptions being SA18, SA19 and SA25 near Kimberley). Using seismic velocities from the IASP91 model we found the '410' lifted

by up to 20km, and the '660' close to the global average depth. The size of the transition zone was calculated to be between 6 and 20km thicker than the expected 250km, implying a relative low mantle temperature in the region. This thermal anomaly shifts the '410' upwards by up to 10km, and depresses the '660' by approximately the same amount. Comparing this to the depths computed using IASP91, we can see the model made the discontinuities appear closer to the surface than they really are. From this we can conclude that the wave velocities in the craton are higher than the average values given in the IASP91 model by up to 2%.

For the three stations near Kimberley (SA18, SA19 and SA25), however, the $P_{660}s$ arrived earlier than expected by approximately the same time difference that was observed for the $P_{410}s$ phase. This gives an average sized transition zone, which implies a mantle temperature very close to the global average. This in turn means that the two discontinuities should be found at their namesake depths, 410 and 660km, respectively. As the calculated depths are shallower than that by up to 20km, we can conclude that the seismic velocities in the region are higher than the averages from the IASP91 model by up to 5%. The Kimberley region will be studied in more detail in the next chapter.

Over the northern boundary of the Kaapvaal craton, using stations placed on the Zimbabwe craton, the '410' was found very slightly deeper than 410km, while the '660' was just a few km shallower than the depth it is named after. This suggests the upper mantle temperature of the Zimbabwe craton is very slightly (less than 1%) warmer than the global average, while the seismic velocities in that area are close to the averages used in the IASP91 model, as the calculated depths are what is expected from this slight thermal anomaly.

The only station off the Kaapvaal craton that produced results was SA12. It

registered a depth of 403km for the '410' and 652km for the '660'. This gives the size of the transition zone as 249km, just 1km away from the expected 250km. This suggests mantle temperature very close to the global average, and therefore the discontinuities are expected to exist very close to the depths of 410 and 660km, respectively. As they were calculated to be slightly shallower than these values, it can be concluded that the seismic velocities there are higher than the averages from IASP91. It is a very unfortunate shortcoming of the Kaapvaal craton project that only one station off the southern boundary of the craton was reliable enough to produce good results.

6.4.2 Conclusion

The very different results for the Kaapvaal and Zimbabwe cratons confirm that the two cratons are significantly different. Seismic velocities beneath the Kaapvaal craton are faster than beneath the Zimbabwe one, suggesting that the Kaapvaal mantle is denser, and therefore may contain more iron.

Recent studies of the Tanzania craton (Nyblade *et al.* 2000; Owens *et al.* 2000) show that the 410 discontinuity is deflected downwards in that region. From these the authors conclude that the region is relatively warm. This thermal anomaly cannot be explained by convective upwelling induced by passive stretching of the lithosphere. This would lead to small-scale convective instabilities near the base of the lithosphere, but not through the upper mantle (Buck 1986; Mutter *et al.* 1988). The only plausible explanation for the thermal anomaly invokes the presence of a mantle plume, with the bottom of its head reaching across the 410km discontinuity. Fluid dynamic studies of plumes suggest that the heads can be several hundreds of kilometers across (Griffiths & Campbell 1991); so if a plume

head impinged on cratonic lithosphere, it could give rise to the depression of the 410km discontinuity.

It is clear that if the Kaapvaal craton had a mantle plume at the base of its lithosphere, a similar thermal anomaly to the one discussed above would have existed, and would in turn bring down the level of the 410km discontinuity. However, since the discontinuity is brought up underneath the craton, the temperatures concerned are cooler than expected. This implies there are no mantle plumes in the region.

6.5 The 300-km velocity reversal zone

The existence of a low-velocity zone at a depth of about 300km has often been postulated as a feature of Archean cratons (e.g. Vinnik *et al.* 1995). If such a layer exists, it would be bounded on top by a discontinuity, and velocities of waves passing through it on the way to seismic stations would increase as they reach it after passing the low-velocity zone. Because of this unusual velocity-depth relation, the receiver functions would register a negative trough as a sign that a Ps conversion took place. For a depth of 300km these troughs would be expected a little more than 30 seconds after the P-wave arrival.

From the receiver functions included in Appendix B ten stations recorded clearly visible troughs near the expected time. The depths calculated from these arrival times using the IASP91 model are given in Table 6.4 below, and are illustrated in figure 6.4.

As the seismic velocities beneath the craton were shown to be higher than those quoted in the IASP91 model, the depths tabulated above are underestimates by between 5 and 20 km.

Table 6.4

Depths of a possible velocity reversal using the IASP91 seismic velocities

Station	Depth (km)	Station	Depth (km)
SA18	294	SA40	295
SA19	294	SA46	302
SA24	300	SA55	294
SA25	304	SA56	289
SA39	296	SA59	290

With only 10 positive results, this is by no means conclusive evidence for the presence of a low-velocity zone. However, the consistency of these depths and the obvious prominence of some of the troughs recorded (e.g. SA24 and SA40) suggest that the zone does in fact exist from the depth of around 300-310km. As this is a phenomenon of Archean cratons, predictably the evidence for it was not registered by the single active station off the Kaapvaal craton, SA12. It is interesting to note that the stations on the Zimbabwe craton (SA76, SA78 and SA79) also did not register any evidence for the existence of this zone. This further demonstrates the significant difference between the two cratons.

The existence of this anomaly would mean that the results for the 410- and 660-km discontinuities were not precise. By modifying the program to accommodate the velocity reversal it was checked that, depending on the magnitude of the velocity change, the depths obtained in the previous two sections would decrease by only a maximum of 3km. This would not, however, change the size of the transition zone, as the low-velocity zone does not influence velocities below the 410-km discontinuity, and therefore the actual depths of the two discontinuities would not be influenced.

The magnitude of the velocity drop has been estimated by Vinnik *et al.* (1995) to be about 3%. To compensate for this the velocities above this zone should be 1% higher than originally calculated from arrival times of converted phases (as the low-velocity zone has the thickness of approximately 1/3 of the mantle/crust above it). This would make the mantle velocities up to a depth of ~300km in the Kimberley region and other sections of the craton higher than global averages by up to 6% and 3%, respectively. In the low velocity zone these values would drop by the 3% mentioned above – to 3% and 0%, respectively.

A cross-section through the Kaapvaal craton and its surrounding areas illustrating the upper mantle features discussed in this chapter is shown in figure 6.5. The figure also contains percentage values by which the seismic velocities in a particular region differ from the global averages.

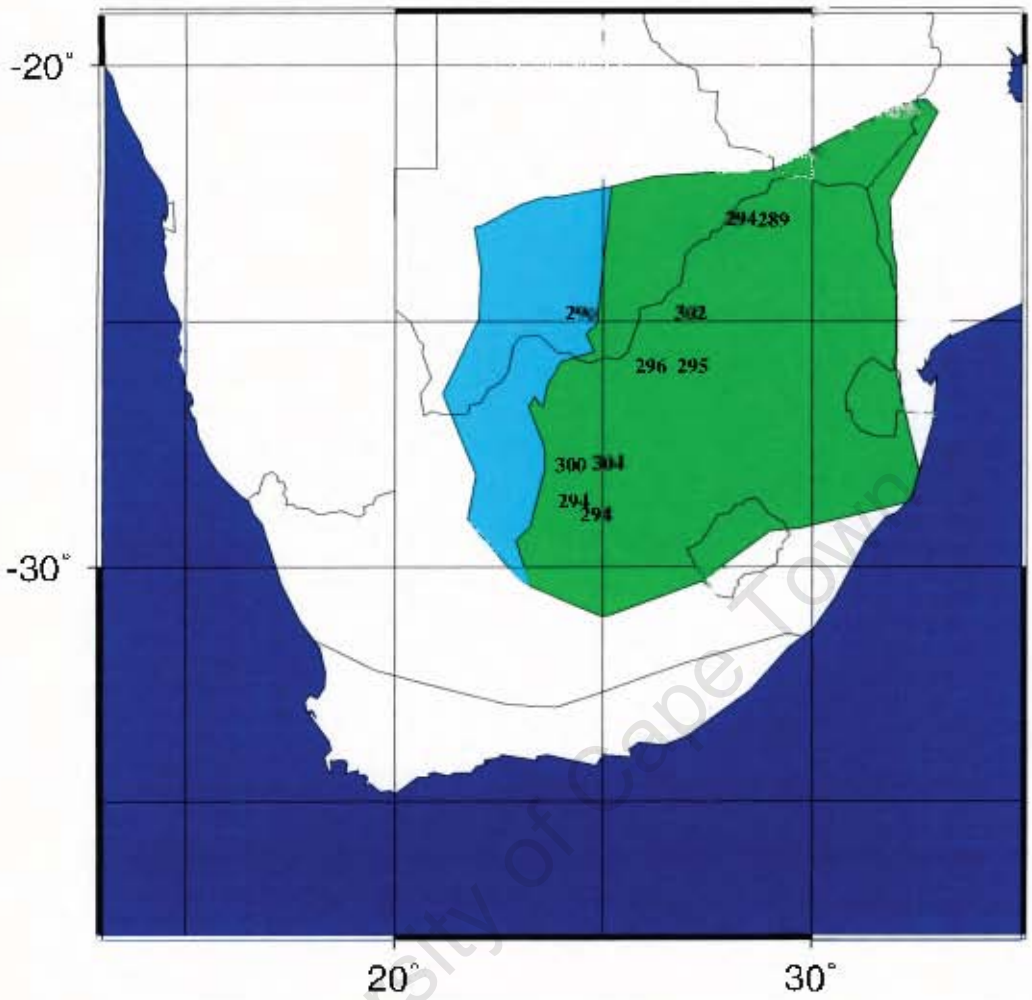

Fig 6.4

Depths of the upper boundary of the low velocity zone, calculated using velocities from the IASP91 model

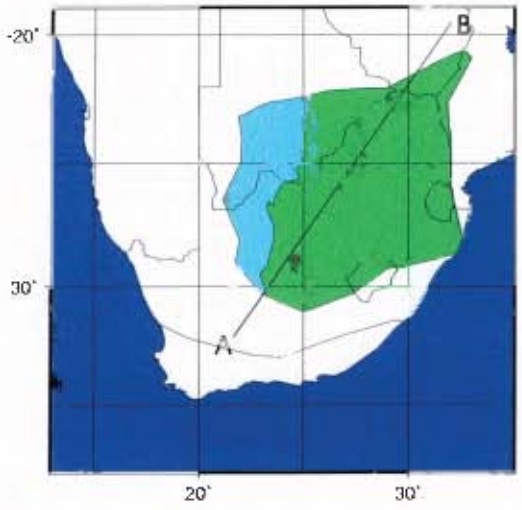

Fig 6.5a

Diagonal along which the cross-section of the craton is shown in b)

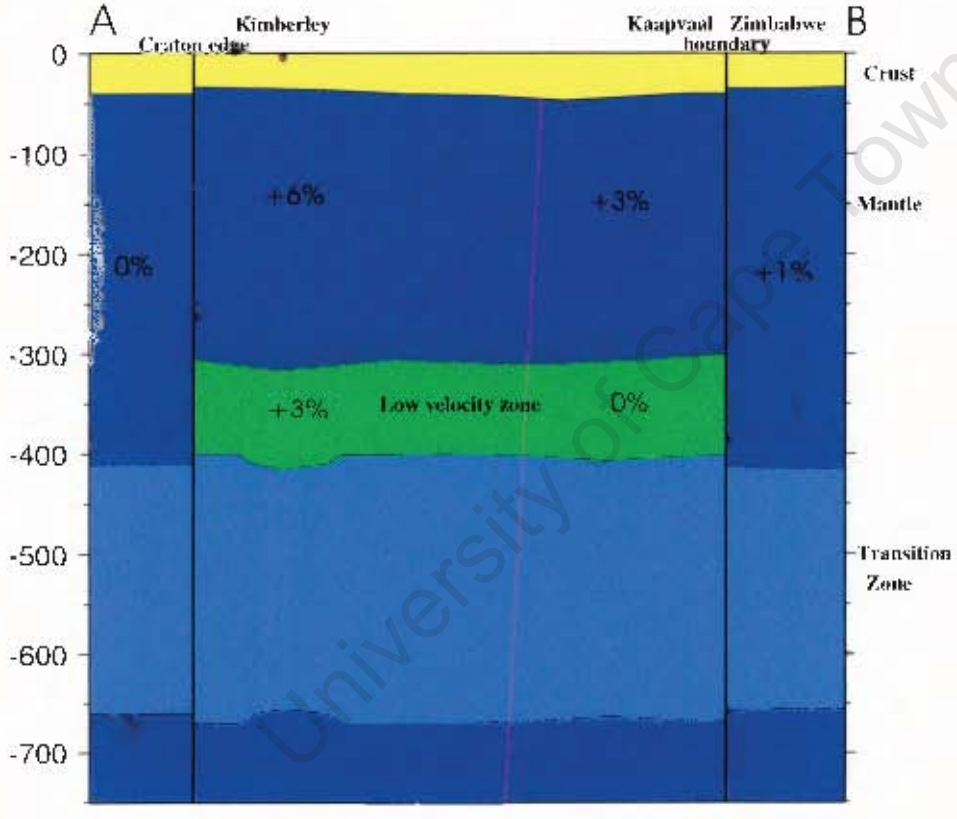

Fig 6.5b

Cross-section of the craton along the diagonal shown in a) using results for the crustal thickness from Chapter 5 and the upper mantle structures discussed in this chapter. Percentages indicate how the velocities in a specific region compare to global averages.

Chapter 7

Study of the Kimberley Area

7.1 The data set

In this chapter the data used comes from the seismic events recorded by the closely-packed array near Kimberley, described in section 3.3 and illustrated in Figure 3.2. The array was deployed for a relatively short time (only 7 months), and only 4 events of quality sufficiently high for the purpose of this study were recorded in that time. However, with 32 stations places in such close proximity (no two stations are more than 50km apart), there were 128 individual traces, over 100 of which were of very good quality and could be used for a comprehensive study. The details of these events are tabulated below, while their locations are shown in Figure 7.1. The ray parameters were computed using the program TTIMS (described in Appendix C) used by Chevrot & Girardin (2000).

Table 7.1

Details of the seismic events recorded by the Kimberley array

Date	Lat.	Long.	Loc.	Depth	Mag.	Ray parameter	Dist.	B.az
99063	28.343N	57.193E	Iran	33km	6.5	0.0587 s/km	64.8	31.4
99087	30.512N	79.403E	Nepal	15km	6.6	0.0495 s/km	78.7	45.8
99093	16.660S	72.662W	Peru	87km	6.2	0.0424 s/km	88.4	251.9
99126	29.501N	51.880E	Iran	33km	6.3	0.0595 s/km	63.6	26.3

The dates used in this table are in the numerical format which was described in section 5.2

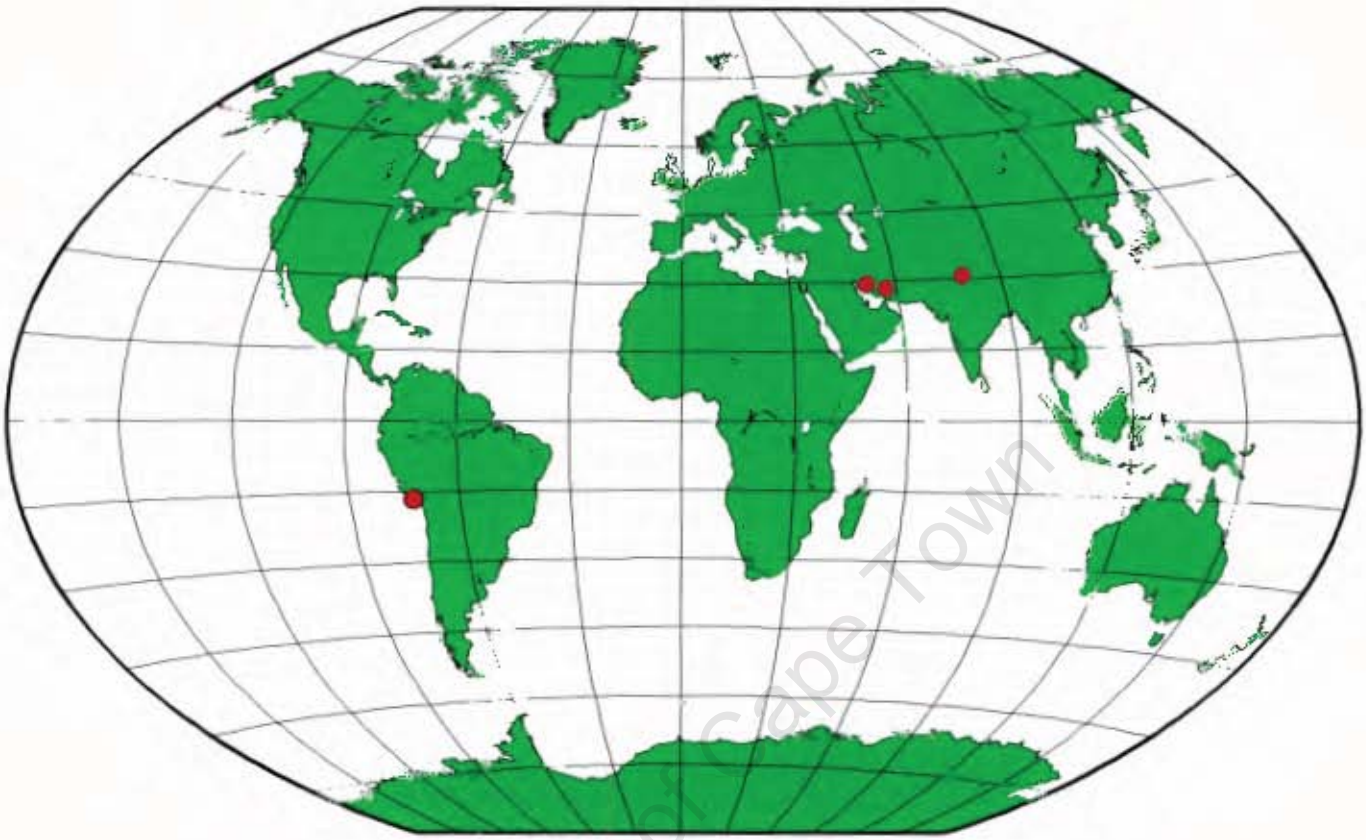

Fig 7.1

Locations of the 4 earthquakes used in this study

7.2 Data processing

The deconvolution process used in this chapter is similar to that described in Chapter 4, but there were some significant differences in the approach. All the data were processed using the Seismic Handler (SH) software, developed at the Seismological Central Observatory at the University of Erlangen by Stammler (1992) as part of his PhD research. This software enables the user to perform various mathematical procedures (such as rotations and deconvolution) on seismographs read into the program. The AH format necessary to read in a seismic record can be obtained from SAC format using the SAC2AH program, which is described in Appendix C.

For each of the four events chosen the three principal components (Z, N and E) were rotated to the L, SV and SH axes. L is along the P-wave principal motion direction, SV, also known as Q, is the P-wave propagation plane and is normal to L, and SH is normal to both L and Q. An additional rotation is performed using an angle that is calculated from the radial and vertical components correlation matrix (Vinnik 1977).

The L component is then deconvolved from the horizontal components using the mathematics introduced in Chapter 4. The deconvolution procedure suppresses the effects of the source (rupture process, magnitude) and of the wave propagation before the converting interface (Chevrot & Girardin 2000). After this operation the resulting Q-component trace is the required receiver function, which contains all the information related to the P-S conversions at the seismic discontinuities beneath the station.

The most significant difference between this approach and the one used earlier in the study, is that the Q-components is devoid of P-wave energy, unlike the radial component which contained a peak representing the arrival of all P-wave energy in the window. It is obviously vital to know the arrival

time of the P-wave with respect to the converted phases, and therefore it is important to align all the Q-traces correctly, since the P arrival is not registered in them. This can be done easily using the T-ORIGIN function with which Seismic Handler is equipped, and which shifts all traces accordingly to align them in phase with each other.

7.3 P-S conversion results

The four events chosen were filtered (high pass at 0.2Hz) to improve the signal to noise ratio, and were then deconvolved using the procedure described above. After all the Q-component traces were aligned to set the arrival of the P-wave at time = 0, they were cut for a time window from 10 seconds before the P arrival up to 100 seconds after it, and were then stacked together for individual events. The resulting four stacks are illustrated in Figure 7.2. These receiver functions are dominated by arrivals of converted phases, as the direct P-wave energy has been mostly eliminated. A clear Ps from the Moho is present in all the stacks at about 5 seconds, while the Ppps and Ppss phases are clearly seen between 15 and 20 seconds.

To study the discontinuities in the upper mantle, a Seismic Handler function STACK was used. This function reads in all the available traces (Q-components in this case) from all the events, and using the locations and depths of the different events as well as exact positions of recording stations, produces a so-called depth stack, which takes into account the varying ray parameters and exact arrival times. This depth stack (Figure 7.3) is a series of stacks computed by varying these parameters for converted phases produced at different depths. Any feature implying a converted phase arrival is expected to be best focused at the stack corresponding to the depth it came from. Prominent arrivals will be seen throughout the depth stack, but will

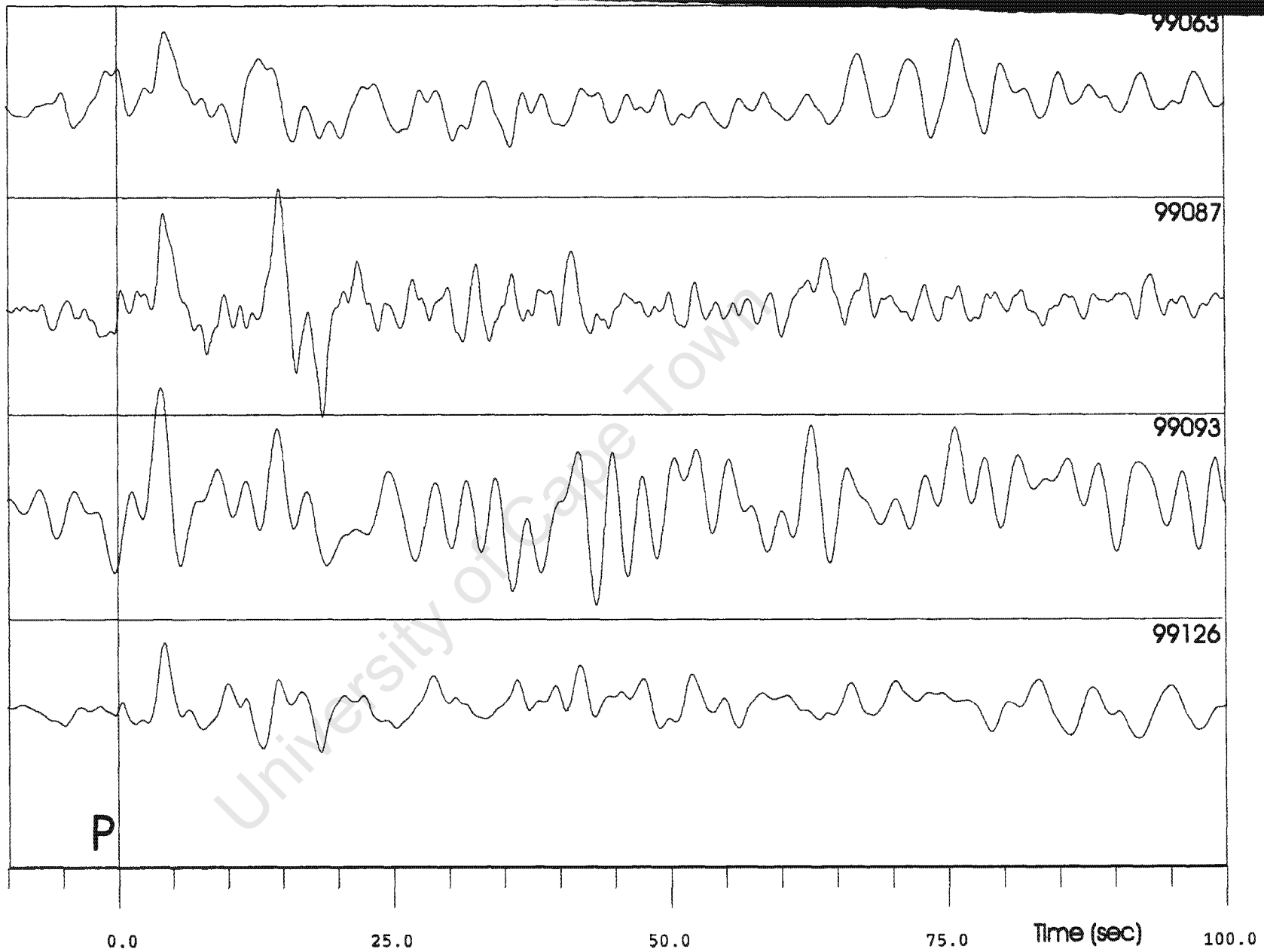

Fig 7.2 Stacks of Q-components of receiver functions of the 99063, 99087, 99093 and 99126 events showing P-S converted phases. The direct P-wave arrival was at 0 seconds, but is not seen as all its energy was in the L-component, perpendicular to Q.

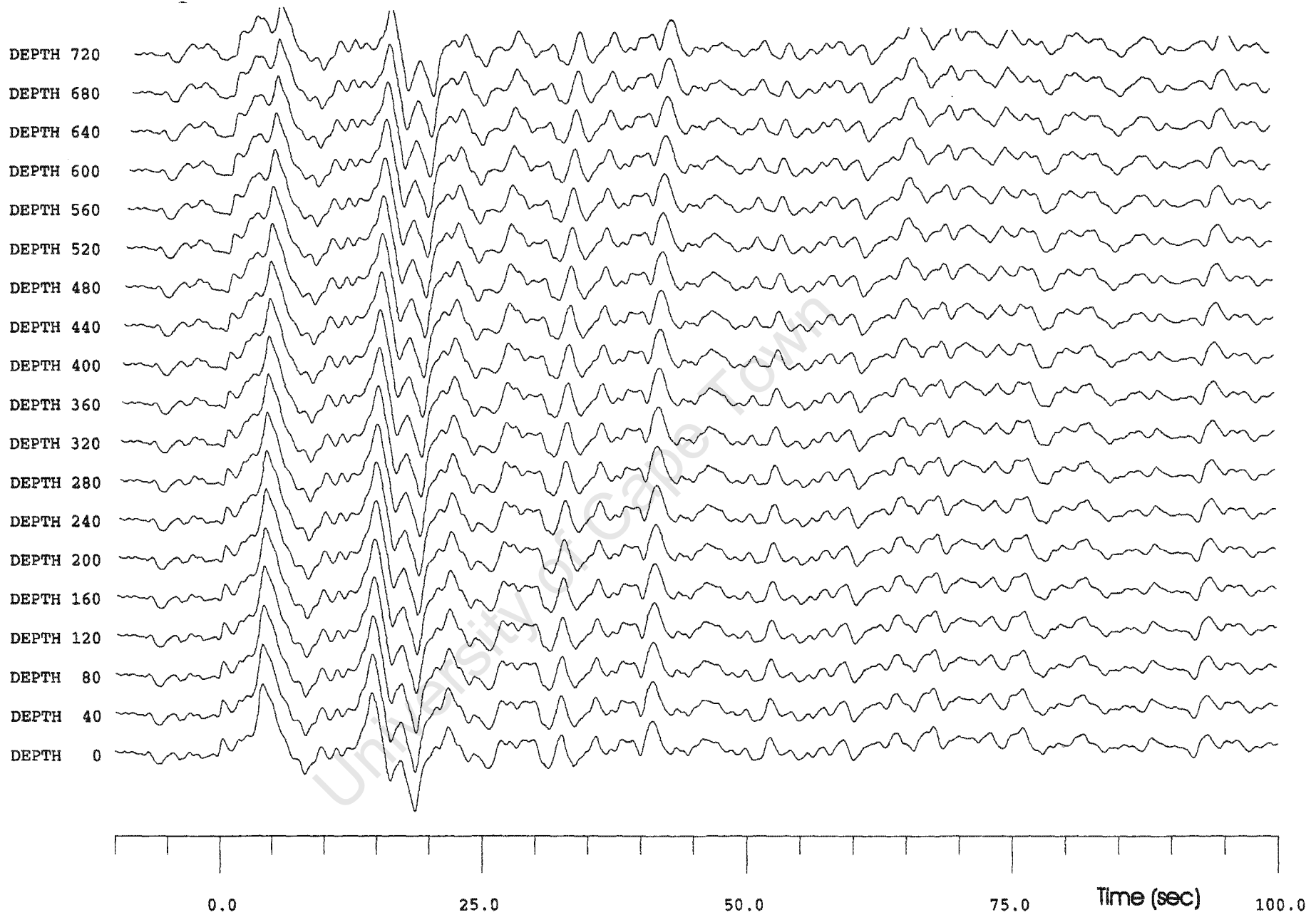

Fig 7.3 P-S conversion depth stack using the 4 events. This stack is actually a series of stacks computed for arrivals of phases produced at different depths. A feature implying an arrival from a certain depth will be best focused at that depth.

still be best defined at the individual stack corresponding to the depth it was produced at. In this study stacks were computed at depth intervals of 40 km.

7.3.1 The Moho

The Ps wave produced at the Moho is the first significant feature of the depth stack. At the 40km stack its arrival was measured at 4.1 seconds. Since the ray parameter of the events has already been taken into account, we can use equation (4.11):

$$h = \Delta t \cdot (v_p \cdot v_s) / (v_p - v_s)$$

Using v_p = 6.5 km/s and v_s = 3.8 km/s we obtain the crustal thickness as 37.3km, which is consistent with the results from Chapter 5, where the Moho depths for the stations near Kimberley were between 36 and 38 km.

The next significant phases are the Ppps and the characteristic trough of Ppss. These were observed at 14.6 and 18.6 seconds respectively. Later in this chapter they will be used to obtain a more accurate crustal thickness, as well as in the calculation for the Poisson ratio of the Kimberley crust.

7.3.2 The transition zone

The $P_{410}s$ phase appears fairly prominently throughout the depth stack. At the stack corresponding to the depth of 400km, its arrival has been timed at 41.9 seconds. The $P_{660}s$ is not very clear at the shallower stacks, but focuses clearly as a peak at 65.7 seconds at the correct depth. These results give the travel time of the converted S-wave through the transition zone as 23.8 seconds. This is exactly the same time as the one found by Vinnik *et al.* (1996b) in their study of the area, having observed the two phase arrivals at 41.8 and 65.6 seconds, respectively.

This time of 23.8 seconds corresponds to the global average predicted by the IASP91 model (Kennett & Engdahl 1991) and confirmed by the global study of Chevrot *et al.* (1999). This implies that beneath Kimberley the 410- and 660-km discontinuities occur very close to their namesake depths. Since the size of the transition zone depends on the mantle temperature (see section 6.4), the average thickness of 250 km implies that this temperature in the region must be close to the global average.

The mantle in the Kimberley region is therefore relatively hotter than in the surrounding cratonic areas (using results from Chapter 6, which were unfortunately not conclusive), but is not unusually hot compared to global measurements. This is therefore consistent with the deduction that the anomalously large heat flow in southern Africa (discussed in section 1.4) is caused by the contents of the crust, and not high mantle temperatures.

The IASP91 model expects the arrivals of $P_{410}s$ phase 44.1 seconds after the primary P-wave arrival, while the global study of Chevrot *et al.* (1999) finds this phase between 41.8 and 49.8 seconds. These variations are caused by different seismic velocities in different regions. All stations set within Precambrian platforms registered this phase earlier than 43 seconds, confirming that in these areas wave velocities are faster than elsewhere. The results obtained in this study imply that the Archean upper mantle beneath Kimberley is fast even by Precambrian standards; in fact the seismic velocities in this region are as fast as anywhere else in the world, and up to 5% faster than the global average.

7.3.3 The velocity reversal zone

This zone could be identified by the presence of an 'inverted' phase arrival. As the velocities increase when they pass across it on the way to the station,

the result would be a trough in the receiver function. Two of these troughs can be seen about 10 seconds before the arrival of the $P_{410}s$ phase. At the correct depth they focus at 31.9 and 34.2 seconds respectively. These times correspond to depths of about 305 and 330 km. The troughs seem sufficiently prominent to suggest that a velocity reversal zone may exist in the Kaapvaal craton. There is no evidence, however, to confirm the claim by Vinnik *et al.* (1996b) that the upper bound of this zone occurs less than 50 km above the 410-km discontinuity. On the contrary, the depth difference found in this study is closer to 100km (105 and 80 km respectively for the two registered troughs).

7.3.4 The 520-km discontinuity

The existence of this discontinuity has been reported very infrequently (e.g. Dueker & Sheehan 1998). It is certainly not a global phenomenon like the 410- or the 660-km ones, and no physical or chemical explanation for its existence has been agreed upon. In this study's depth stack there exists a small peak at 53.3 seconds, which corresponds to a depth of about 530 km. It certainly suggests the presence of a discontinuity, but does not provide conclusive evidence for it, as the peak could be a reverberation of an earlier phase.

7.3.5 Poisson's ratio

The Poisson's ratio σ, is a quantity related to the elasticity of a medium. It is defined as the ratio of lateral contraction to the longitudinal extension of the body when it is placed under stress (Bullen & Bolt 1947). It can be expressed in terms of two Lamé elastic parameters, λ and μ:

$$\sigma = 0.5 * \lambda / (\lambda + \mu) \quad (7.1)$$

By definition a perfectly elastic solid has $\lambda = \mu$, and in this case σ takes on the value of 0.25. A perfect fluid has $\mu = 0$, and therefore $\sigma = 0.5$.

It is possible to express the ratio of primary longitudinal wave velocity to that of a transverse secondary wave. The relation is:

$$(v_p/v_s)^2 = (\lambda + 2\mu)/\mu \quad (7.2)$$

From the two equations Poisson's ratio can be related to the P and S wavespeeds via the following relation:

$$\sigma = 0.5 * \{1 - 1 / [(v_p/v_s)^2 - 1]\} \quad (7.3)$$

It is easy to see that when $(v_p/v_s)^2$ is equal to 3, as is often assumed for studies of the crust (Zandt *et al.* 1995), σ is then 0.25, the value predicted for a perfectly elastic solid.

The ratio provides much tighter constraints on the crustal composition than either the compressional or the shear velocity alone (Chevrot & van der Hilst 2000). Laboratory experiments (Christensen 1996) have shown that many physical and chemical factors may induce variations of the average crustal Poisson's ratio. The abundance of quartz ($\sigma = 0.09$) and plagioclase feldspar ($\sigma = 0.30$) have a dominant effect on the Poisson's ratio of common crustal rocks. An increase of plagioclase content and a decrease of quartz can increase the ratio from 0.24 for a granitic rock to 0.27 for a diorite, to 0.30 for a gabbro (Tarkov & Vavakin 1982). Poisson's ration can therefore be a very useful tool in crustal structure studies.

It was pointed out by Zandt *et al.* (1995) that it is possible to measure the crustal thickness and σ from the analysis of the travel times of the Ps and Ppps phases produced at the Moho discontinuity.

In section 4.8 it was shown that the time difference between the arrival of

the direct P-wave and the Ps phase converted at the Moho is given by:

$$\Delta t = h \cdot [(v_s^{-2} - p^2)^{1/2} - (v_p^{-2} - p^2)^{1/2}] \qquad (7.4)$$

Where h is the crustal thickness and p the ray parameter.

Defining this time difference as t_1 the equation can be rewritten as:

$$t_1 = (h/v_p) \cdot [(v_p^2/v_s^2 - p^2v_p^2)^{1/2} - (1 - p^2v_p^2)^{1/2}] \qquad (7.4a)$$

As this is the difference between the travel times of an S-wave and a P-wave through the crust, the time difference between the Ppps phase (2 P-wave legs and an S-wave leg) and the direct P-wave will be

$$t_2 = (h/v_p) \cdot [(v_p^2/v_s^2 - p^2v_p^2)^{1/2} + (1 - p^2v_p^2)^{1/2}] \qquad (7.5)$$

From these equations it can be seen that the travel times depend on 3 crustal parameters: the P-wave velocity, the v_p/v_s ratio and h, the crustal thickness. A review of seismic refraction studies by Drummond & Collins (1986) gives average crustal P-wave velocities for Archean cratons between 6.4 and 6.5 km/s. This study has shown that the Kimberley area has fast crustal seismic velocities even by Archean standards, so a value of 6.5 km/s was used.

A computer program POISSON, described in Appendix C was then written to examine the variation of theoretical values of t_1 and t_2, as h and v_p/v_s were varied between 20 and 60 km, and between 1.5 and 2.1, respectively. The travel times thus computed were then used to calculate the amplitudes of the receiver function in study, looking for the pair of parameters that would give the highest amplitudes. The result of the program is a matrix whose values are the sum of the amplitudes of t_1 and t_2, while rows and columns correspond to the crustal thickness and the velocity ratio that would produce these particular travel times. By checking the position of the highest value in the matrix, the actual Moho depth and the true v_p/v_s value will be obtained.

Of the four events used, three (99087, 99093 and 99126) had prominent

arrivals of the Ppps phase, and the calculation was performed for each of them. The resulting graphs are shown in Figure 7.4, while the table below shows a summary of the results.

Table 7.2

Results for the crustal thickness and v_p/v_s ratio analysis, uncertainty is the iteration step size

Event	H (km)	v_p/v_s	σ
99087	36 ± 1	1.78 ± 0.02	0.269 ± 0.006
99093	36 ± 1	1.74 ± 0.02	0.253 ± 0.006
99126	35 ± 1	1.78 ± 0.02	0.269 ± 0.006

The results are fairly consistent, giving the average value for Poisson's ratio in the region as

$$\sigma = 0.264 \pm 0.007$$

This is slightly larger than the 0.25 expected for a perfectly elastic solid, but typical for old continental crust. The geological interpretation of this value fall beyond the scope of this study, but an interested reader can find relevant literature on the topic, e.g. Christensen (1996); Clarke & Silver (1993); Zandt & Ammon (1995), Zhu & Kanamori (2000).

The depth of the Moho discontinuity was found around 36 km, consistent with previous results in the study.

7.4 S-P conversions

7.4.1 Introduction

Similarly to a P-wave being partially converted to an S-wave at a discontinuity, an S-wave could produce P-waves under the same circumstances. These converted Sp phases would then travel ahead of the direct S-wave, and reach the receiver a time Δt before it. This time shift would be the same as between a direct P-wave and a converted Ps phase.

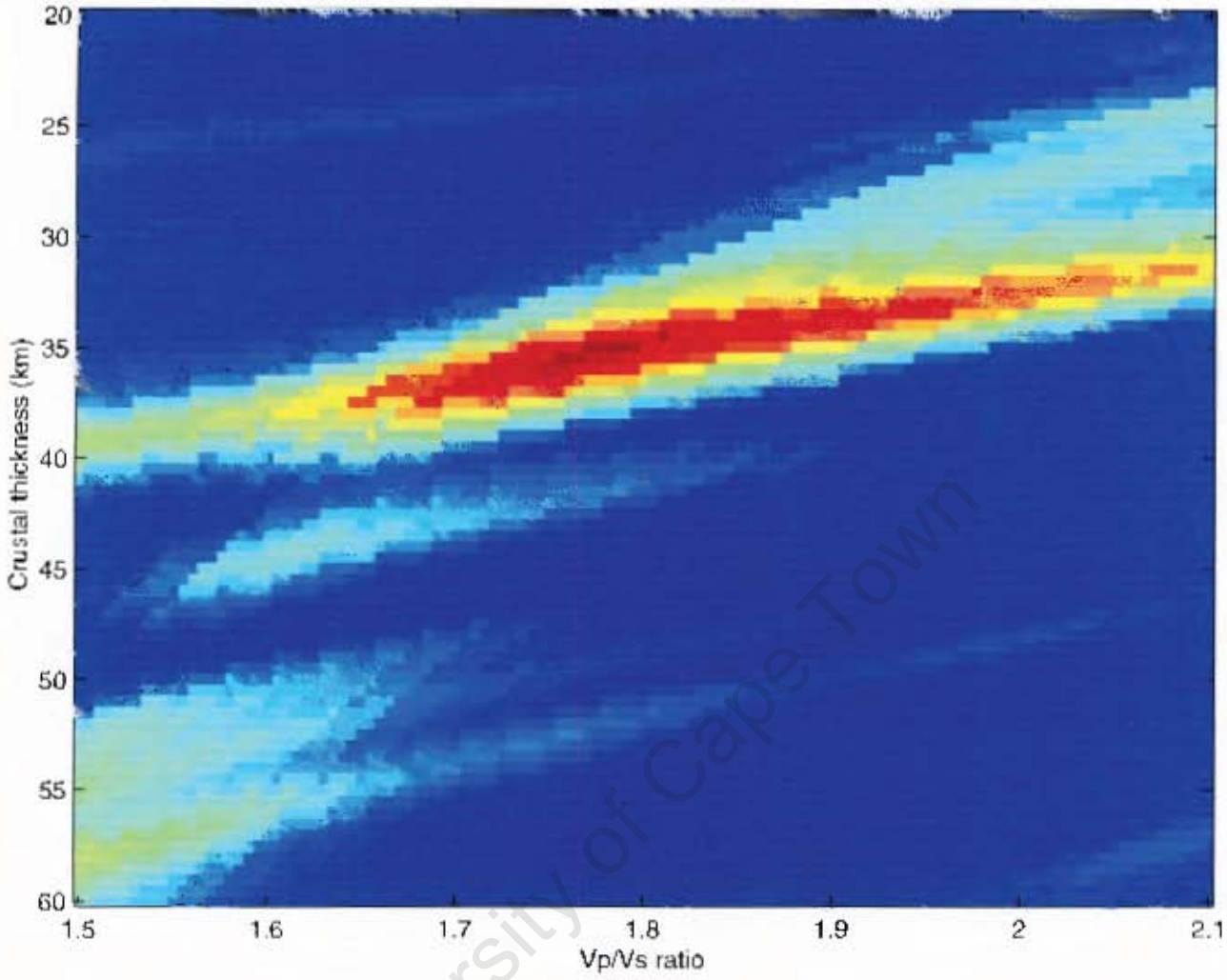

Fig 7.4a

Crustal thickness and Vp/Vs determined using the 99087 event. This diagram is a graphic representation of correlation between a chosen pair of Vp/Vs and crustal thickness values and the true ones for the crust. Cold colours (blue) imply low correlation, while warm colours (red) indicate that the chosen values are close to the real ones.

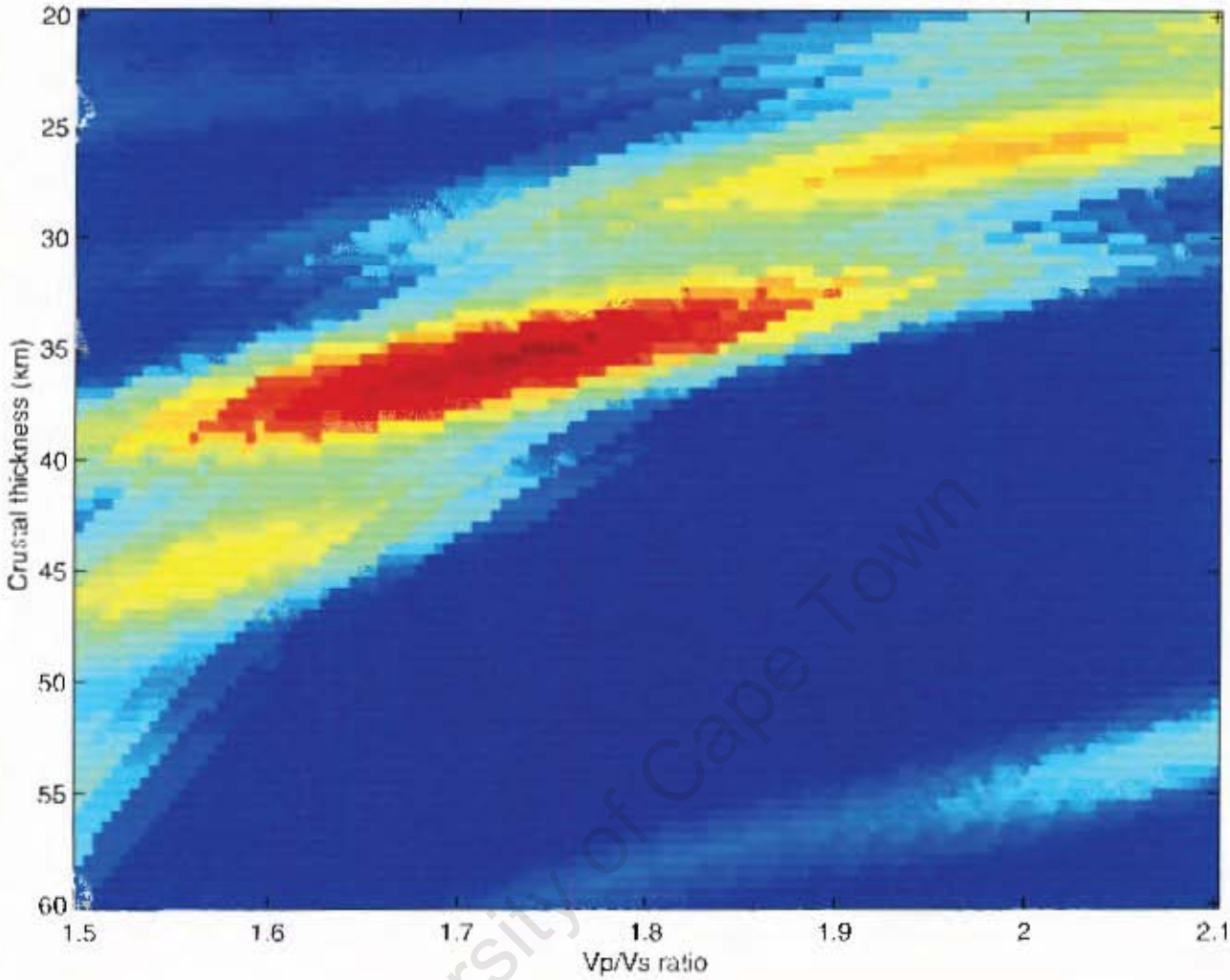

Fig 7.4b

Crustal thickness and Vp/Vs determined using the 99093 event. This diagram is a graphic representation of correlation between a chosen pair of Vp/Vs and crustal thickness values and the true ones for the crust. Cold colours (blue) imply low correlation, while warm colours (red) indicate that the chosen values are close to the real ones.

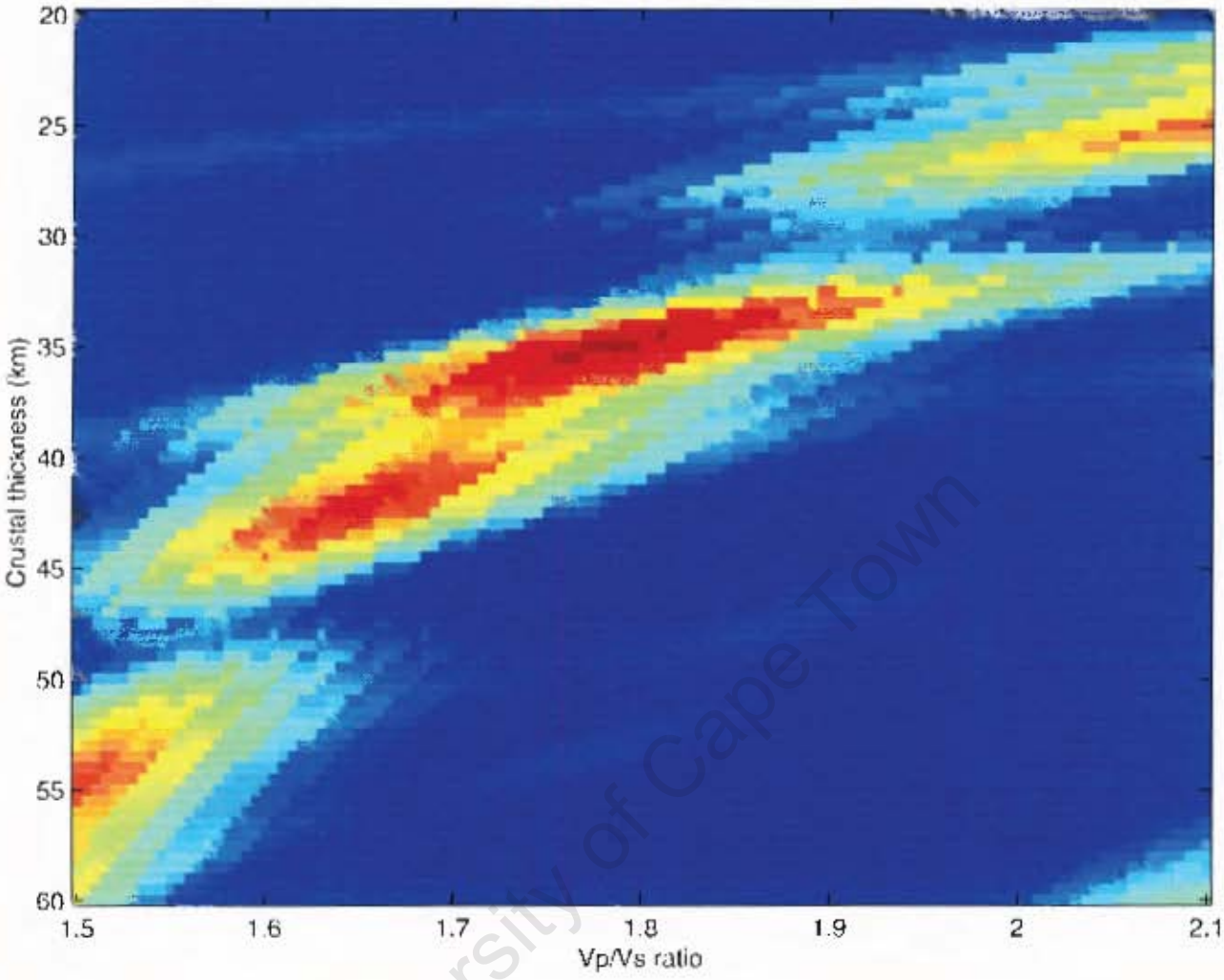

Fig 7.4c

Crustal thickness and Vp/Vs determined using the 99126 event. This diagram is a graphic representation of correlation between a chosen pair of Vp/Vs and crustal thickness values and the true ones for the crust. Cold colours (blue) imply low correlation, while warm colours (red) indicate that the chosen values are close to the real ones.

To identify these phases a different deconvolution process had to be performed. The Q component is the one that contains the direct S-wave energy, so this was deconvolved from the L and SH components, unlike the L that was used in the P-S conversions. The L component was the resultant receiver function, as it was free of S-wave energy and contained all the necessary information about Sp conversions.

The S-P conversions are a lot more difficult to deal with, and very few studies of it have been attempted (e.g. James & Snoke, 1994). It is not known how strong the conversions into P-waves are, and as the direct S-wave arrives much later than the direct P-wave, the converted phases could very easily arrive at about the same time as different reflected P-waves, making their identification very difficult.

7.4.2 Results

The Seismic Handler function STACK was changed slightly to produce a depth stack for the Sp phases from all available L components of the 4 events used in the study. This is shown in Figure 7.5.

The depth stack is not as clear as the one showing the Ps phases (Figure 7.3). However, a clear peak is present at 4.8 seconds, and that strongly suggests a conversion at the Moho. Another prominent peak at 44.1 seconds suggests the arrival of a phase converted at the 410-km discontinuity.

There are many other strong peaks and troughs in the depth stack, but many of these might be arrivals of reflected phases of the P-wave. For a comprehensive study of the S-P conversions one needs a much wider variety of event locations, to provide a variety of different ray parameters. Even then the reflected P-waves will still be present, and unless these can be precisely identified, studies of Sp converted phases will not be very reliable.

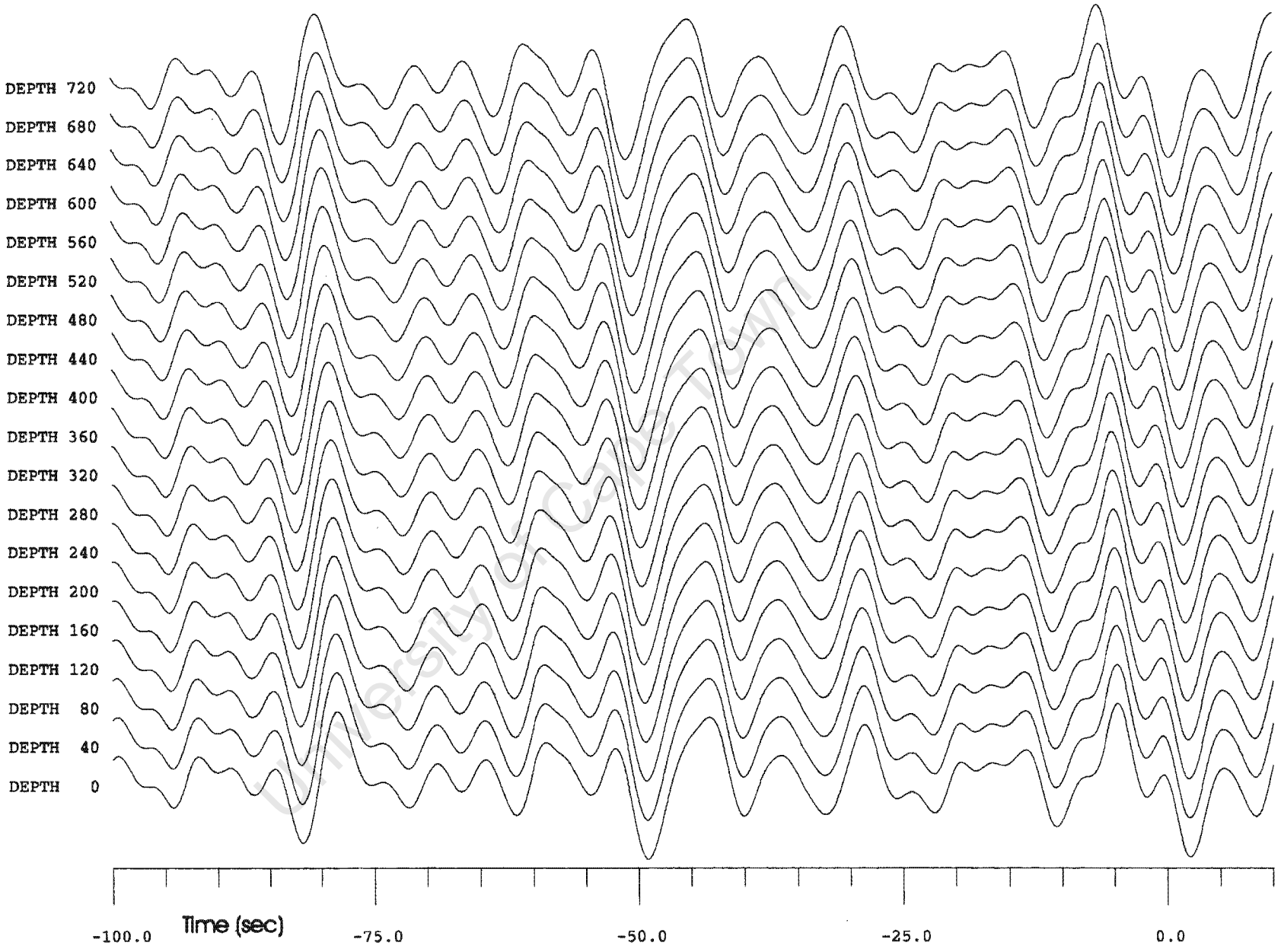

Fig 7.5

S-P conversion depth stack using the 4 events. This stack is actually a series of stacks computed for arrivals of phases produced at different depths. A feature implying an arrival from a certain depth will be best focused at that depth.

Chapter 8

The Kimberley Array as a Tool for Studying Surface Waves

8.1 Non-random noise in seismic events

All recordings of seismic events contain seismic noise as well as the desired seismic data, and separating the two is a very important part of data processing (see section 4.6). Often the noise is random and incoherent, and can be mostly removed by filtering the traces and stacking of receiver functions. However, in some cases the noise is not random. This happens when a different seismic wave passes through the stations at the same time as the main event in study (e.g. Longuet-Higgins 1950; Hasselmann 1963). Most of the time those waves are surface waves, or, when the array is close to the ocean coast, ocean waves (Darbyshire 1950). A major source of noise in broadband seismic records are microseisms generated by wave action along the coast of Africa. These differ from true seismic noise by having shorter periods. Identification of those waves can improve the signal-to-noise ratio of the main event, and also enable us to use the array as a tool for studying these surface waves. This could be very useful, as surface wave tomography is a powerful method of studying deep structures of continents (e.g. Friedrich *et al.* 1998; Simons *et al.* 1999).

By looking at individual Q components recorded by each station for the 99063 event (Fig 8.1), some consistent long period noise is clearly visible. This noise is slightly out of phase at each station, and by considering

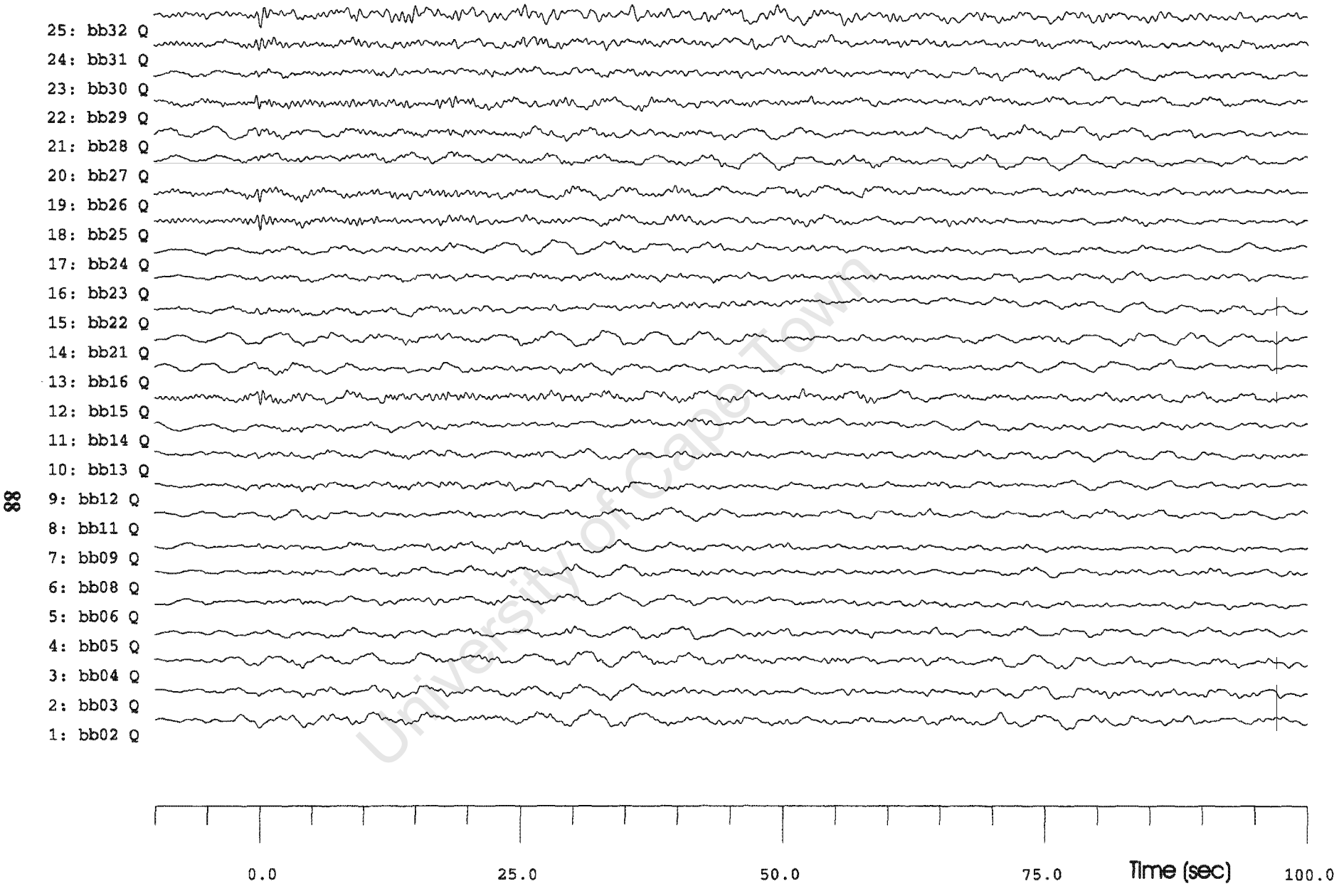

Fig 8.1

Individual Q-components of the 99063 event showing the periodic low frequency noise

positions of each of the stations it is possible to determine the direction the noise is coming from, as well as its velocity. This can only be done if the array concerned is closely packed – if stations were too far apart traces that appear in phase could actually be out by an integer number of phases.

8.2 Response of the array

The response of an array as a function of the wave number **k** corresponds to the ability of the array to study incoming waves corresponding to a specific wave number.

The wave number **k** contains all the necessary information about the wave – its velocity as well as the direction.

$$\mathbf{k} = (k_x , k_y) \qquad (8.1)$$

is a 2-dimensional vector in the horizontal plane, where k_x is the wave number in the E-W direction (West being defined as positive), and k_y the wave number in the N-S axis (North taken as positive).

The velocity of the incoming wave can also be determined from **k**, if its frequency is known. For any given direction

$$k = \omega / c \qquad (8.2)$$

where c is the wave velocity and ω is related to the frequency by the relation

$$\omega = 2\pi f \qquad (8.3)$$

By defining the slowness of a seismic wave as

$$s = 1 / c \qquad (8.4)$$

we get

$$\mathbf{s} = \mathbf{k} / \omega \qquad (8.5)$$

or by using x and y components this can be expressed as

$$(s_x , s_y) = (k_x / \omega , k_y / \omega) \qquad (8.5a)$$

The response of the array is given by:

$$AR(\mathbf{k}) = \Sigma_j \, e^{i[\mathbf{k}\cdot\mathbf{r}_j]} \qquad (8.6)$$

where j is the station index and $\mathbf{r}_j$ is the position vector of each station from an arbitrarily chosen centre of the array (Monzingo & Miller 1980).

The array response is a complex function, but for the purposes of this study only the modulus of its value is needed.

The centre of the Kimberley array was chosen at 28.6 degrees South and 24.7 degrees East (see Fig 3.2). A computer program RESPONSE was written to compute the modulus of the response of this array for k_x and k_y, each varying between –0.5 and 0.5. The program is described in Appendix C, while the result is shown in Figure 8.2.

The response of a perfect array would be a spike at $\mathbf{k} = 0$, and zero for all other wave numbers. Real arrays might have secondary spikes, and any incoming wave with that particular wave number would be very difficult to study using that array. The response of the Kimberley array is very good. There are no spikes other than the centre one that is very narrow (wave numbers greater than 0.1 in any direction are not affected). The fact that it is elliptical in the NE-SW direction could have been predicted. Most stations are aligned in the NW-SE axis, and therefore a wave coming from the NE or SW direction would pass the array faster than one coming from the NW or SE, increasing the inaccuracy of any studies. However, even with this elliptical anomaly, the array response is still very satisfactory.

8.3 Identification of the frequency of the non-random noise

If the long period noise seen in Figure 8.1 is in fact a surface wave not connected with the main event, it would be present in the trace before the P-

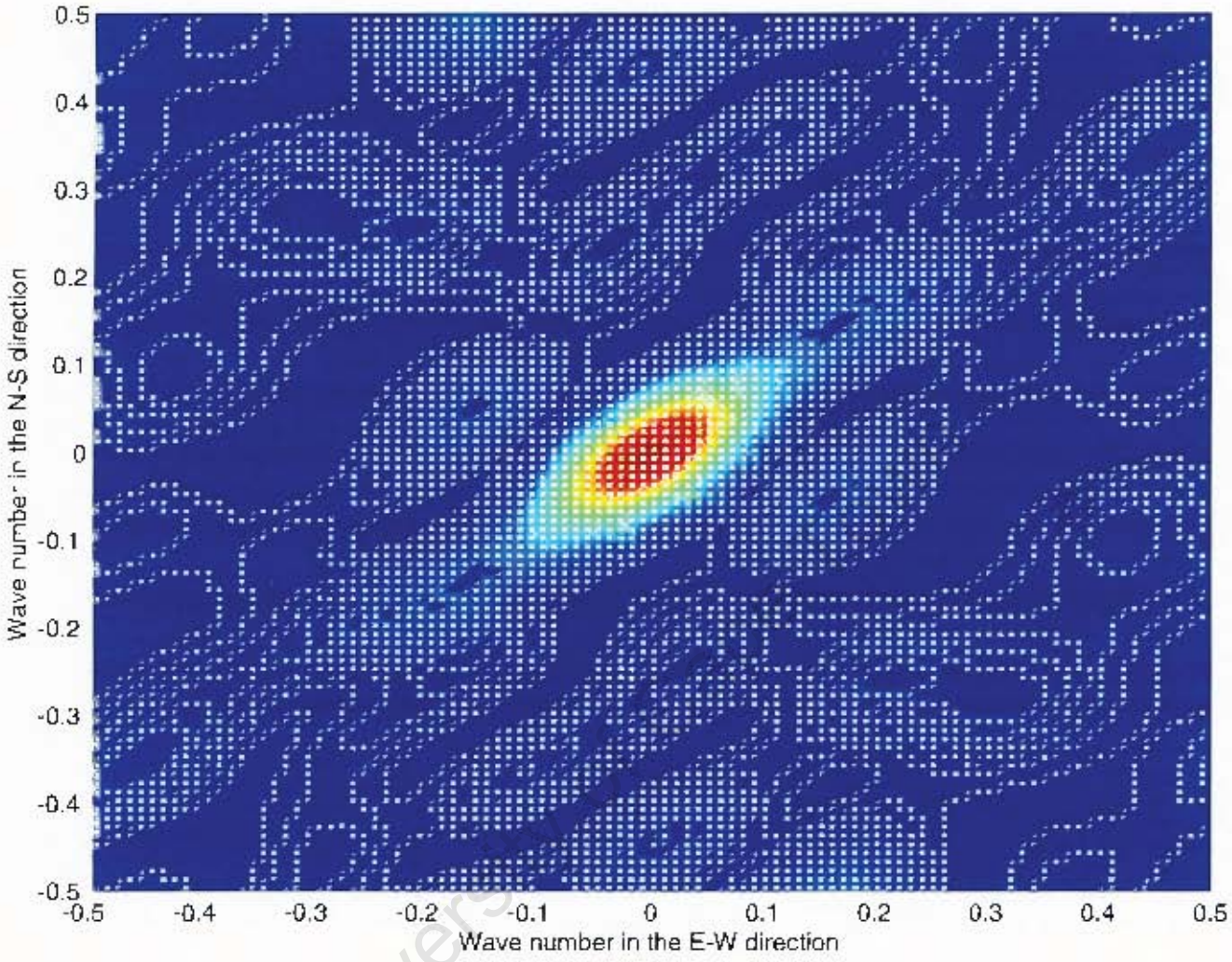

Fig 8.2

Response of the Kimberley array. Cold colours represent low response, while warm ones imply a high value for the response, an anomaly. The peak at the centre of the array was expected, and there are no anomalous secondary peaks.

wave arrival as well as after it. To identify the frequency of the noise and not that of any signal connected with the seismic event, a power spectrum was calculated for the section of the trace before the P-wave arrival. This spectrum can be seen in Figure 8.3.

By studying the power spectrum it is clear that there are in fact two signals of different frequencies present. One of these has a frequency of about 0.07 Hz, and the other about 0.2 Hz. To study these signals separately, two band pass filters were applied to the records: one for frequencies between 0.05 and 0.1 Hz, and the other between 0.1 and 0.3 Hz. The two resulting sets of data, each largely dominated by the surface wave concerned, were then interpreted individually.

8.4 Plane wave beamforming

As the plane wave passes through the array, it will reach each station at a different time. Because of that, the records at each station will be slightly out of phase – these phase shifts could be determined if the velocity and direction of the wave were known. Similarly, by knowing the phase shifts at each of the stations it is possible to determine the wave number, and hence the direction and velocity of the plane wave. This can be done by trying different wave numbers and shifting all traces back by the time shift which would result from this specific wave number. The resulting stacks can then be correlated for being in phase, and the highest correlation coefficient corresponds to the true wave number of the incoming plane wave. This procedure is known as beamforming, or f-k analysis (Jensen *et al.* 1994).

Let us consider this for a given wave number **k**. The angle of the incoming wave corresponding to this **k**, known as the beam steering angle, is given by

$$\theta_s = \text{arctg}\,(k_x / k_y) \qquad \textbf{(8.7)}$$

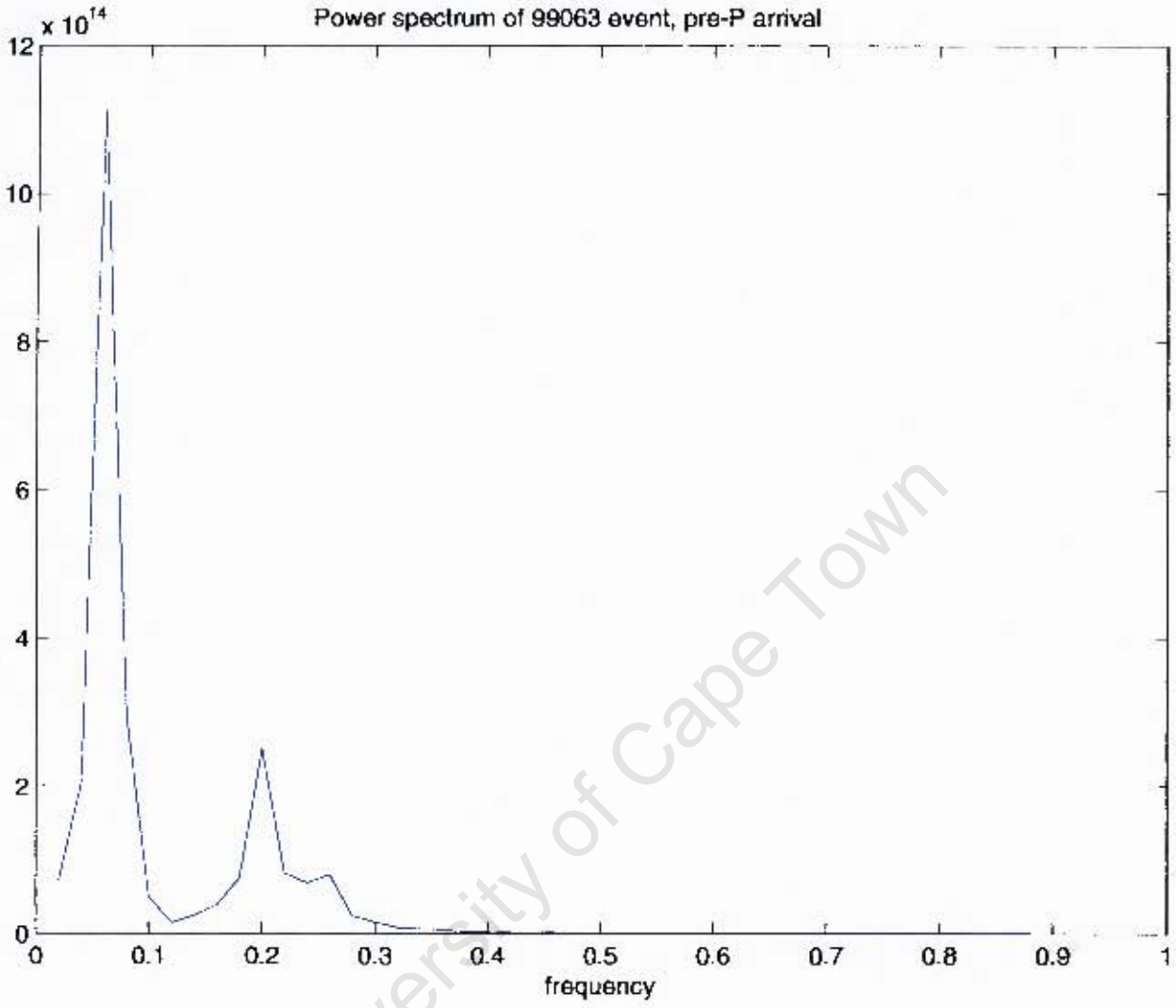

Fig 8.3

Power spectrum of the 99063 event, pre-P-wave arrival.

and consider an incoming plane wave

$$s(\theta) = e^{i[\mathbf{k}\cdot\mathbf{r}]} \qquad \textbf{(8.8)}$$

where θ is the bearing angle associated with the signal, and $\mathbf{r}$ is any point the wave passes through. If the station input at point $\mathbf{r}_j$ is multiplied by the complex conjugate of the plane wave phase factor ω_j, the field will then be summed in phase. This phase factor is given by

$$\omega_j = e^{i[\mathbf{k}\cdot\mathbf{r}_j]} \qquad \textbf{(8.9)}$$

The output of this linear beamforming process is a quadratic form obtained by summing the phase-corrected signal and noise for each station:

$$B(\theta_s) = | \Sigma_j \omega^+_j(\theta_s) [s_j(\theta) + n_j] |^2 \qquad \textbf{(8.10)}$$

Where n_j is the random noise recorded by station j, which makes $[s_j(\theta) + n_j]$ simply the trace recorded by a specific station and ω^+ is the complex conjugate of ω. For more advanced beamforming techniques (not used in this study) see Jensen *et al.* (1994).

8.5 Results

A computer program BEAM (described in Appendix C) was then written to perform the beamforming calculation for different wave numbers. Using the relation between slowness and wave number (equation 8.5), the calculation was done using slowness as the input parameter; s_x and s_y were both varied between the values of –0.5 and 0.5.

8.5.1 The 0.05-0.1 Hz frequency band

For this band each f-k analysis was done for a time window of 128 seconds. This number was chosen so that the window would contain about 10 periods

a back azimuth between 150 and 180 degrees, and slowness between 0.30 and 0.35 s/km. This implies a velocity in the range of 2.9-3.3 km/s.

8.6 Discussion

In the above section the directions and velocities of the external surface waves were determined, and it would be very interesting to find out where they originated. Unfortunately we were not able to do this. It would have been possible, however, if this event was recorded by another dense array. If those records also contained these surface waves, their direction with respect to the other array could have been computed, and combining the results for the two arrays, we would be able to pinpoint the origin of these waves. This technique was successfully used by Friedrich *et al.* (1998) using arrays in Germany and Norway.

The 0.1-0.3 Hz is a typical frequency for microseismic noise generated by coastal waves. It is therefore not surprising that the waves are arriving from the south. The 0.05-0.1 Hz band probably represents a seismic event.

Despite being unable to identify the source of the waves, it is possible to identify what type they are. This can be done by considering the particle motion of the wave, i.e. comparing the radial, transverse and vertical components against each other. To obtain these components, the original E, N and Z components must be rotated not by the azimuth of the main event, but by that of the incoming wave in study.

To do this the most interference-free time windows were chosen. For the 0.05-0.1 Hz band the pre-P-wave window of 0-30 seconds was used, as well as 120-210 seconds window divided into three 30 second sections. For the 0.1-0.3 Hz band the 15-30 seconds (pre-P-wave) as well as the 250-280 seconds divided into two 15 second windows were used.

These selected sections of the records were then rotated, and graphs of the radial component against the transverse, as well as the vertical against the radial, were plotted. These can be seen in Appendix F.

From these graphs it appears that both waves are Rayleigh waves, but the signals are not very clear. For a perfect Rayleigh wave both graphs should by ellipses polarized along the y-axis (Lay & Wallace 1995; Dahlen & Tromp 1998). The vertical/radial graphs all seem to follow that prediction with a little bit of interference clearly visible, while the radial/transverse graphs are even more distorted. These distortions probably result from the fact that there are 2 surface waves present, and while they are not visible in each other's frequency bands, it is inevitable that they will interfere with each other, upsetting their particular motions. Another notable feature of the graphs is the fact that even the clear ellipses are tilted away from the y-axis. This behaviour is normally associated with anisotropy in the region. If anisotropy is in fact present in the region, the velocities of the same wave would be different in different directions. This would cause the particular motion graphs of surface waves to be tilted ellipses (Dahlen & Tromp 1998; Simons *et al.* 1999).

8.7 Conclusion

The purpose of the study in this chapter was to demonstrate how densely packed arrays, such as the one near Kimberley, can be used for studies that cannot be done with regional arrays. These have been shown to include:

- improving signal to noise ratio by eliminating non-random noise,
- identifying this noise for surface wave tomography studies,
- identifying sources of surface waves (if more than one array is available),
- studying the anisotropy in the area.

Chapter 9

Discussion and Conclusion

9.1 Results

In this thesis it was demonstrated how the technique of receiver functions can be used to identify converted phases of the seismic waves, and how these can be used to study the discontinuities in the upper mantle and the depth to the base of the crust.

In the first part of the study the variations in the crustal thickness beneath the craton surface were computed. Off the southwestern boundary of the Kaapvaal craton the values are around 45 km, beneath the southern section of the craton they vary from 37 to 40 km (with two exceptions of 43 and 46 km). Further north the depth increases up to 52 km. North of the Kaapvaal craton (on the Zimbabwe craton) stations record depths between 36 and 40 km. The results follow a similar pattern to those in parallel studies, but some differences were noticed and discussed.

After a study of the transition zone between the 410- and 660-km discontinuities, it was observed that for the most of the craton this zone has a greater than expected thickness, by up to 20km. This implies that the 410-km discontinuity is shifted upwards by up to 10km, and the '660' is depressed by approximately the same amount. From the earlier than expected arrival times it was deduced that the seismic velocities beneath the craton are above the global average. This was to be expected from a study of an Archean craton (Vinnik *et al.* 1995, 1996b). The data for this section of

the study was very limited, and further analysis will be necessary to produce conclusive results.

In the Kimberley region, however, the transition zone had exactly the expected thickness, and therefore the mantle temperature and the positions of the two discontinuities are very close to the global averages. The arrival times imply that the seismic velocities in that region are faster than any other place in the world studied so far. These results were consistent for both arrays used in this study.

The results indicate that there is no positive thermal anomaly in the Kaapvaal mantle, and therefore rule out the possibility of the existence of a mantle plume at the base of the lithosphere (as is the case with the Tanzania craton, e.g. Nyblade *et al.* 2000). The results also reinforce the theory of Hart (1978) that the anomalous heat flow across southern Africa is due to excessive heat production in the crust, and not the asthenosphere.

Eventually it was shown how a close-packed array (like the one near Kimberley) can be used to study surface waves. If the frequency of the wave can be identified (using a power spectrum or any other reliable technique), an f-k analysis can be performed of the data filtered in a narrow frequency band. The results of such analysis would supply the direction as well as the velocity of the incoming wave. This information can be used to study the wave in detail.

If these waves can be identified precisely, deleting them from the records of the main event would be a very efficient way of filtering. This method could enable us to use smaller events in comprehensive studies, if their signal-to-noise ratio can be improved significantly.

9.2 Continuation of the Kaapvaal craton seismic project

Unfortunately the seismic stations used in the Kaapvaal craton project have all been removed, but all the recorded raw data are stored on the IRIS website: www.iris.edu, and a lot of interesting projects can still be done.

The following topics are related to this study and should be used to expand the project in the future:

- Examining the variations in Poisson's ratio throughout the craton,
- A more detailed study of the upper mantle discontinuities for the whole craton. This will be difficult using only the main array, but can be done with sufficiently many events.
- Introducing surface waves to study the deep structure of the craton, using techniques similar to Simons *et al.* (1999).
- A detailed surface wave identification using beamforming to filter as many events from Kimberly as possible, to produce more usable data.

References

Albarede, F. & van der Hilst, R.D., 1999. New mantle convection model may reconcile conflicting evidence, Eos, **80**, 535-539.

Ammon, C.J., 1990. An Overview of receiver function analysis, world wide web address: www.eas.slu.edu/People/CJAmmon/HTML/RftnDocs

Bina, C. & Helffrich, G.R., 1994. Phase transition Clapeyron slopes and transition zone seismic discontinuity topography, J. Geophys. Res, **99**, 15853-15860.

Bostock, M.G. & Cassidy, J.F., 1997. Upper mantle stratigraphy beneath the southern Slave craton, Can. J. Earth Sci., **34**, 577-587.

Boyd, F.R., 1989. Compositional distinction between oceanic and cratonic lithosphere, Earth Planet. Sci. Lett. **96**, 15-26.

Brown, L.F., Benson, J.M., Brink, G.J., Doherty, S., Jollands, A., Jungslanger, E.H.A., Keenan, J.H.G., Muntingh, A. & Van Wyk, N.J.S., 1995. Sequence Stratigraphy in offshore South African Divergent Basins – AAPG studies in Geology # 41. American Association of Petroleum Geologists, Oaklahoma, USA.

Buck, W.R., 1986. Small-scale convection induced by passive rifting: The cause for uplift or rift shoulders. Earth and Planetary Science Letters, **77**, 339-410.

Bullen, K.E. & Bolt, B.A., 1947. An introduction to the theory of seismology. Cambridge University Press, Cambridge.

Carlson, R.W., Grove, T.L., de Wit, M.J. & Gurney, J.J., 1996. Program to study crust and mantle of the Archean craton in southern Africa. Eos, American Geophysical Union, **77**, 273-277.

Carlson, R.W., Boyd, F.R., Shirey, S.B., Janney, P.E., Grove, T.L., Bowring, S.A., Schmitz, M.D., Dann, J.C., Bell, D.R., Gurney, J.J., Richardson, S.H., Tredoux, M., Menzies, A.H., Pearson. D.G., Hart, R.J., Wilson, A.H. & Moser, D., 2000. Continental growth, preservation and modification in Southern Africa. GSA Today, **10**, 1-7.

Chevrot, S. & Girardin, N., 2000. On the detection and identification of converted and reflected phases from receiver functions. Geophys. J. Inst., **141**, 801-808.

Chevrot, S. & van der Hilst, R.D., 2000. The Poisson's ratio of the Australian crust: Geological and geophysical implications, submitted to EPSL.

Chevrot, S., Vinnik, L.P. & Montagner, J.P., 1999. Global-scale analysis of the mantle Pds phases. J. Geophys. Res., **104**, 20203-20219.

Christensen, N.I., 1996. Poisson's ratio and crustal seismology, J. Geophys. Res., **101**, 3139-3156.

Clarke, T.J. & Silver, P.G., 1993. Estimation of crustal Poisson's ratio from broad band teleseismic data, Geophys. Res. Lett., **20**, 241-244.

Collier, J.D. & Helffrich, G.R., 1997. Topography of the "410" and "660" km seismic discontinuities in the Izu-Bonin subduction zone. Geophys. Res. Lett. **24**, 1535-1538.

Corner, B., 1991. Precambrian sedimentary basins of Southern Africa (Terra abstr.) (ed. Eriksson, P.G.) **5** (Blackwell, Oxford).

Dahlen, F.A. & Tromp, J., 1998. Theoretical Global Seismology, Princeton University Press.

Darbyshire, J., 1950. Identification of microseismic activity with sea waves, Proc. R. Soc. Lond. A., **202,** 439-448.

Deuker, K.G. & Sheehan, A.F., 1998. Mantle discontinuity structure beneath the Colorado Rocky Mountains and High Plains, J. Geophys. Res, **103,** 7153-7169.

de Wit, M.J., 1998. On Archean granites, greenstones, cratons and tectonics: does the evidence demand a verdict? Precambrian Res., **91,** 181-226.

de Wit, M.J., Roering, C., Hart, R.J., Armstrong, R.A., de Ronde, C.E.J., Green, R.W.E., Tredoux, M., Peberdy, E. & Hart, R.A., 1992. Formation of an Archean continent. Nature **357,** 553-562.

Dingle, R.V., Siesser, W.G., Newton, A.R., 1983. Mesozoic and Tertiary Geology of Southern Africa, 375pp., A.A. Balkema, Rotterdam, Netherlands.

Drummond, B.J. & Collins, C.D.N., 1986. The nature of the crust-mantle boundary under Australia from seismic evidence, in The Australian lithosphere, pp. 67-80, Geol. Soc. Aust. Spec. Publ.

Friederich, A., Kruger, F., Klinge, K., 1998. Ocean-generated microseismic noise located with the Grafenberg array, J. Seism. **2,** 47-64.

Given, J.W. & Helmberger, D.V., 1980. Upper mantle structure of northwestern Eurasia, J. Geophys. Res., **85,** 7183-7194.

Green, R.W.E. & Durheim, R.J., 1990. A seismic refraction investigation of the Namaqualand metamorphic complex, South Africa, J.Geophys. Res., **95,** 19927-19932.

Griffiths, R.W. & Campbell, I.H., 1991. Interaction of mantle plume heads with the Earth's surface and onset of small-scale convection, J. Geophys. Res., **96,** 18295-18310.

Gurrola, H., Minster, J.B. & Owens, T.J., 1994. The use of velocity spectrum for stacking receiver functions and imaging upper mantle discontinuities, Geophys. J. Int. **117,** 427-440.

Hart, R.J., 1978. A study of the isotopic and geochemical gradients in the Old Granite of the Vredefort Structure, with implications to continental heat flow. Ph.D. thesis at the University of the Witwatersrand.

Hart, R.J., Tredoux, M. & de Wit, M.J., 1997. Refractory trace elements in diamond inclusions: Further clues to the origins of ancient cratons, Geology **25,** 1143-1146.

Harvey, J., 1999. Comparing the azimuthal dependence of the receiver function with crustal features and geology in the South-Western Cape. Unpublished B.Sc.(Hons) thesis at the University of Cape Town.

Hasselmann, K., 1963. Statistical analysis on the generation of microseisms, Rev. Geophys., **1,** 177-210.

Helmberger, D.V. & Wiggins, R.A., 1971. Upper mantle structure of the mid-western United States, J. Geophys. Res., **76,** 3229-3245.

Ito, E., & Takahashi, E., 1989. Postspinel transformations in the system Mg_2SiO_4-Fe_2SiO_4 and some geophysical implications, J. Geophys. Res. **94,** 10637-10646.

James, D.E. & Snoke, J.A., 1994 Structure and tectonics in the region of flat subduction beneath central Peru I: crust and uppermost mantle, J. Geophys. Res. **99,** 6899-6912.

Jensen, F.B., Kuperman, W.A., Porter, M.B. & Schmidt, H., 1994. Computational Ocean Acoustics, AIP press, American Institute of Physics.

Jones, M.Q.W., 1988. Heat flow in the Witwatersrand basin and environs and its significance for the South African shield geotherm and lithosphere thickness. J. Geophys. Res., **93**, 3243-3260.

Jones, M.Q.W. & Bottomley, P., 1986. Geothermal gradients and heat flow in the Witwatersrand basin. Presented at Geocongress '86: The 21st Biennial Congress, Geol. Soc. of S. Afr., Univ. of the Witwatersrand, Johannesburg.

Jordan, T.H., 1975. The continental tectosphere. Rev. Geophys. **13**, 1-12.

Jordan, T.H., 1988. Structure and formation of the continental tectosphere. J. Petrology, **29**, 11-37.

Kárason, H. & van der Hilst, R.D., 2000. Constraints on mantle convection from seismic tomography, Geophysical Monograph **121**, 277-288.

Katsura, T. & Ito, E., 1989. The system Mg_2SiO_4-Fe_2SiO_4 at high pressures and temperatures: Precise determination of stabilities of olivine, modified spinel and spinel. J. Geophys. Res., **94**, 15663-15670.

Kellogg, L.H., Hager, B.H. & van der Hilst, R.D., 1999. Compositional stratification in the deep mantle, Science, **283**, 1881-1884.

Kennett, B., 1991. Seismic velocity gradients in the upper mantle. Geophys. Res. Lett., **18**, 115-118.

Kennett, B. & Engdahl, E.R., 1991. Travel times for global earthquake location and phase identification. Geophys. J. Int. **105**, 429-465.

Kopylova, M.G., Russel, J.K. & Cookenboo, H., 1999. Petrology of peridotite and pyroxenite xenoliths from the Jericho Kimberlite: Implications for the thermal state of the mantle beneath the Slave Craton, Northern Canada. J. Petrology, **40**, 79-104.

Langston, C.A., 1977. The effects of planar dipping structure on source and receiver responses for constant ray parameter, Bull. Seism. Soc. Am., **67**, 1029-1050.

Langston, C.A., 1979. Structure under Mount Rainier, Washington, inferred from teleseismic body waves, J. Geophys. Res., **84**, 4749-4762.

Lay, T. & Wallace, T.C., 1995. Modern Global Seismology, Academic Press, San Diego, California.

Lithgow-Bertelloni, C. & Silver, P.G., 1998. Dynamic topography, plate driving forces, and the African superswell, Nature, **395**, 269-273.

Longuet-Higgins, M.S., 1950. A Theory on the origin of microseisms. Philos. Trans. R. Soc. Lond. A. **243**, 1-35.

Machetel, P., & Weber, P., 1991. Intermittent layered convection in a model mantle with an endothermic phase change at 670km. Nature, **350**, 55-57.

Matthews, P.E., 1990. A plate tectonic model for the Late Archaean Pongola Supergroup in southeastern Africa. In: S.P.H. Sychanthavong (Ed.), Crustal Evolution and Orogeny. Oxford Publ., New Delhi, pp 41 – 73.

McGetchin, T.R., Burke, K.C., Thompson, G.A. & Young, R.A., 1980. Mode and mechanism of plateau uplifts, in Dynamics of Plate Interiors, pp 99-110, AGU and Geol. Soc. Am., Boulder, Colorado.

McNutt, K.M. & Judge, A.V., 1990. The superswell and mantle dynamics beneath the south Pacific, Science **248**, 969-975.

Monzingo, R.A. & Miller, T.W., 1980. Introduction to Adaptive Arrays, Wiley-Interscience, New York.

Morgan, J.W., 1982. Hot spot tracks and the early rifting of the Atlantic, Tectonophysics, **94**, 123-139.

Mutter, J.C., Buck, W.R. & Zehnder, C.M., 1988. Convective partial melting: A model for the formation of thick basaltic sequences during the initiation of spreading, J. Geophys. Res., **93**, 1031-1048.

Nguuri, T., 2000. Mode-converted P-SV and SV-P waves in the solution of problems in crustal evolution, geodynamic processes and exploration. Ph.D. thesis at the University of the Witwatersrand.

Nicolaysen, L.O., Hart, R.J. & Gale, N.H., 1981. The Vredefort radioelement profile extended to supercrustal strata at Carletonville, with implications for continental heat flow. J. Geophys. Res., **86**, 10653-10661.

Nyblade, A.A., Robinson, S.W., 1994. The African Superswell. Geophys. Res. Lett. **21**, 765-768.

Nyblade, A.A., Owens, T.J., Gurrola, H., Ritsema, J. & Langstaon, C.A., 2000. Seismic evidence for a deep upper mantle thermal anomaly beneath east Africa, Geology, **28**, 599-602.

Nyblade, A.A. & Pollack, H.N., 1993. A global analysis of heat flow from Precambrian terrains: Implications for the thermal structure of Proterozoic and Archean lithosphere. J. Geophys. Res., **98**, 12207-12218.

Nyblade, A.A., Pollack, H.N., Jones, D.C., Podmore, F. & Mushayandebvu, M., 1990. Terrestrial heat flow in east and southern Africa, J. Geophys. Res., **95**, 17371-17384.

Owens, T.J., Nyblade, A.A., Gurrola, H. & Langston, C.A., 2000. Mantle transition zone structure beneath Tanzania, east Africa, Geophys. Res. Lett., **27**, 827-830.

Owens, T.J., Taylor, S.R. & Zandt, G., 1987. Crustal structure at regional seismic test network stations determined from inversion of broadband teleseismic P waveforms, Bull. Seism. Soc. Am., **77**, 631-662.

Owens, T.J., Crosson, R.S. & Hendrickson, M.A., 1988. Constraints on the subduction geometry beneath western Washington from broadband teleseismic waveform modeling, Bull. Seism. Soc. Am., **78**, 1319-1334.

Parman, S.W., Dann, J.C. & Grove, T.L., 2001. The production of Barberton komatiites in an Archean subduction zone, submitted to Geophys. Res. Lett.

Phiney, R.A., 1964. Structure of the Earth's crust from spectral behaviour of long-period waves, J. Geophys. Res., **69**, 2997-3017.

Ringwood, A.E. & Irifune, T., 1988. Nature of the 650-km seismic discontinuity: implications for mantle dynamics and differentiation, Nature **331**, 131-136.

Ryabov, V., 1989. Review of crustal-upper mantle structure beneath IRIS stations in the USSR, Internal Report, Center for Seismic Studies, Arlington, VA.

Schimmel, M. & Paulssen, H., 1997. Noise reduction and detection of weak, coherent signals through phase weighted stacks. Geophys. J. Int., **130**, 497 – 505.

Schubert, G. & Tackley, P.J., 1995. Mantle dynamics: The strong control of the spinel-perovskite transition at a depth of 660km, J. Geodynamics, **20**, 417-428.

Shearer, P.M., 1991. Constraints on upper mantle discontinuities from observations of long-period reflected and converted phases, J. Geophys. Res. **96,** 18147-18182.

Shearer, P.M. & Flanagan, M.P., 1999. Seismic velocity and density jumps across the 410- and 660-kilometer discontinuities. Science, **285,** 1545-1548.

Sheriff, R.E. & Geldart, L.P., 1982. Exploration Seismology, Vol. 1, pp. 82-101, Cambridge University Press, New York.

Simons, F.J., Zielhuis, A. & van der Hilst, R.D., 1999. The deep structure of the Australian continent from surface wave tomography, Lithos, **48,** 17-43.

Stammler, K., 1992. Seismic Handler, User's Manual, attachment to PhD thesis at the Seismological Central Observatory, University of Erlangen.

Stein, C.A & Stein, S., 1992. A model for the global variation in oceanic depth and heat flow with lithospheric age. Nature **359,** 123-129.

Tapley, W.C. & Tull, J.E., 1992. SAC – Seismic Analysis Code USER'S MANUAL. Regents of the University of California.

Tackley, P.J., Stevenson, D.J., Glatzmaier, G.A & Schubert, G., 1993. Effects of an endothermic phase transition at 670 km depth in a spherical model of convection in the Earth's mantle. Nature, **361,** 699-704.

Tankard, A.J., Jackson, M.P.A., Eriksson, K.A., Hobday, D.K., Hunter, D.R. & Minter, W.E.L., 1982. 3.5 Billion Years of Crustal Evolution of South Africa. New-York: Springer-Verlag.

Tarkov, A.P. & Vavakin, V.V., 1982. Poisson's ratio behaviour in crystalline rocks: application to the study of the Earth's interior, Phys. Earth Planet. Inter., **29,** 24-29.

Van der Hilst, R.D., Widiyantoro, S. & Engdahl, E.R., 1997. Evidence for deep mantle circulation from global tomography, Nature, **386,** 578-584.

Vasco, D.W., Pulliam, R.J., Johnson, L.R. & Earle, P.S., 1994. Robust inversion of IASP91 travel time residuals for mantle P and S velocity structure, earthquake mislocations and station corrections, J. Geophys. Res. **99,** 13727-13755.

Vinnik, L.P., 1977. Detection of waves converted from P to SV in the mantle, Phys. Earth planet. Inter., **15,** 39-45.

Vinnik, L.P., Green, R.W.E. & Nicolaysen, L.O., 1995. Recent deformation of the deep continental root beneath southern Africa, Nature, **375,** 50-52.

Vinnik, L.P., Green, R.W.E. & Nicolaysen, L.O., 1996a. Seismic constraints of the mantle of the Kaapvaal craton, Phys. Earth Planet. Interiors, **95,** 139-151.

Vinnik, L.P., Green, R.W.E., Nicolaysen, L.O., Kosarev, G.L. & Petersen, N.V., 1996b. Deep seismic structure of the Kaapvaal craton, Tectonophysics, **262,** 67-75.

Welke, H. & Nicolaysen, L.O., 1981. A new interpretive procedure for whole rock U-Pb systems applied to the Vredefort crustal profile. J. Geophys. Res., **86,** 10681-10687.

Wessel, P. & Smith, W.H.F., 1991. Free software helps map and display data, EOS Trans. Amer. Geophys. U., vol. 72(41), pp. 441.

Wessel, P. & Smith, W.H.F., 1995a. New version of the Generic Mapping Tools released, EOS Trans.Amer.Geophys. U., vol. 76(33), pp. 329.

Wessel, P & Smith, W.H.F., 1995b. New version of the Generic Mapping Tools released, EOS Trans.Amer.Geophys. U. electronic supplement, www.agu.org/eos_elec95145e.html

Wessel, P. & Smith, W.H.F., 1998. New, improved version of Generic Mapping Tools released, EOS Trans. Amer. Geophys. U., vol. 79(47), pp. 579.

Yilmaz, O., 1987. Seismic Data Processing, Vol. 2, investigations in Geophysics, Society of Exploration Geophysics, Tusla, OK.

Zandt, G. & Ammon, C.J., 1995. Continental crust composition constrained by measurements of crustal Poisson's ratio, Nature, **374**, 152-154.

Zandt, G., Myers, S.C. & Wallace, T.C., 1995. Crust and mantle structure across the Basin ond Range-Colorado plateau boundary at 37 degrees N latitude and implications for Cenzoic extensional mechanism, J. Geophys. Res., **100**, 10529-10548.

Zhu, L., and Kanamori, H., 2000. Moho depth variation in southern California from teleseismic receiver functions, J. Geophys. Res., **105**, 2969-2980.

Appendix A

Stacks of receiver functions for individual stations used to study the crustal thickness in Chapter 5.

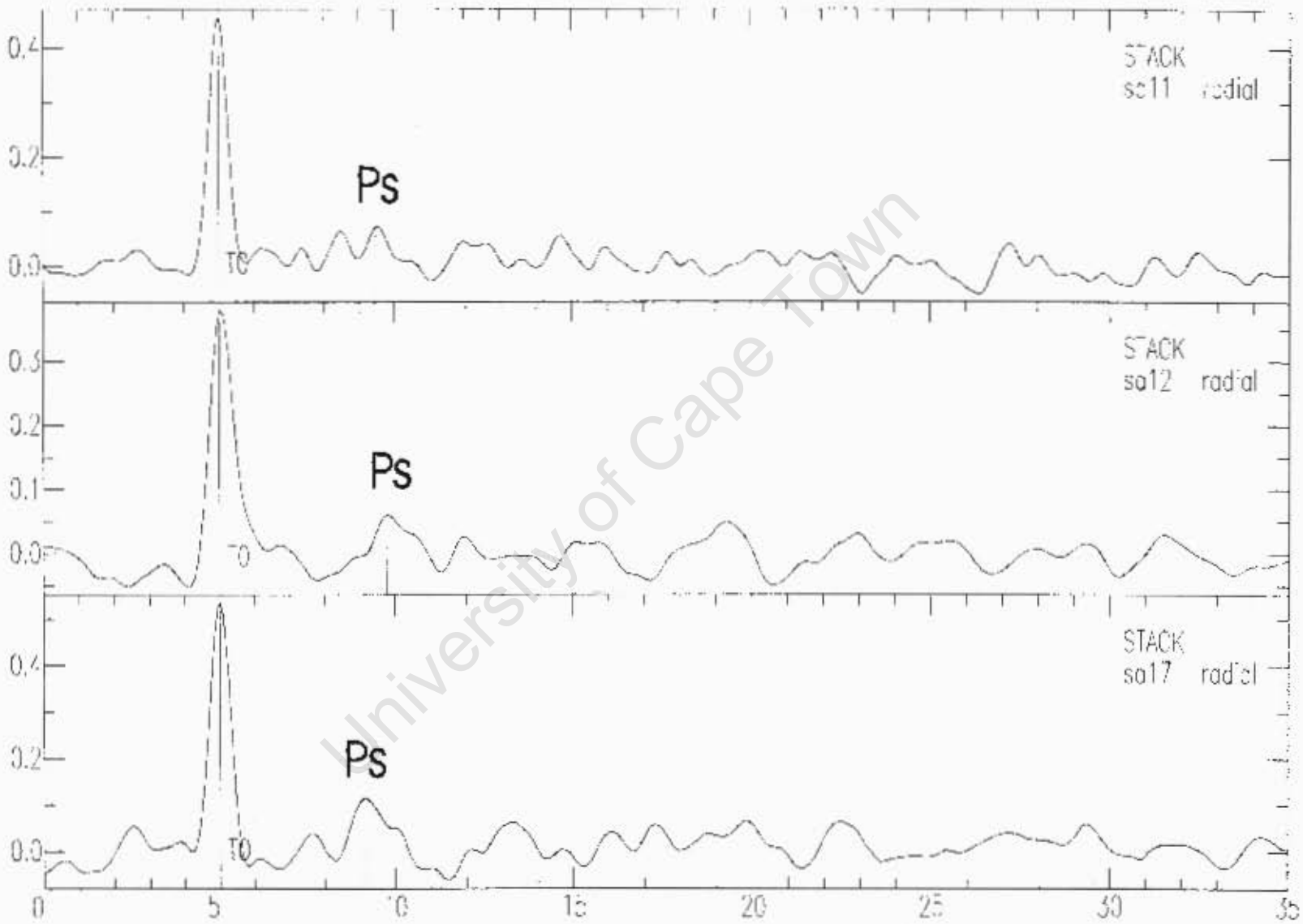

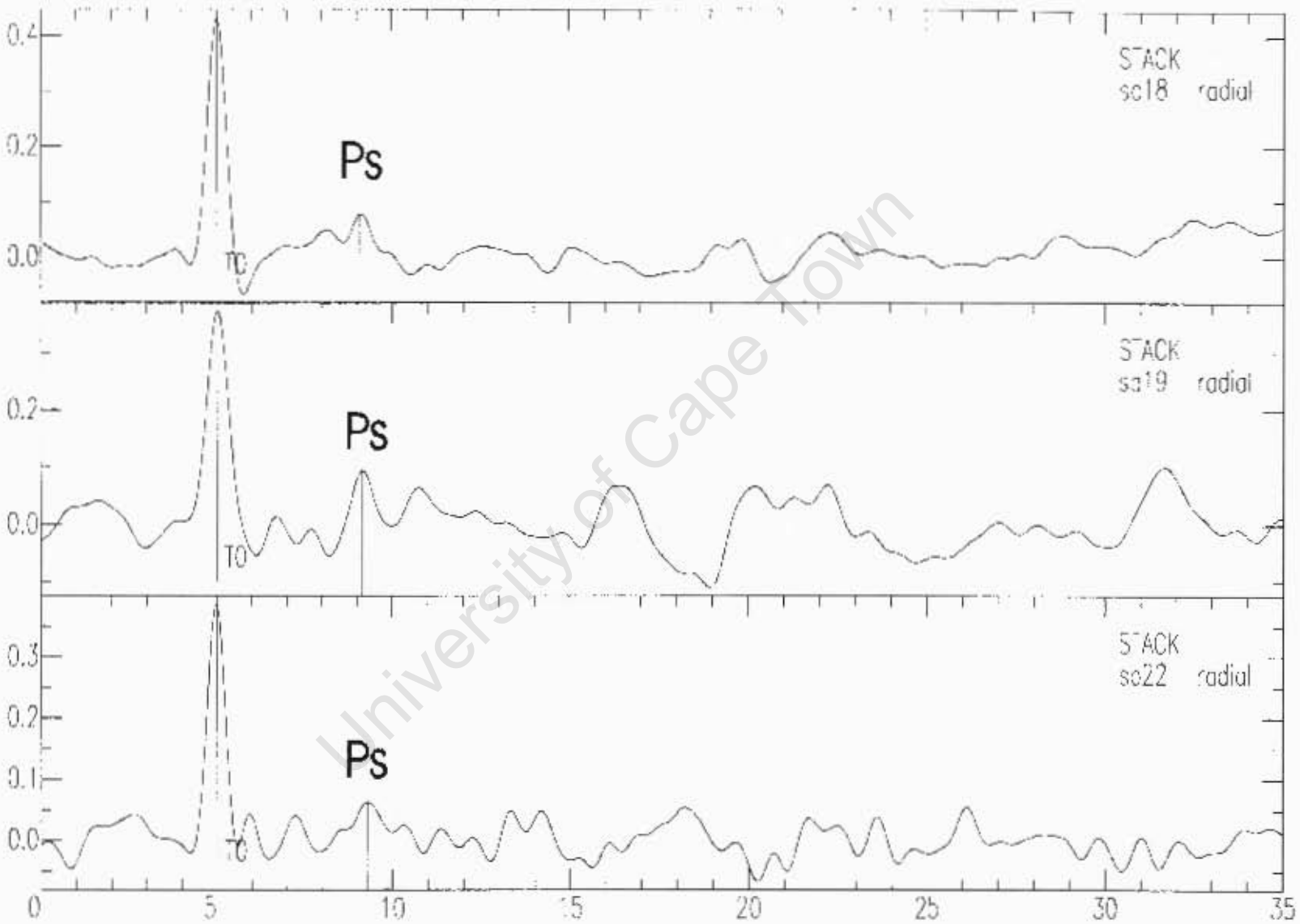

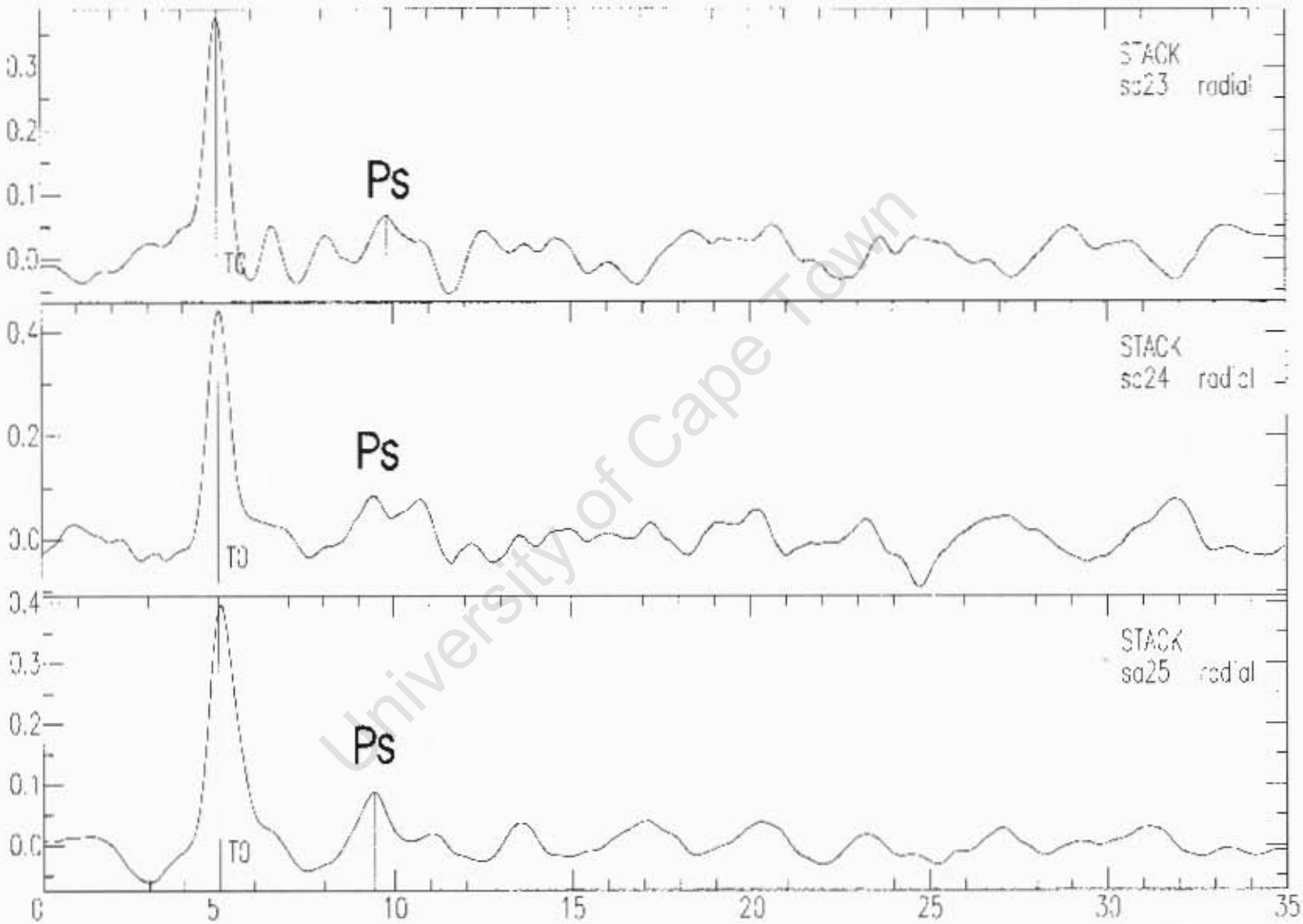

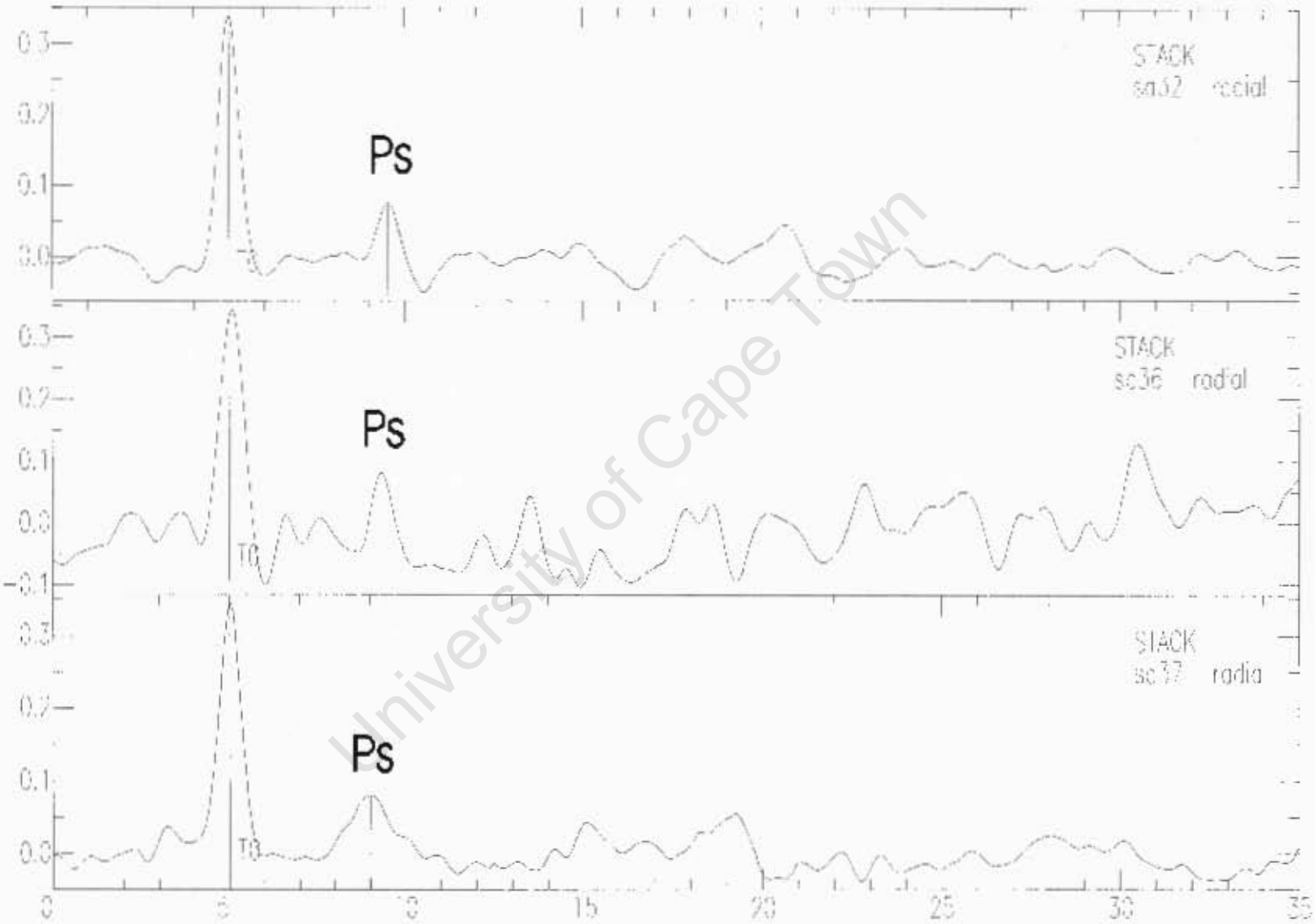

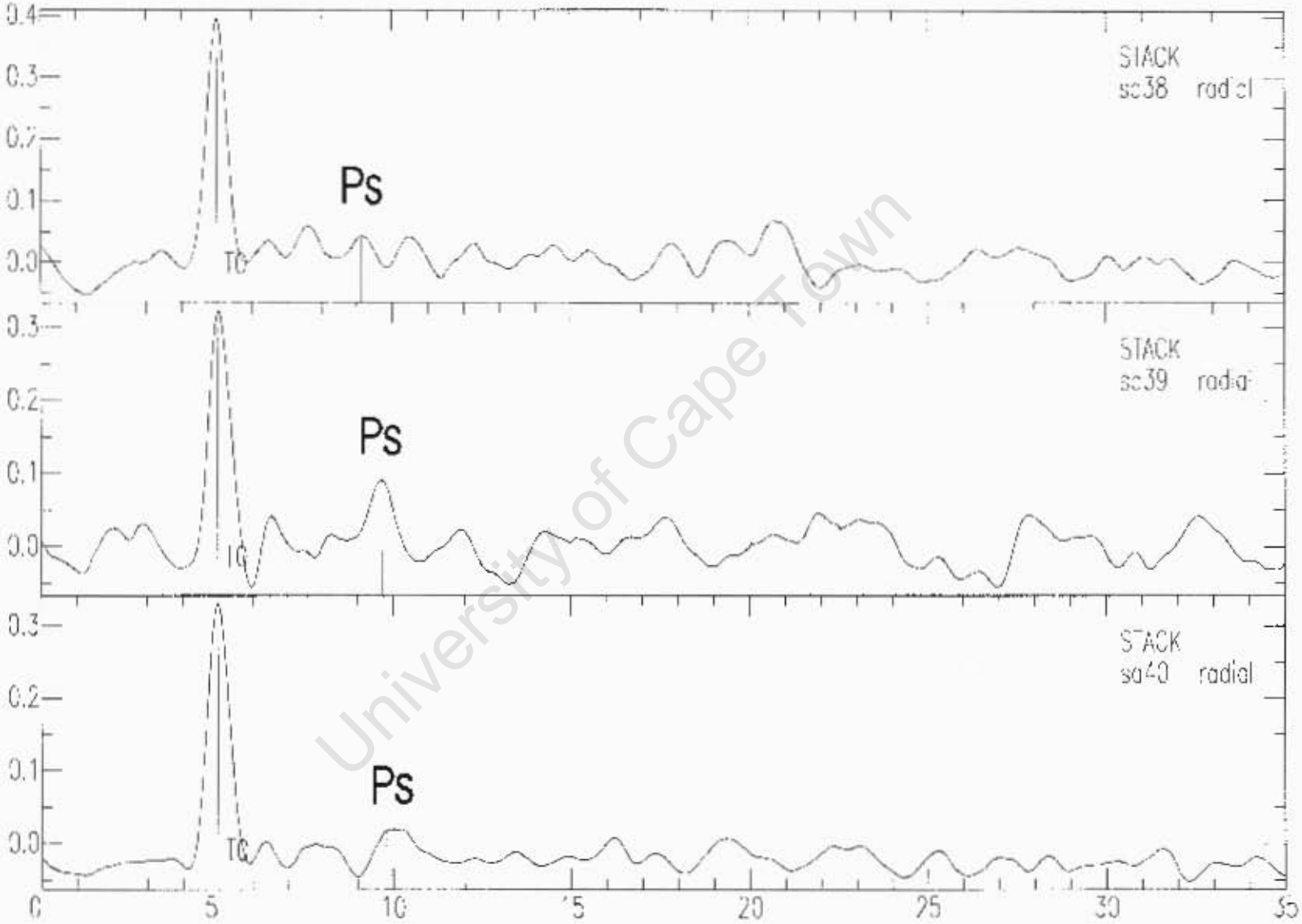

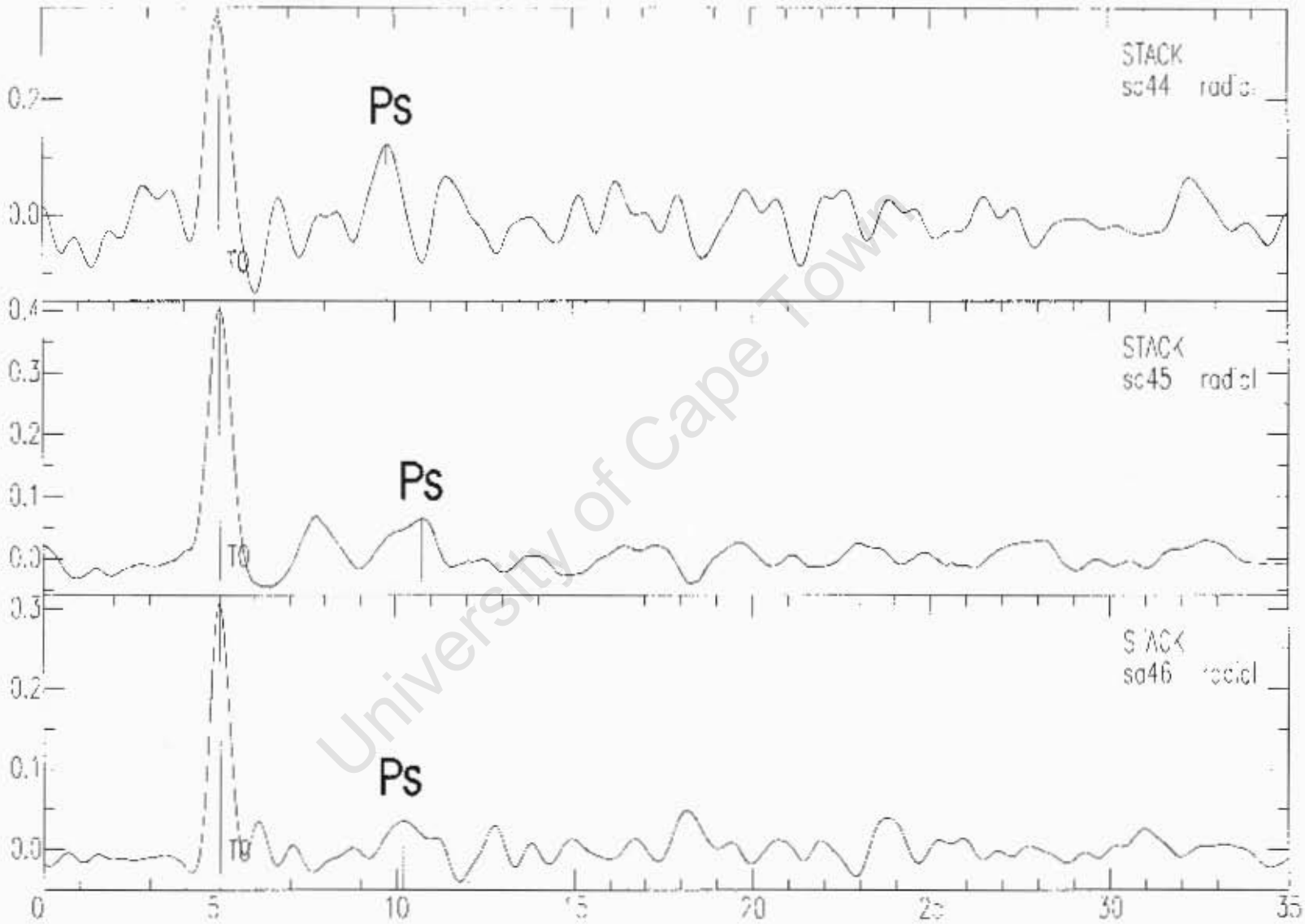

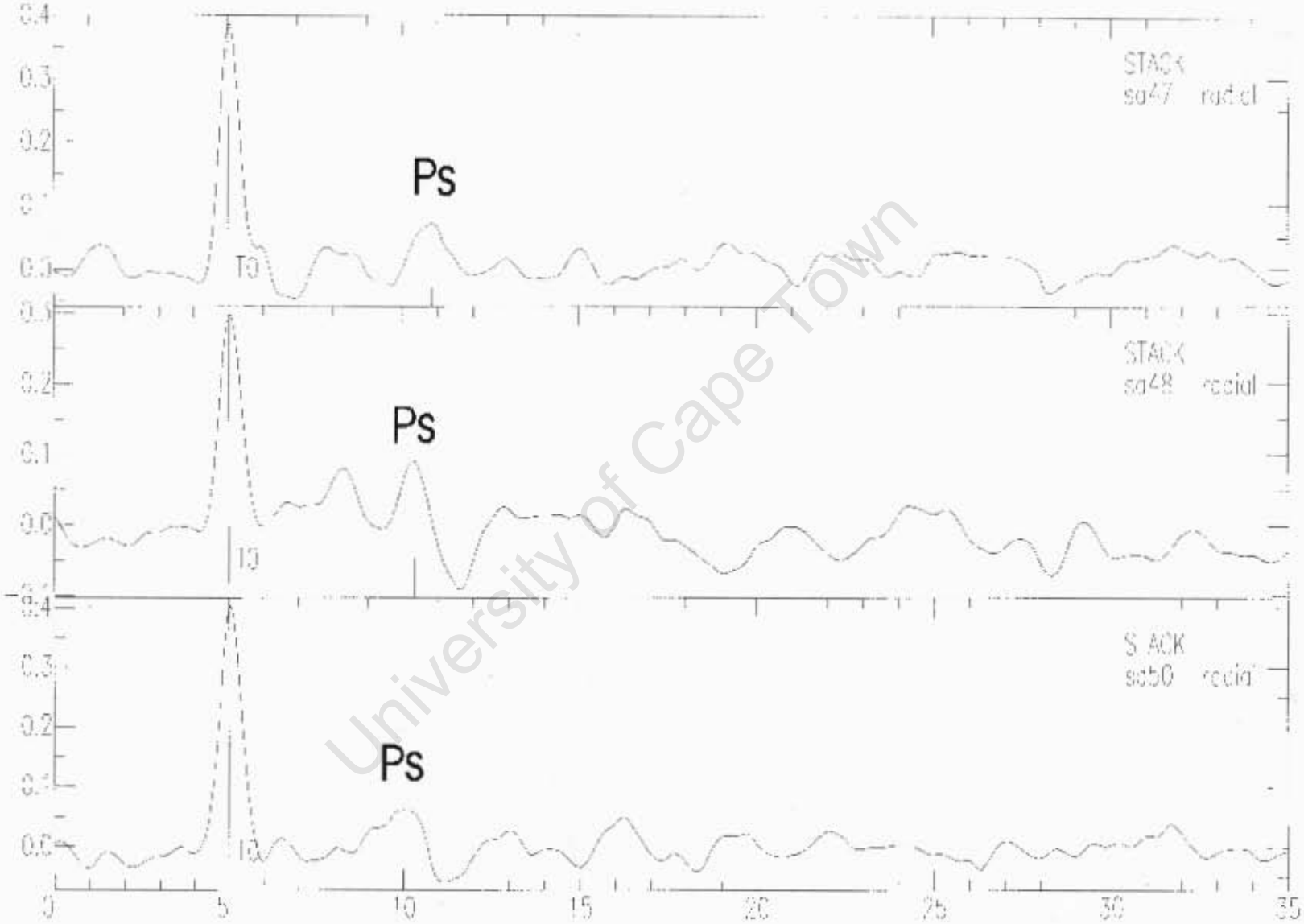

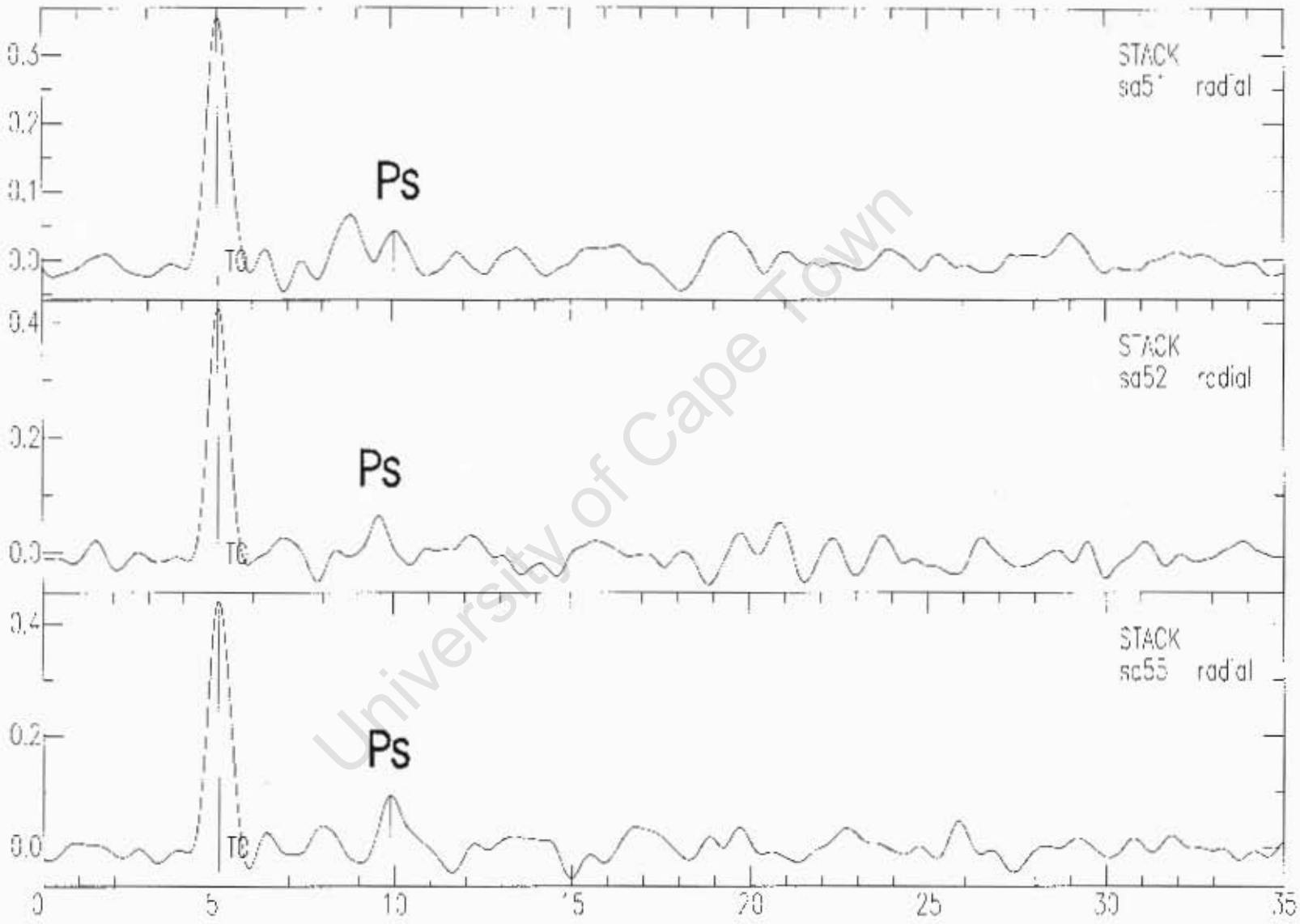

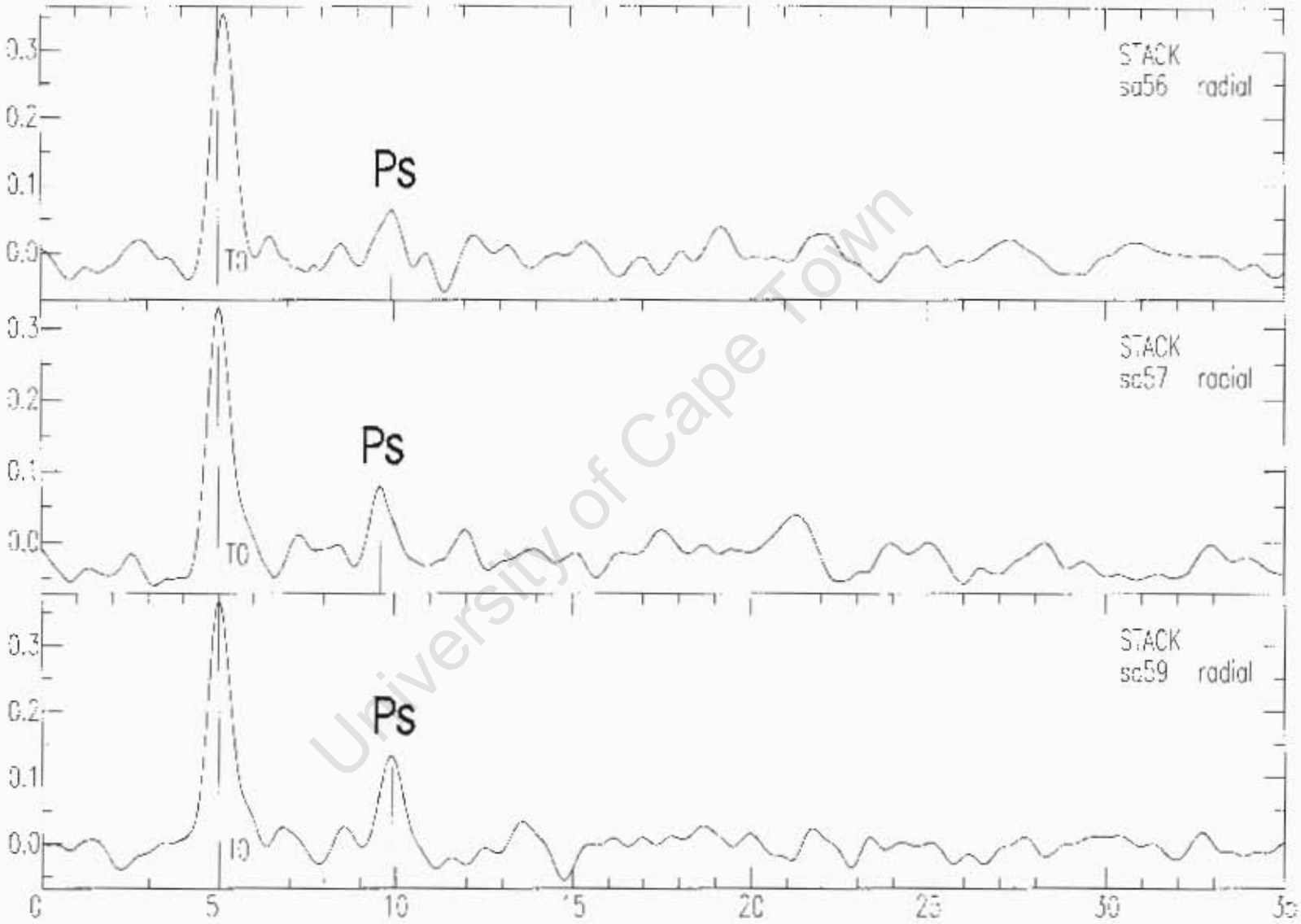

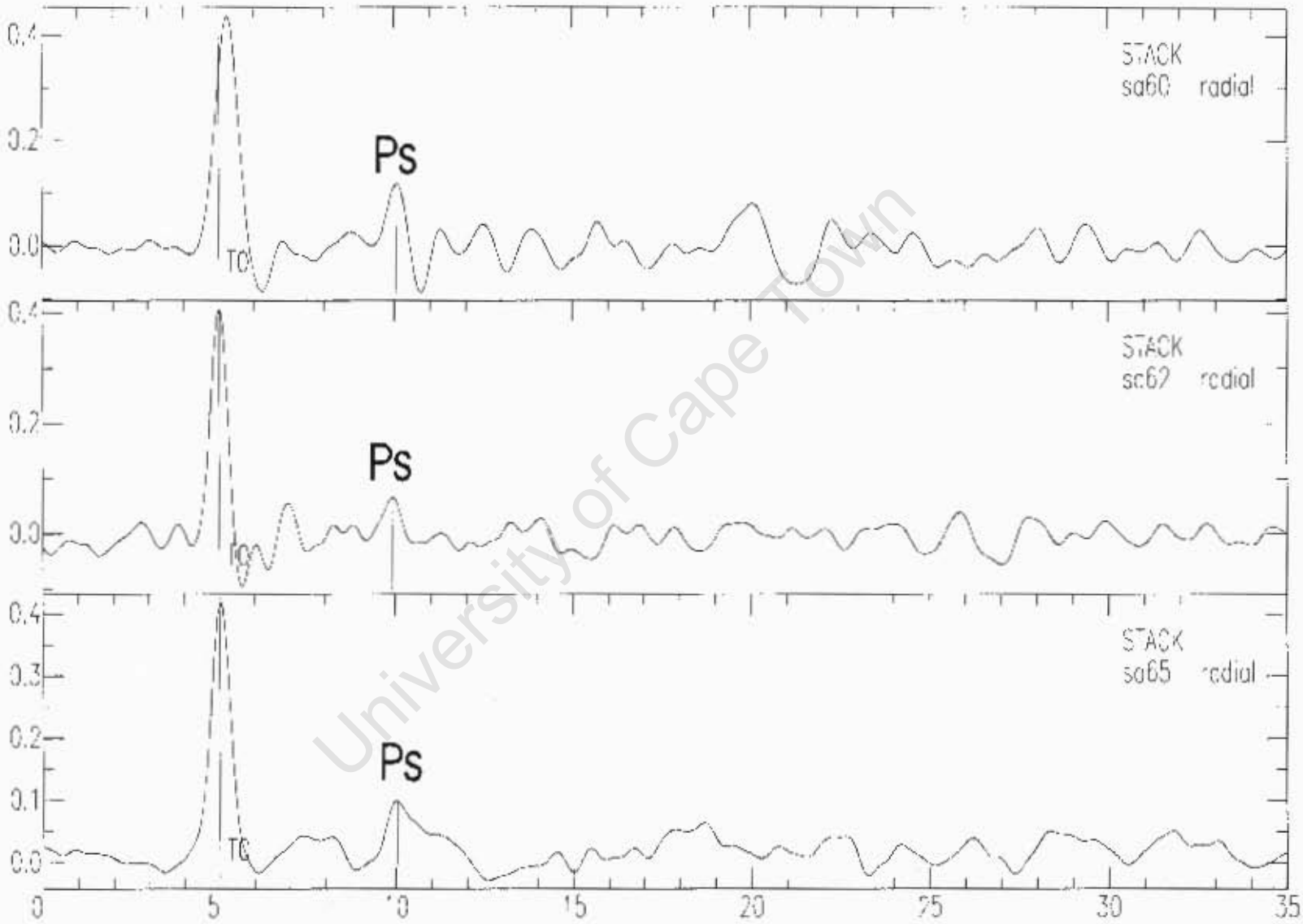

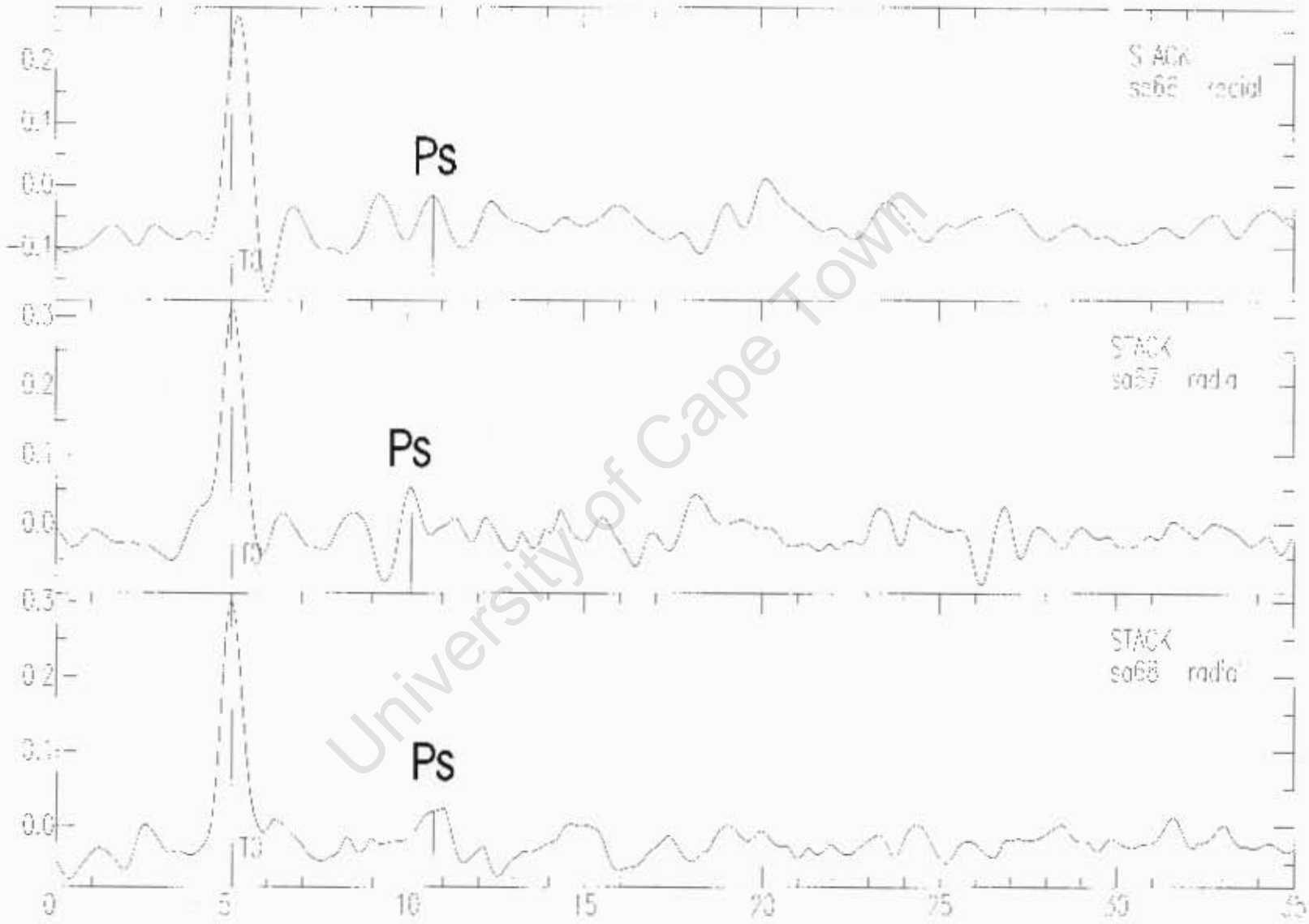

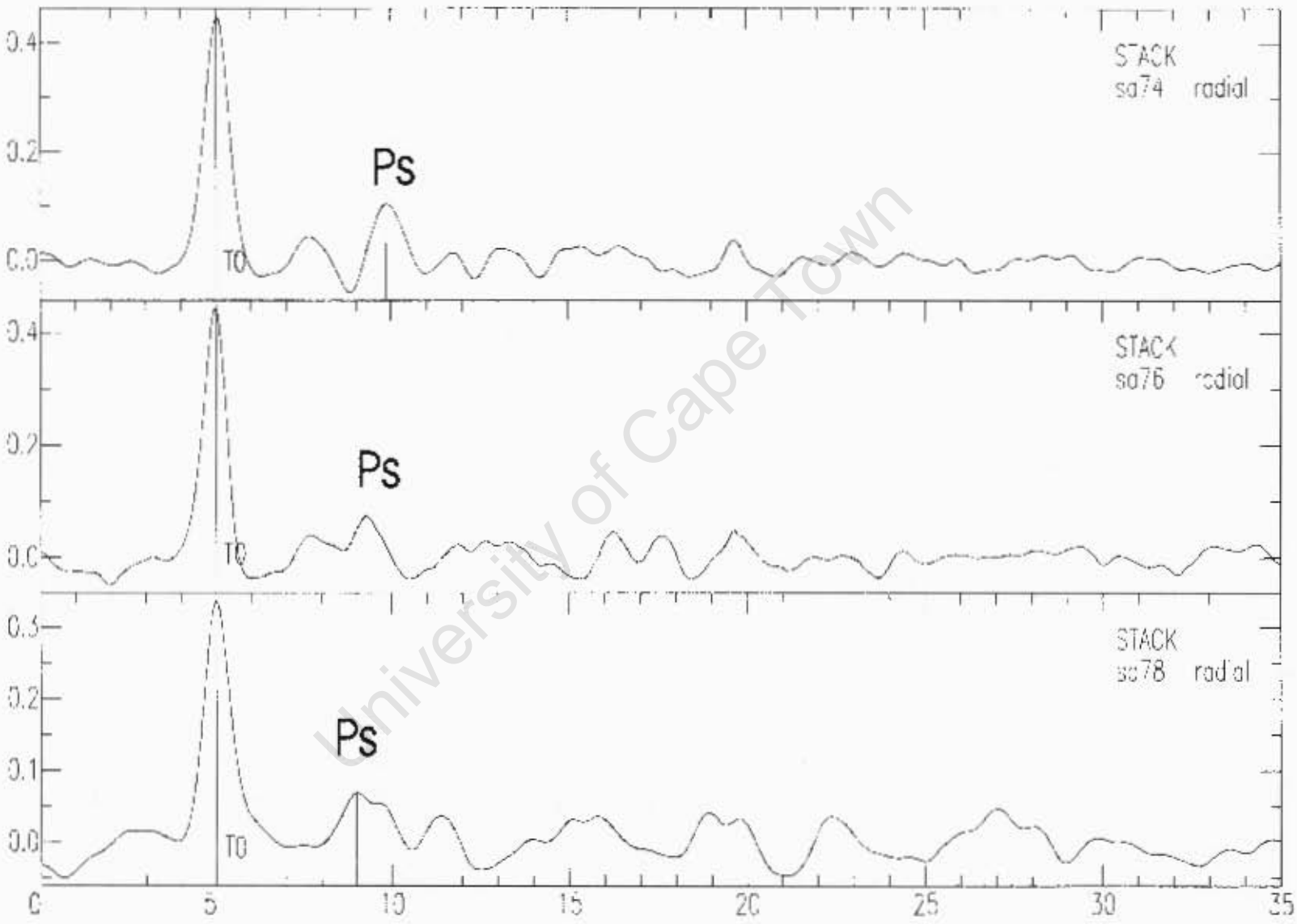

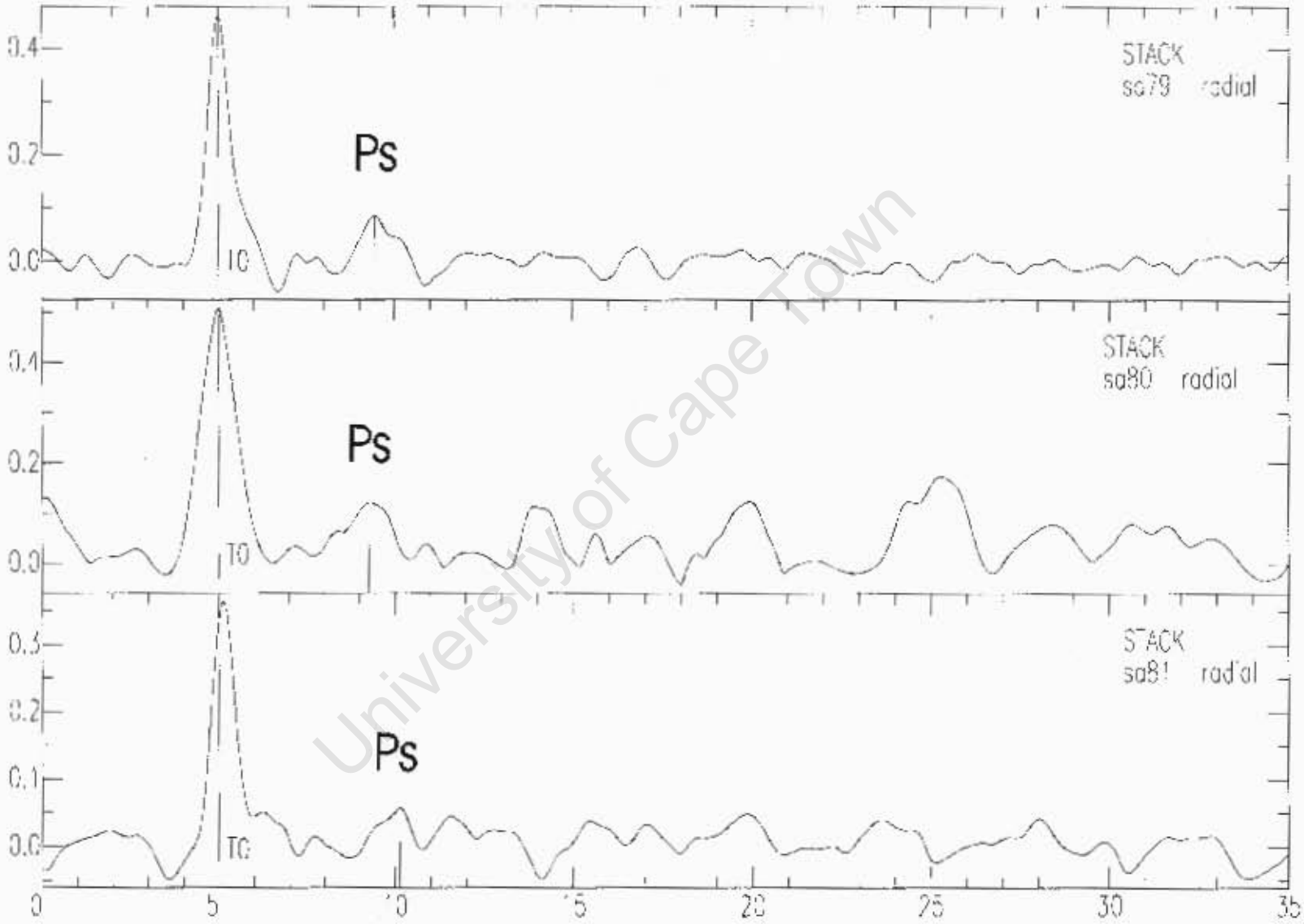

Appendix B

Stacks of receiver functions for individual stations used to study the upper mantle structure in Chapter 6.

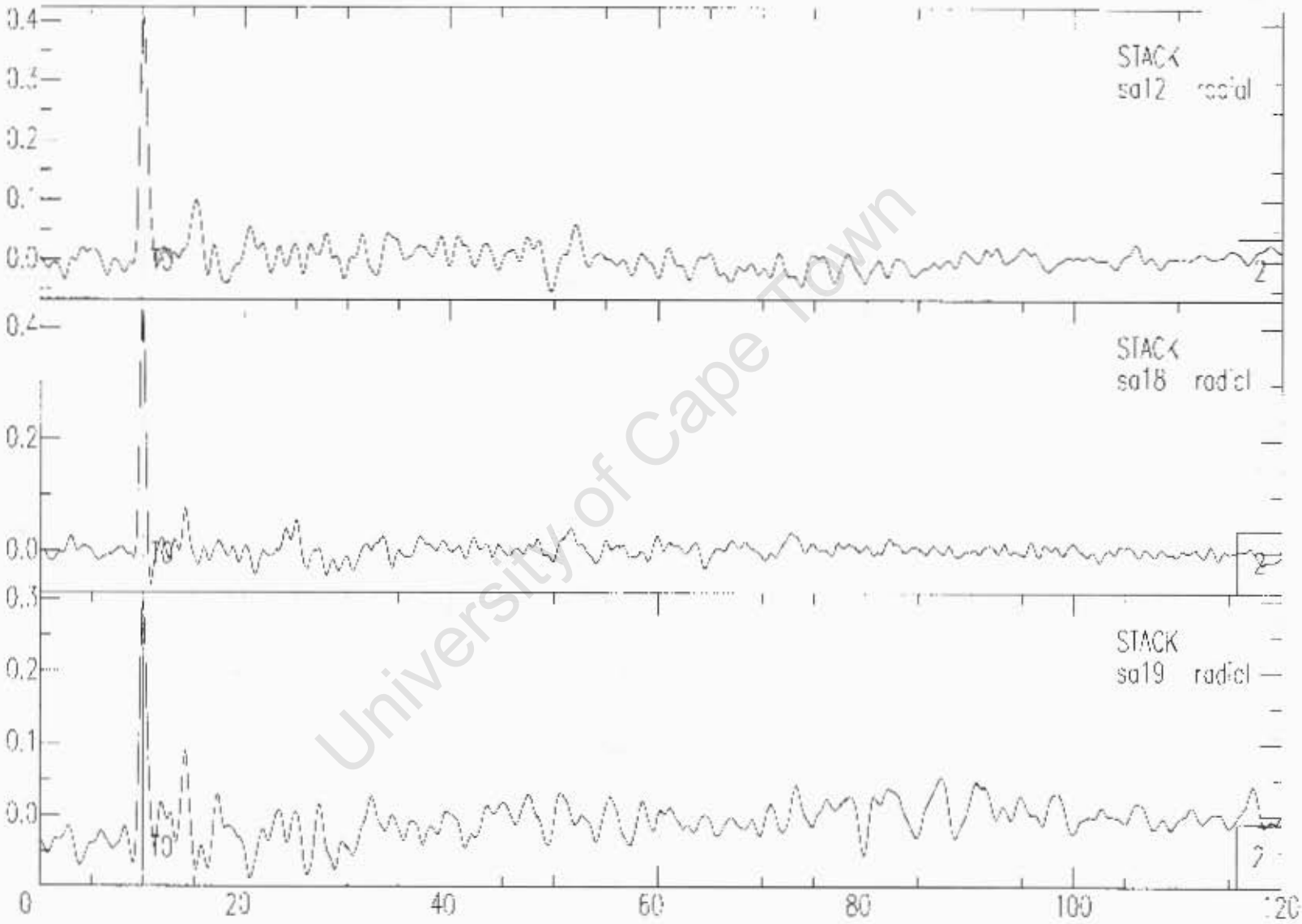

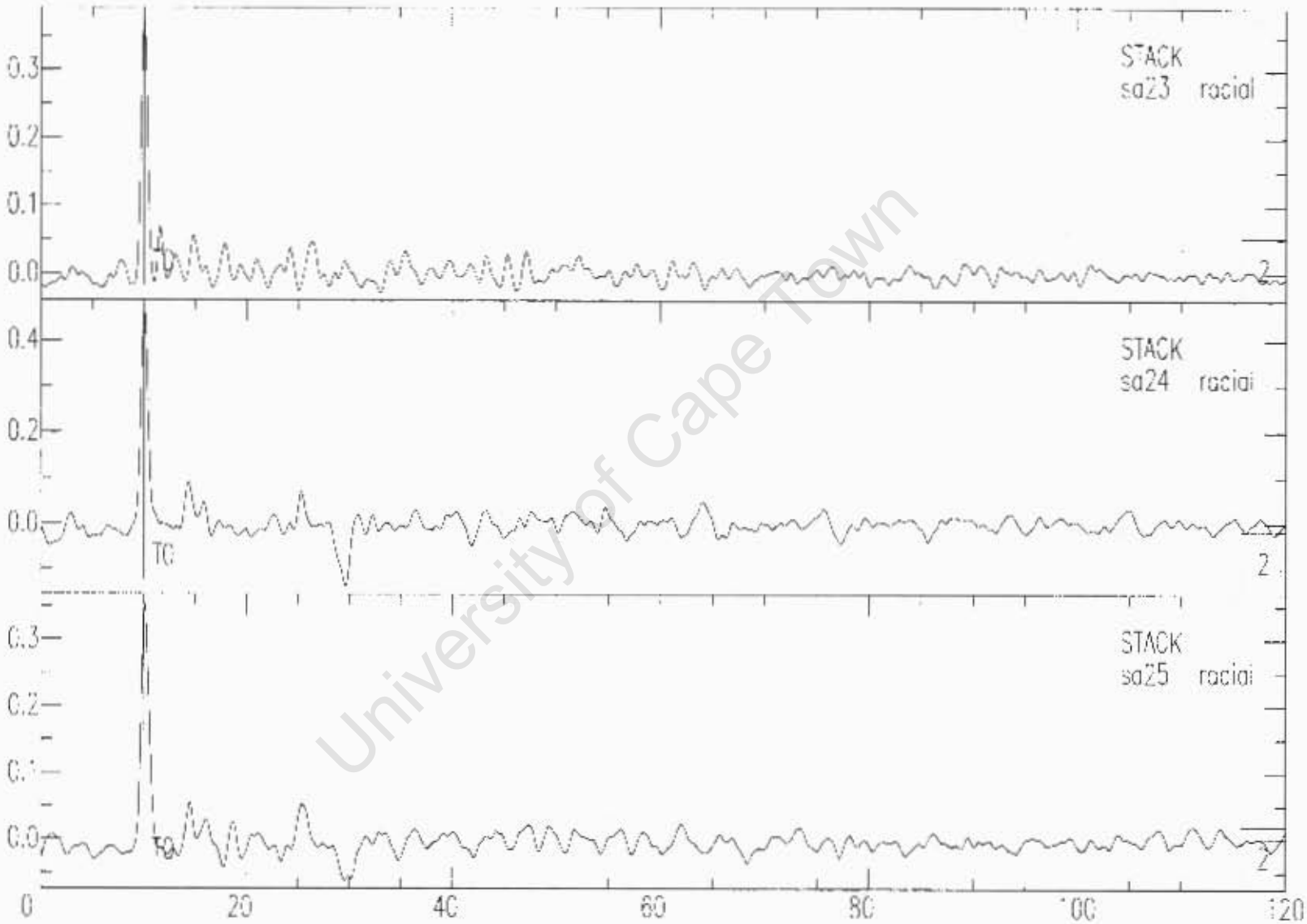

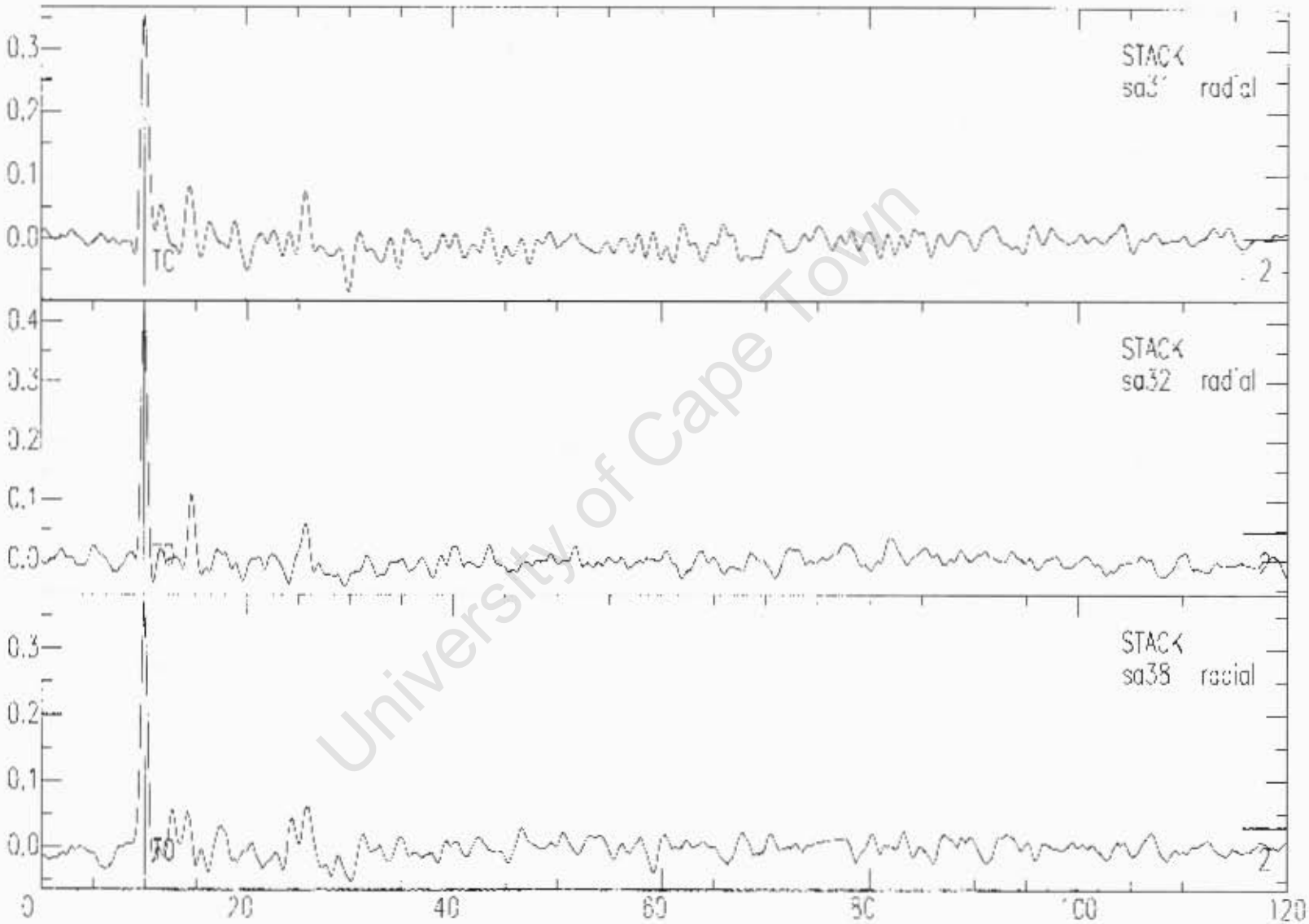

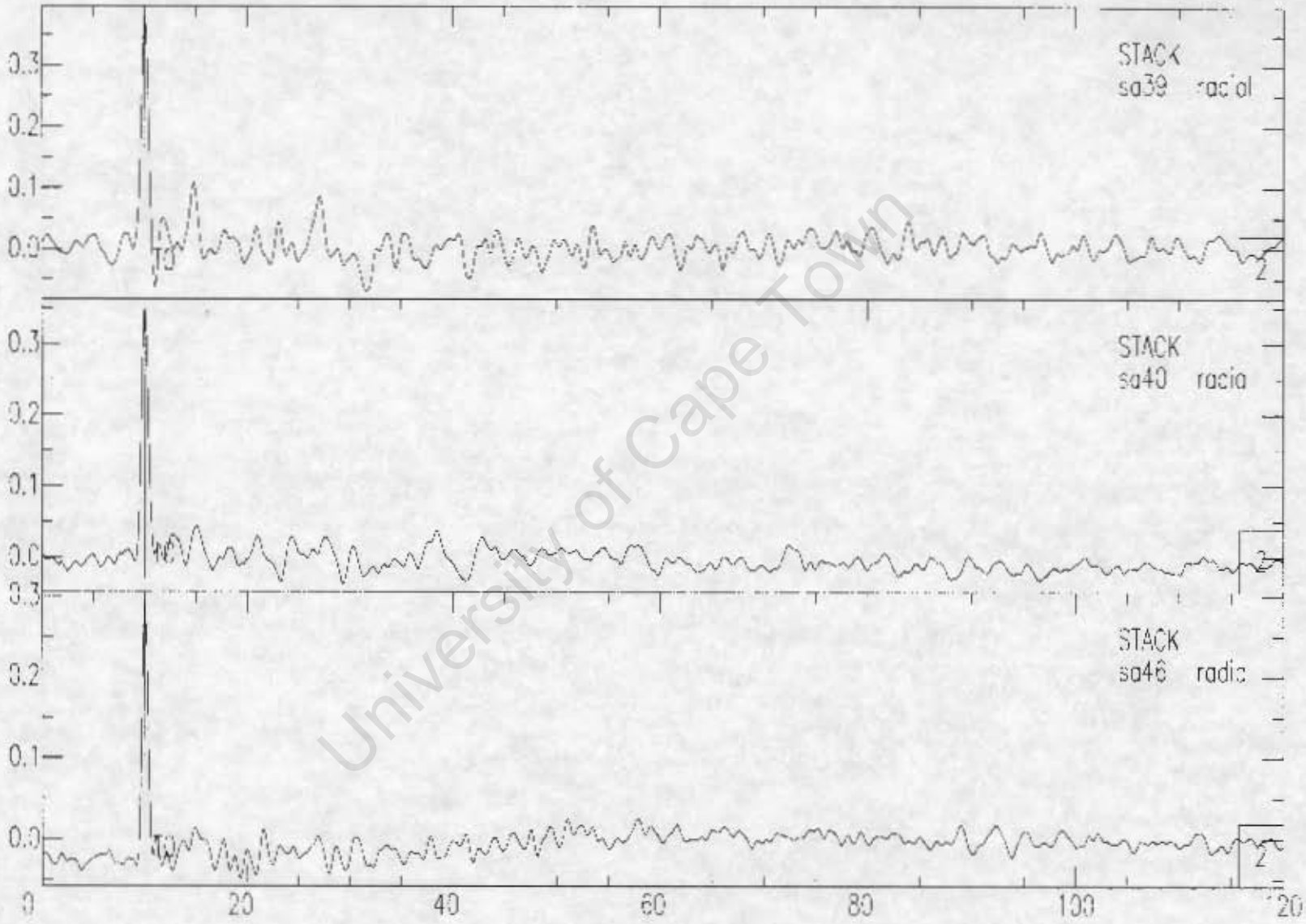

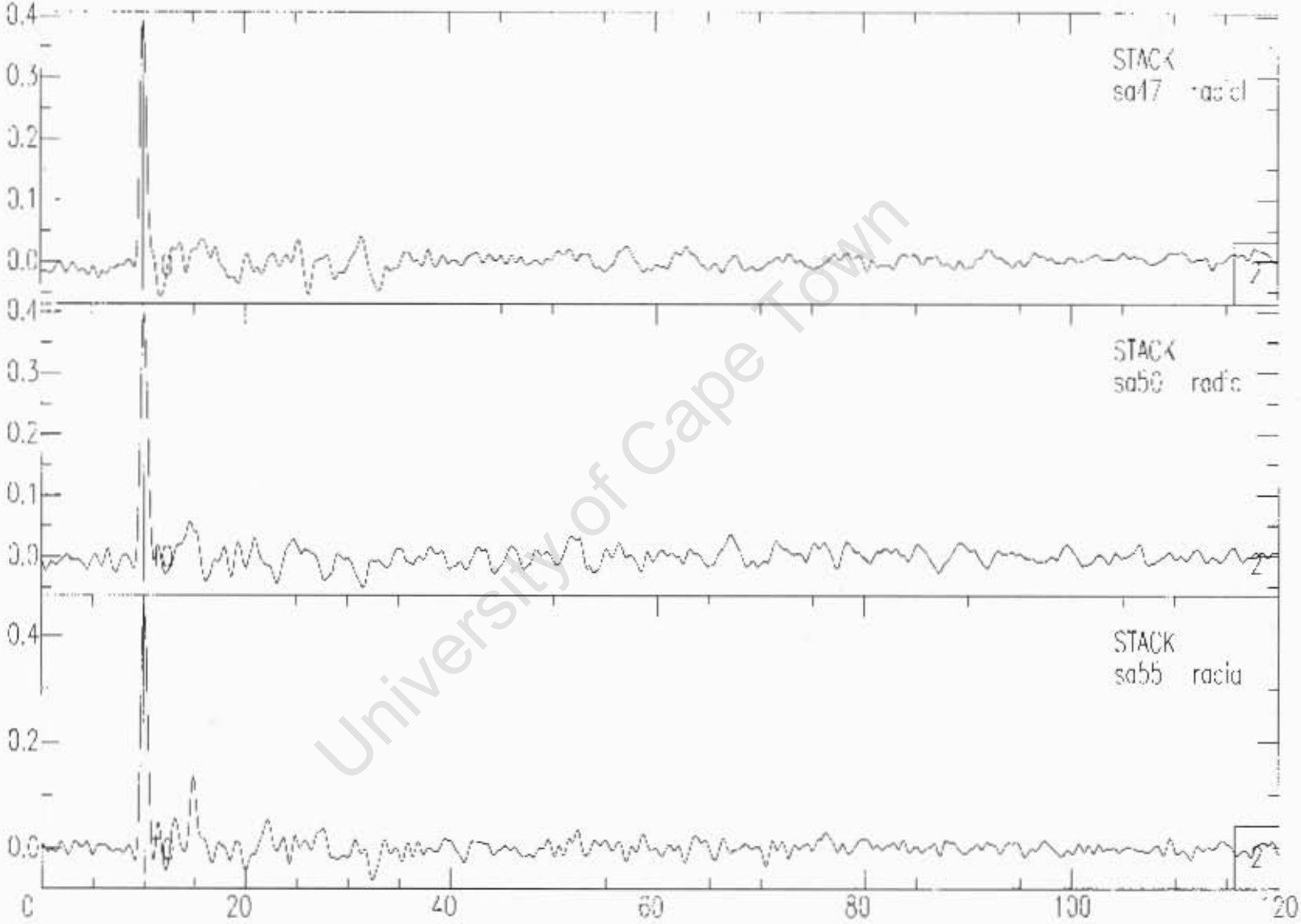

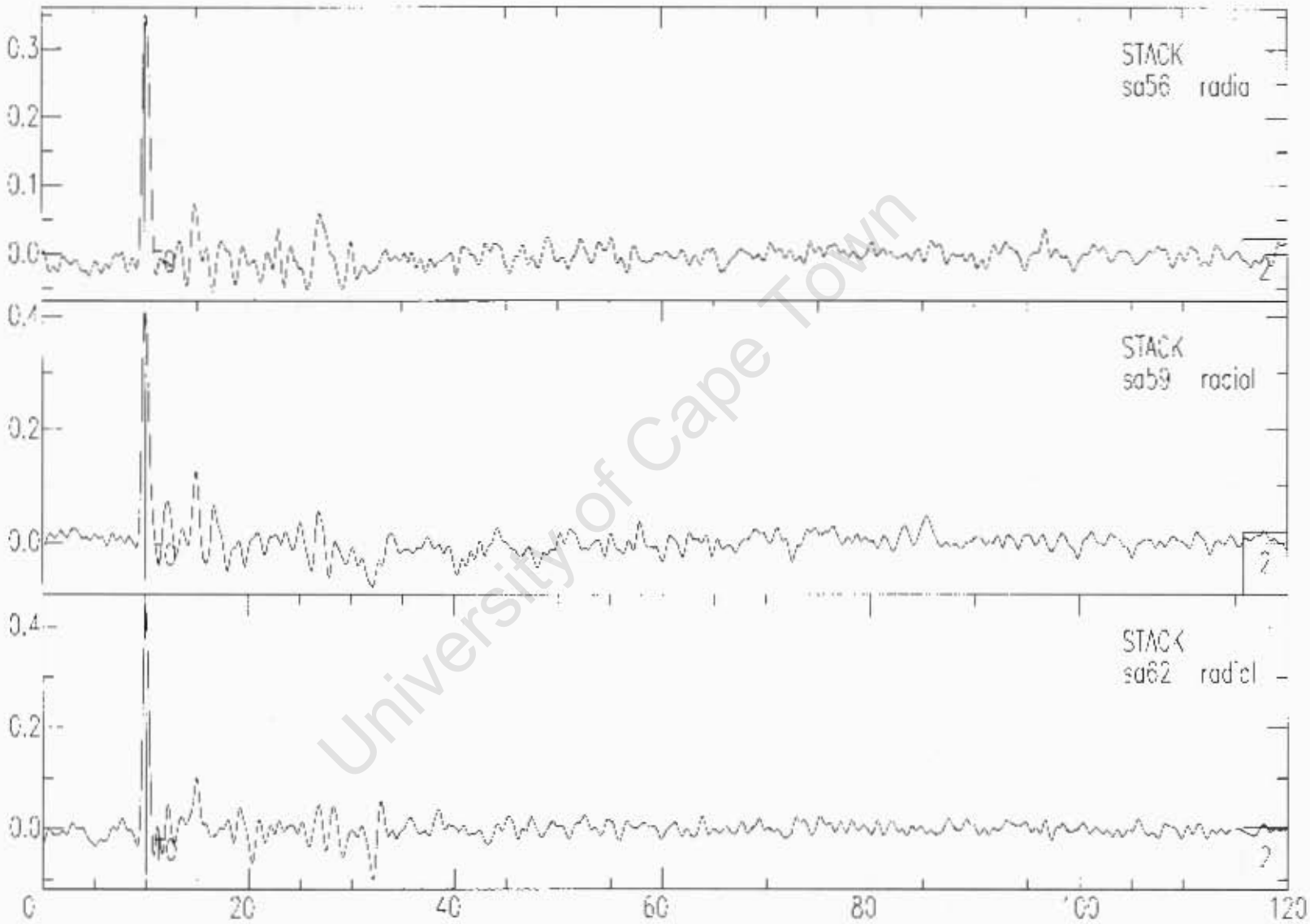

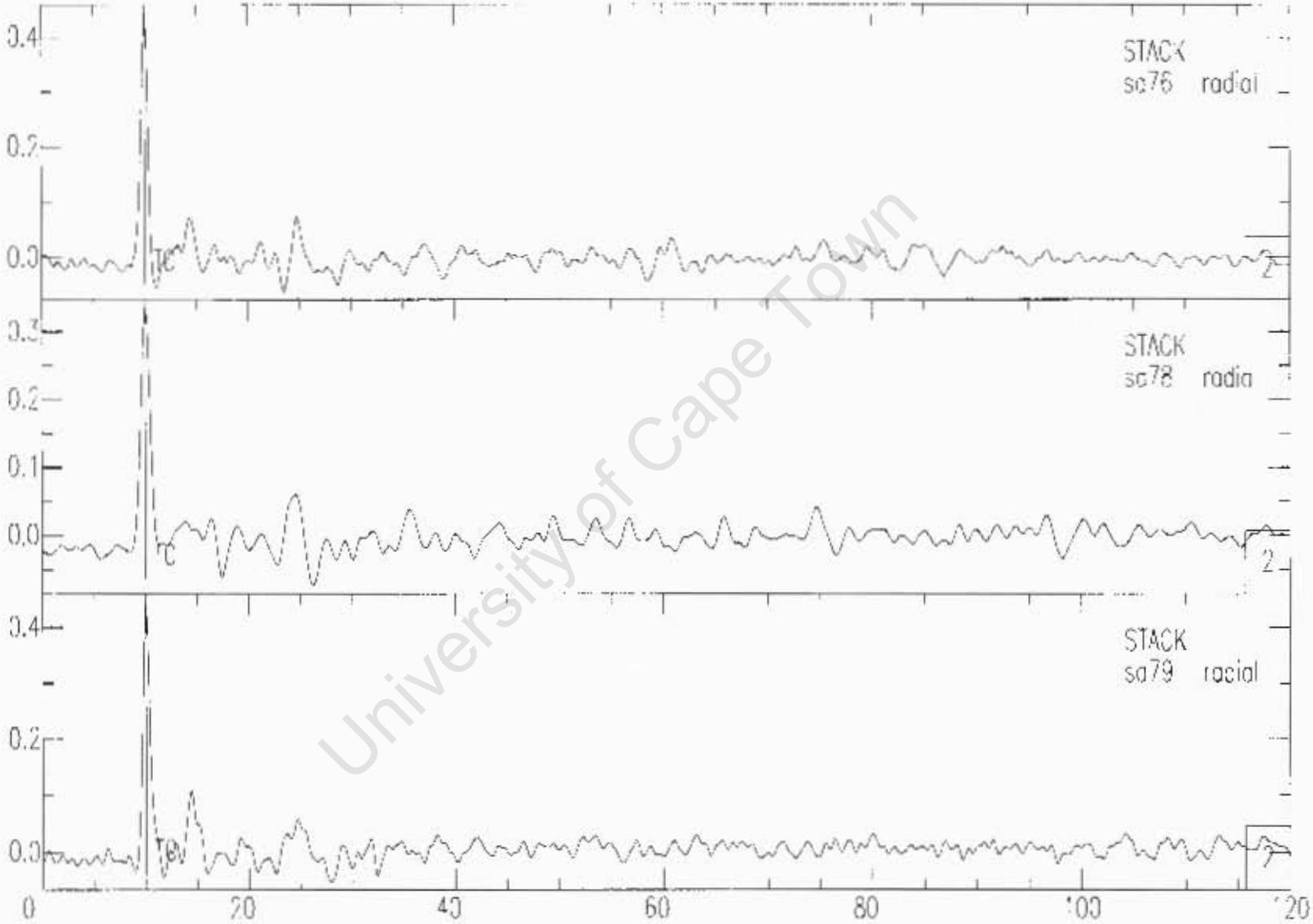

Appendix C

Descriptions of computer programs mentioned in the text.
Unless otherwise stated, programs written by Jacek Stankiewicz.

DEPTH

Used in section 6.1, this EXCEL program uses the arrival time of a converted phase to compute the depth it was produced at, using seismic velocities from the IASP91 model. The velocities given in Table 6.1 are programmed in the computer, and the depth of the phase concerned is computed as a function of two input parameters: the arrival time of the converted phase and the ray parameter of the incoming signal. This is done using the mathematics from section 4.8. The ray parameter is determined using the program TTIMS described below.

TTIMS

Used in section 7.1, as well as in the program DEPTH mentioned above, the UNIX script written by Sebastien Chevrot uses the location of a seismic event and the position of recording sites to compute expected travel times of different phases and their ray parameters. In this study the program is used to compute ray parameters of the Ps phases. It uses a UNIX wrapper TTIMES, written by Ray Buland.

SAC2AH

This SAC utility, used in section 7.2 converts seismic record files from SAC

to AH format. Given a SAC file and a filename as input parameters, the program will produce an AH file under the given name from the SAC file.

POISSON

Used in section 7.3.5, this Matlab program estimates the crustal thickness and the seismic velocities ratio using arrival times of Ps and Ppps phases from a given event. After reading in the seismogram, the program varies the values of the velocity ratio and the crustal thickness from 1.5 to 2.1 in steps of 0.01and from 20 to 60 km in steps of 0.5 km, respectively. For each pair of values it uses equation (7.4) and (7.5) to calculate expected times of arrival for the Ps and Ppps phases, and checks the amplitudes at these values, adding the two together. The resulting graph shows the values obtained for each ordered pair input, where cold colours represent low amplitudes, and warm colours high amplitudes that correspond to the true peaks in the seismogram, and therefore the real values of velocity ratio and crustal thickness.

RESPONSE

Used in section 8.2, this Matlab program is used to calculate the response of a given array. It reads in the coordinates of recording sites with respect to the centre of the array, and using equation (8.6) computes the response. In this study the wave numbers in the NS and EW directions were varied from –0.5 to 0.5 in steps of 0.01 for each axis. The output is a 101 by 101 matrix, where each value in it corresponds to the response for a specific wave number vector. Cold colours represent low response, while warm ones occur in areas of high response, or anomalies.

BEAM

Used in section 8.5, this Matlab program is used to perform plane wave beamforming calculation. It reads in the station coordinates and the seismic records of each station, and uses the equation (8.10) to do the calculation. Slowness is varied from -0.5 to 0.5 in steps of 0.01, and the result is a matrix similar to the one from RESPONSE, where each value corresponds to the result for a specific slowness vector.

Appendix D

Results of the f-k analysis for the 0.05-0.1 Hz frequency band.

Attached figures are graphic representations of matrices computed by program BEAM (described in Appendix C), containing values of the beamforming function $B(\theta_s)$ for different wave numbers **k**.

Cold colours correspond to low values of B, while warm ones imply a high value of B, and therefore correlation to the true angle of incidence of the incoming wave.

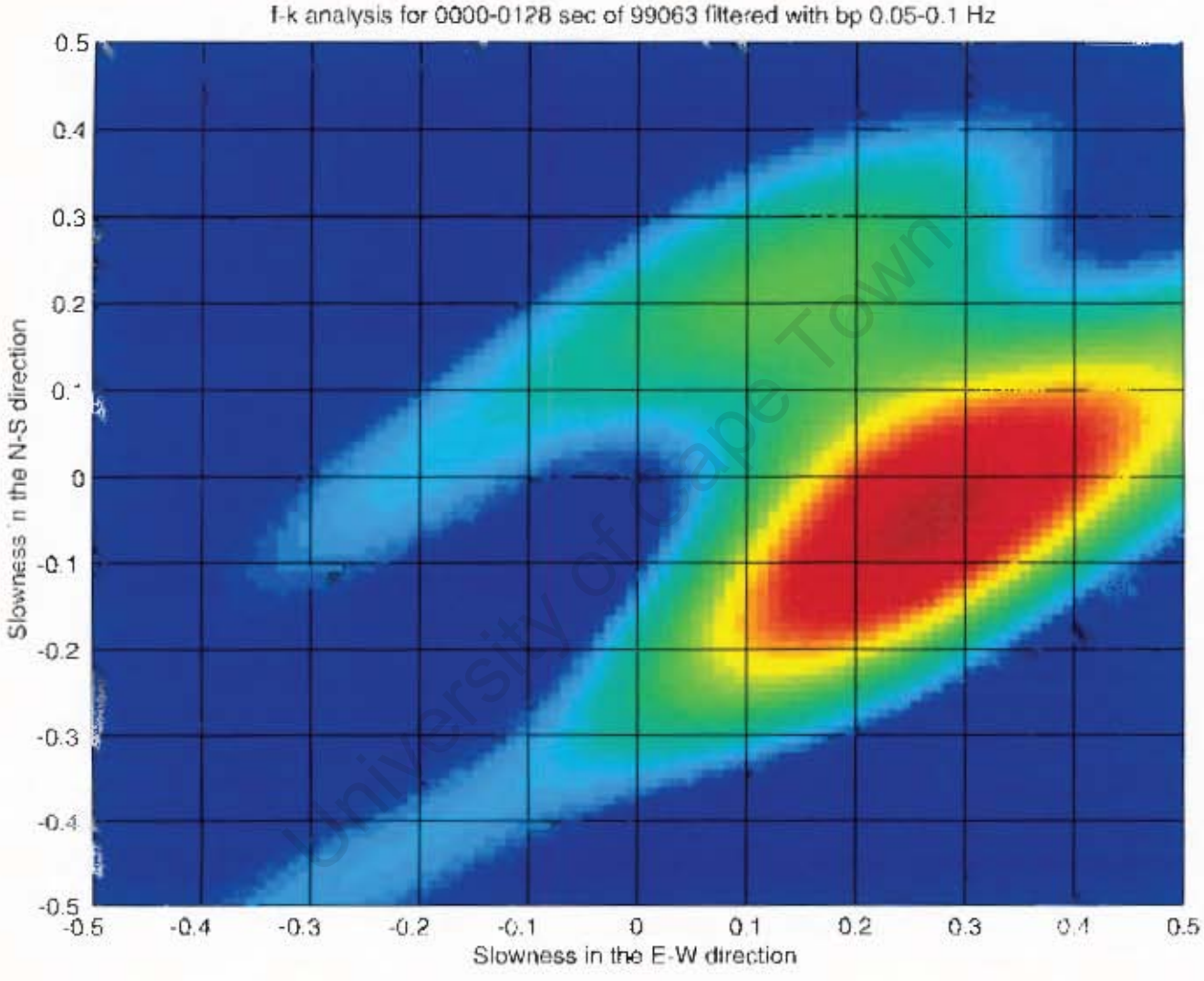

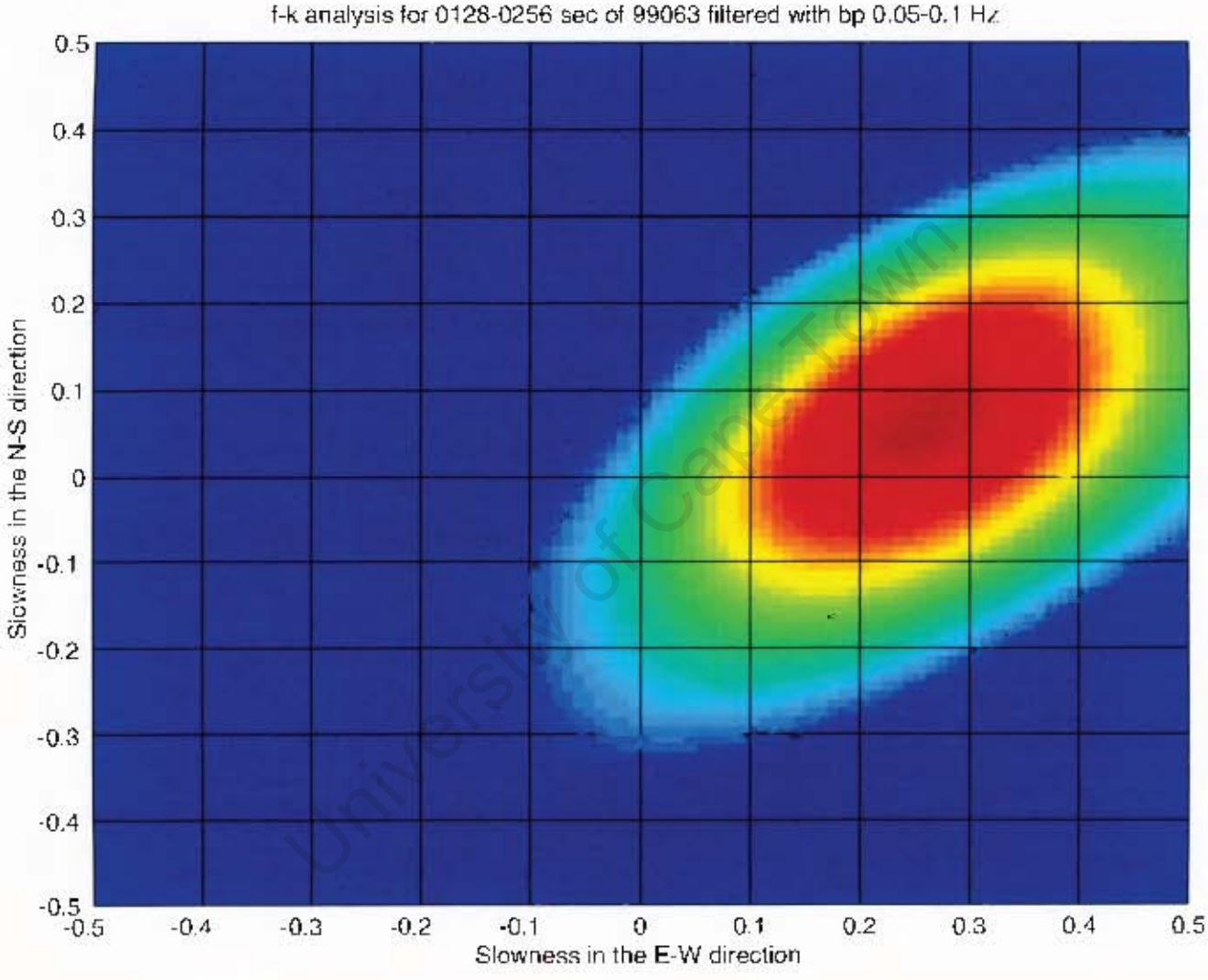

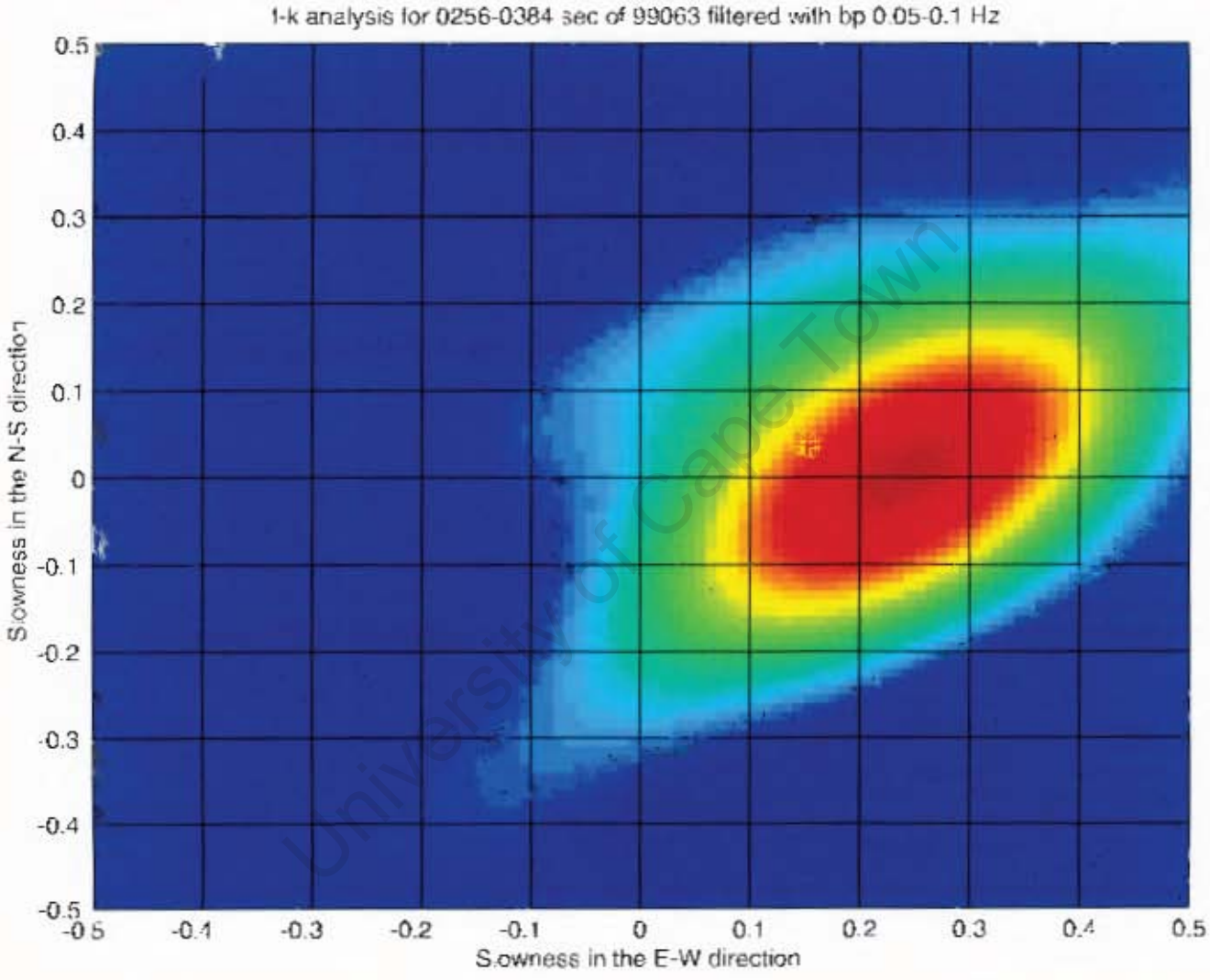

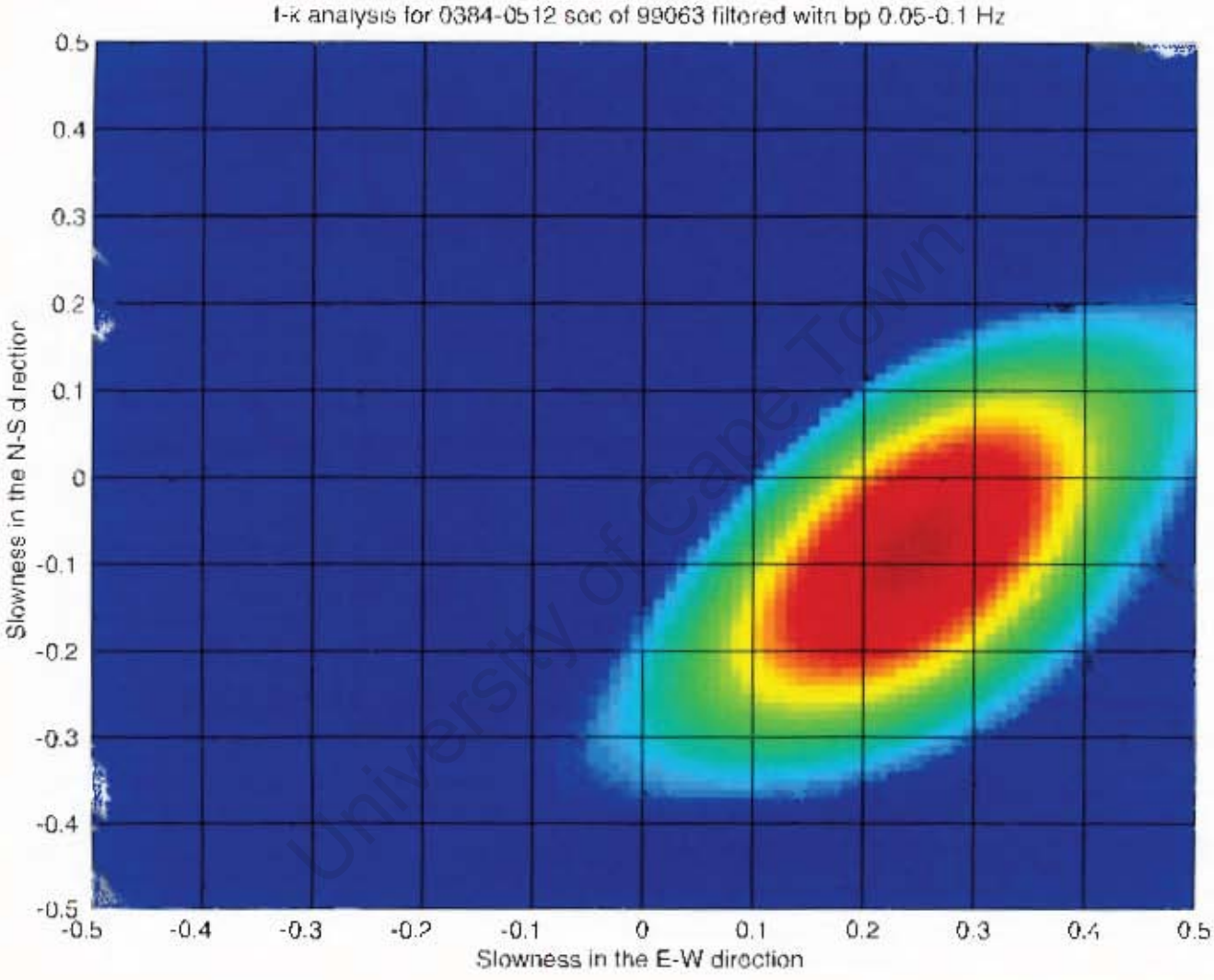

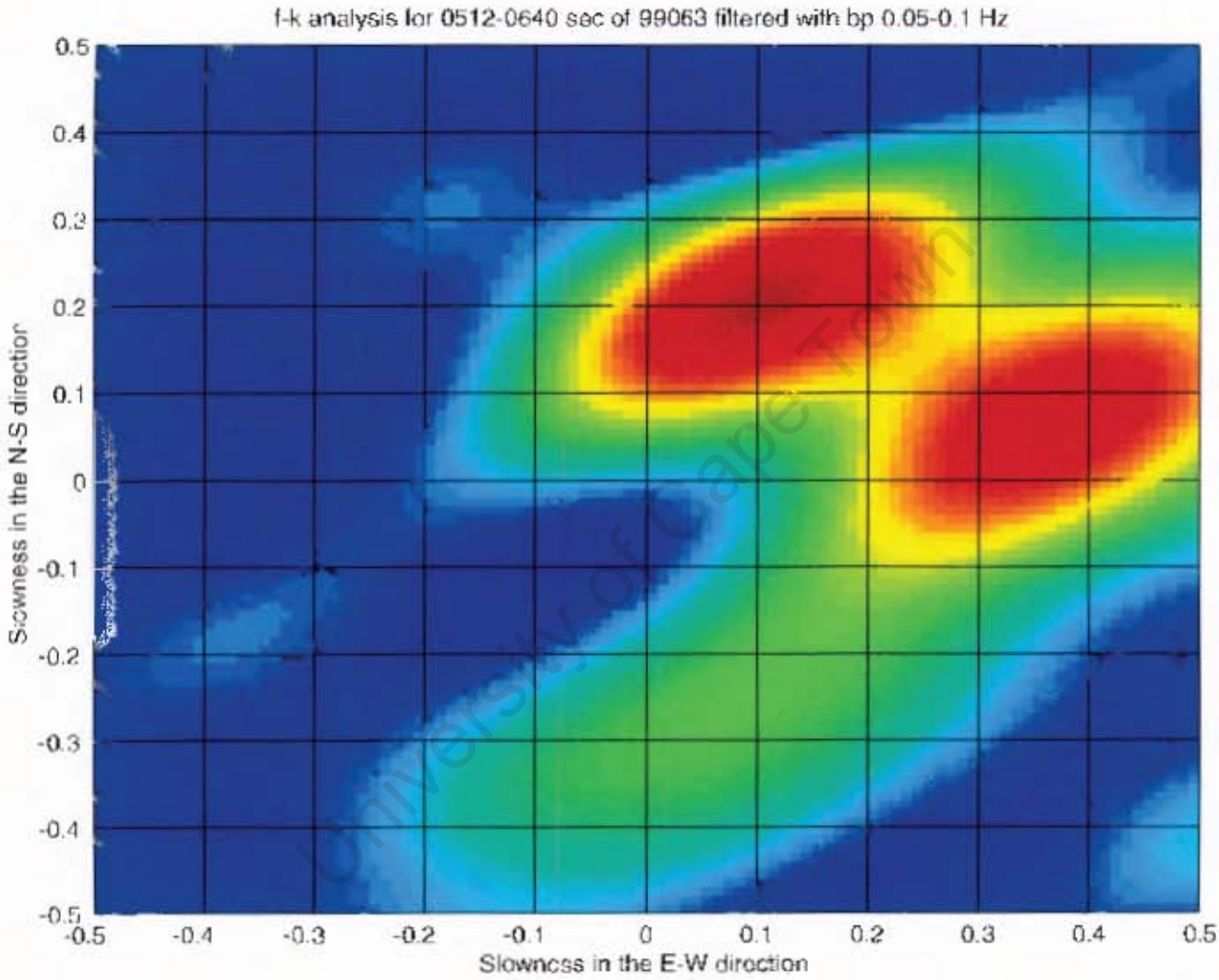

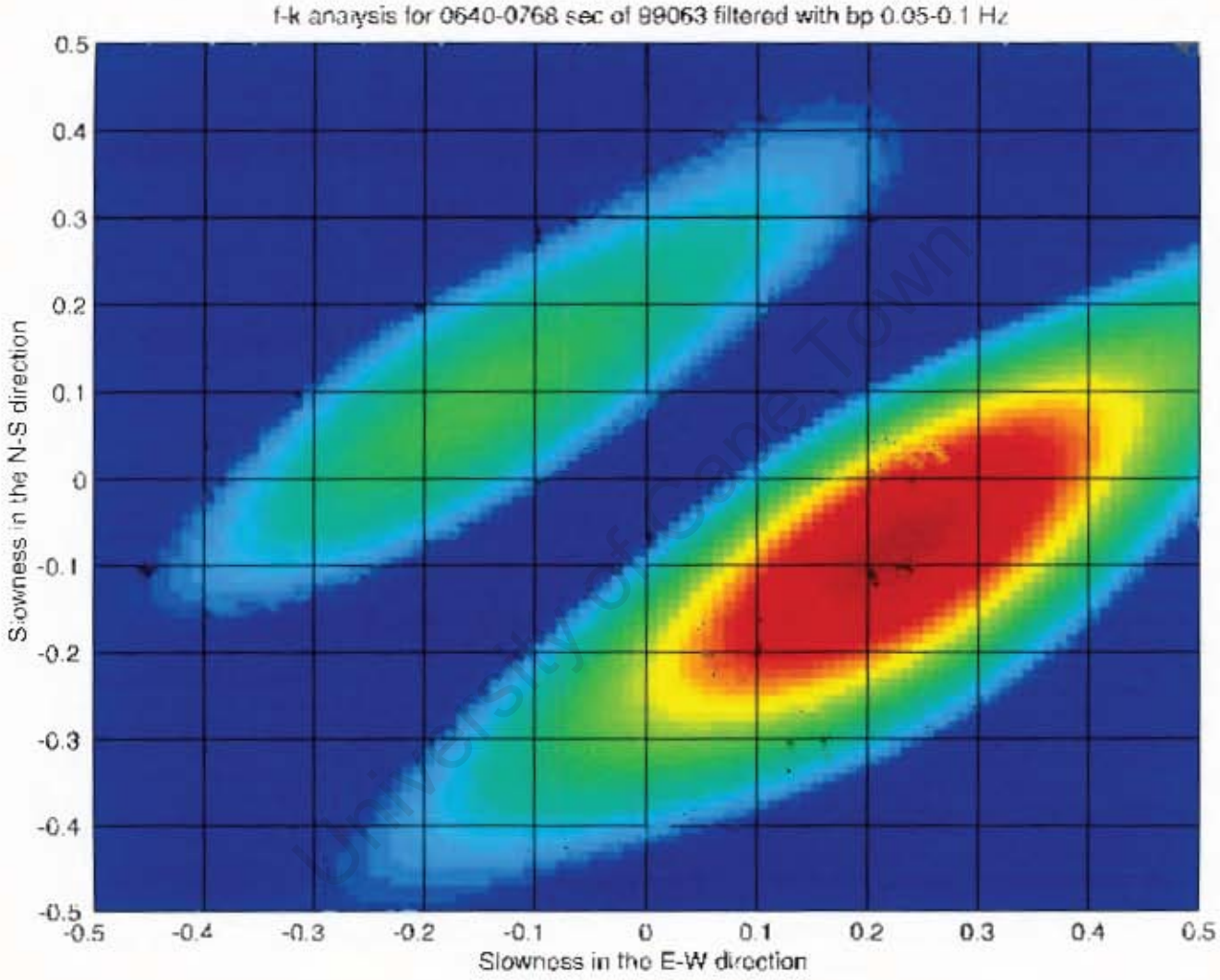

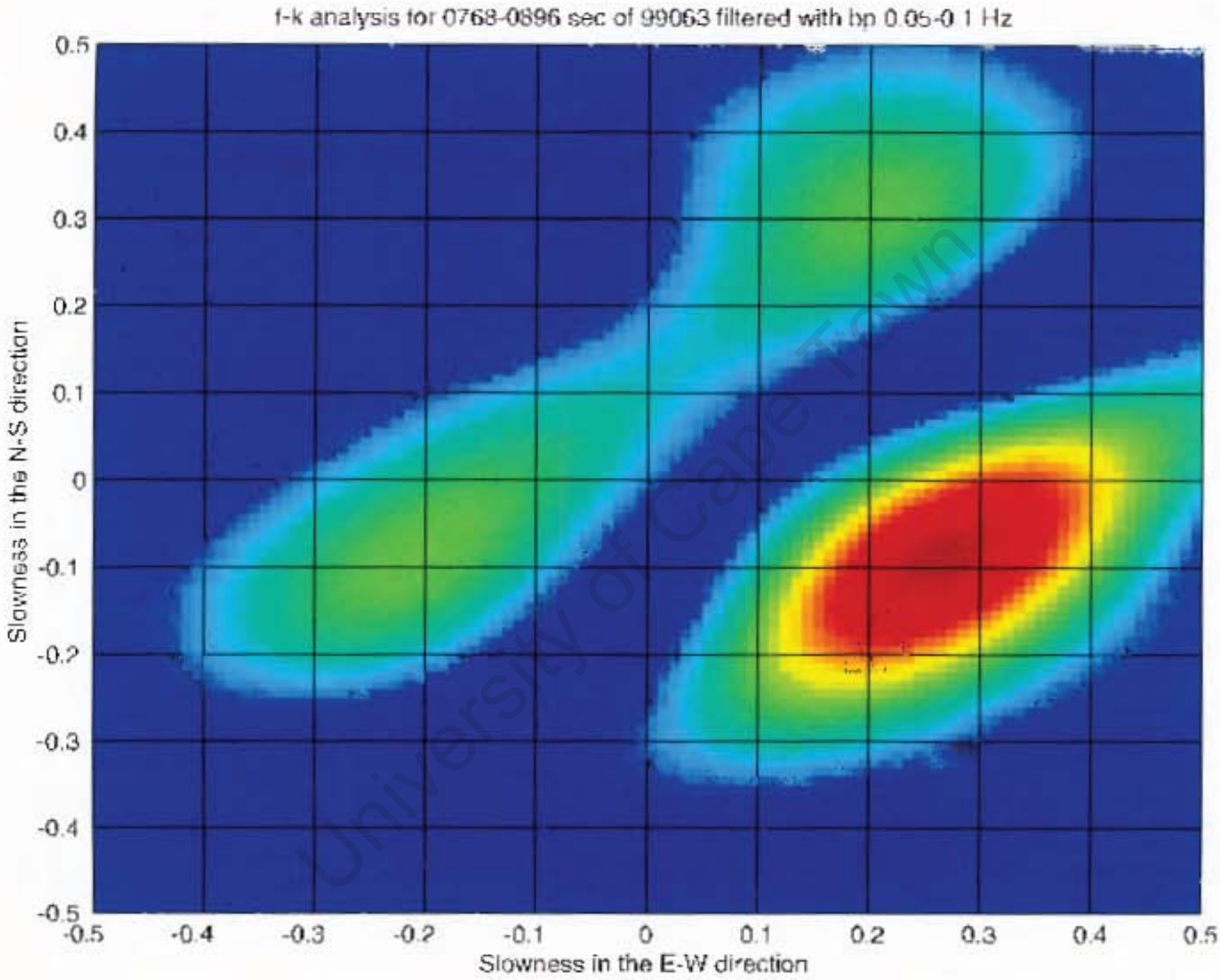

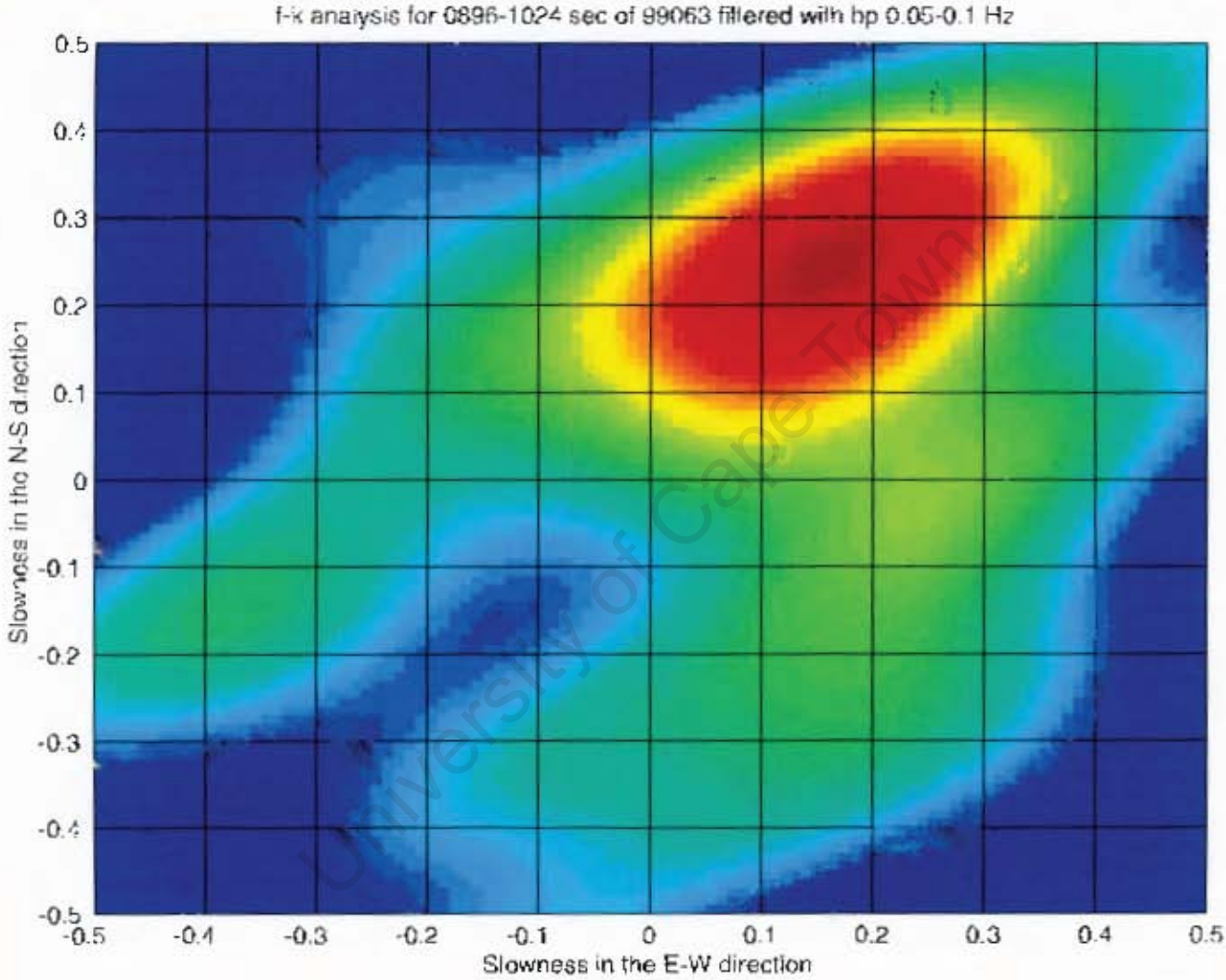

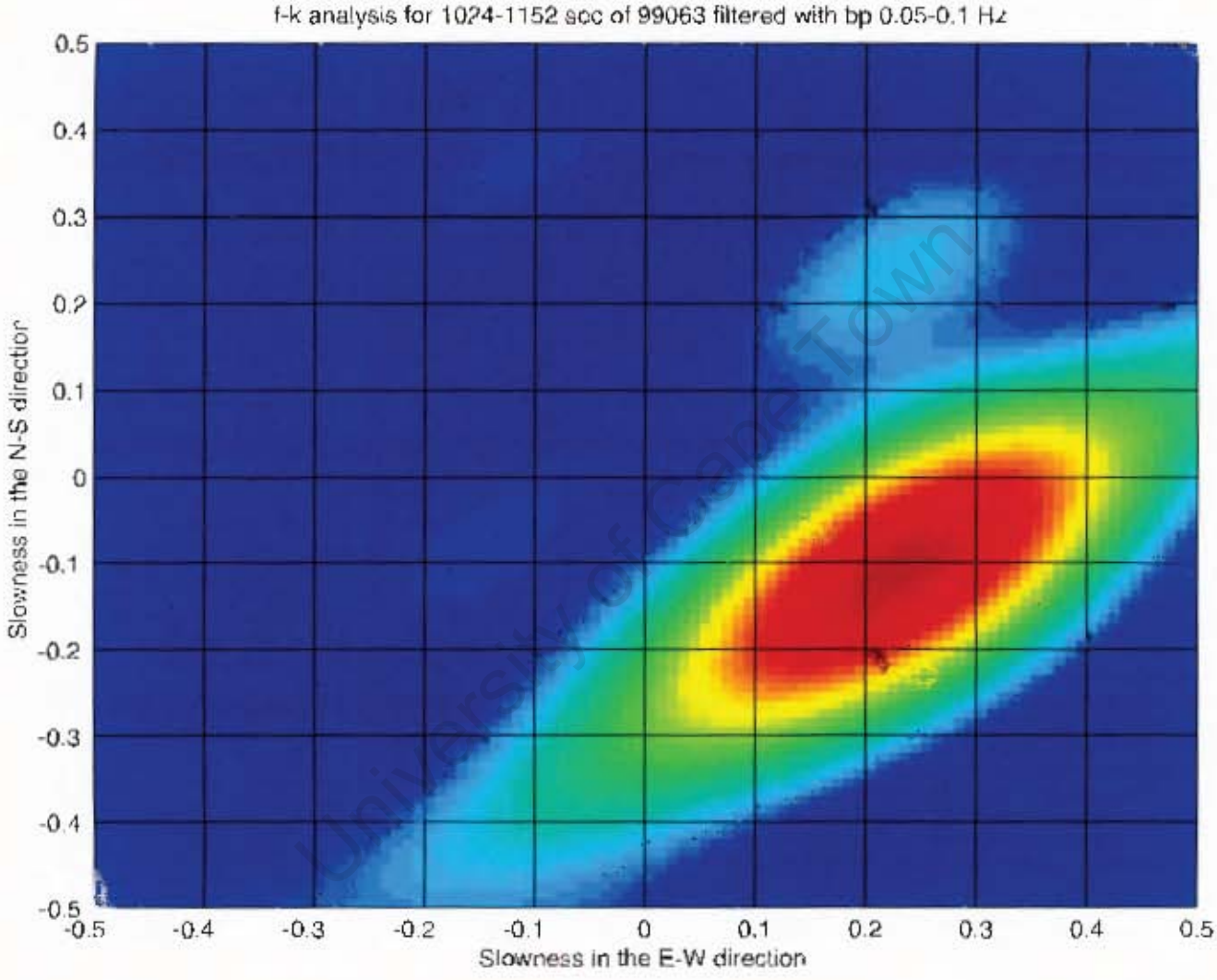

Appendix E

Results of the f-k analysis for the 0.1-0.3 Hz frequency band.

Attached figures are graphic representations of matrices computed by program BEAM (described in Appendix C), containing values of the beamforming function $B(\theta_s)$ for different wave numbers **k**.

Cold colours correspond to low values of B, while warm ones imply a high value of B, and therefore correlation to the true angle of incidence of the incoming wave.

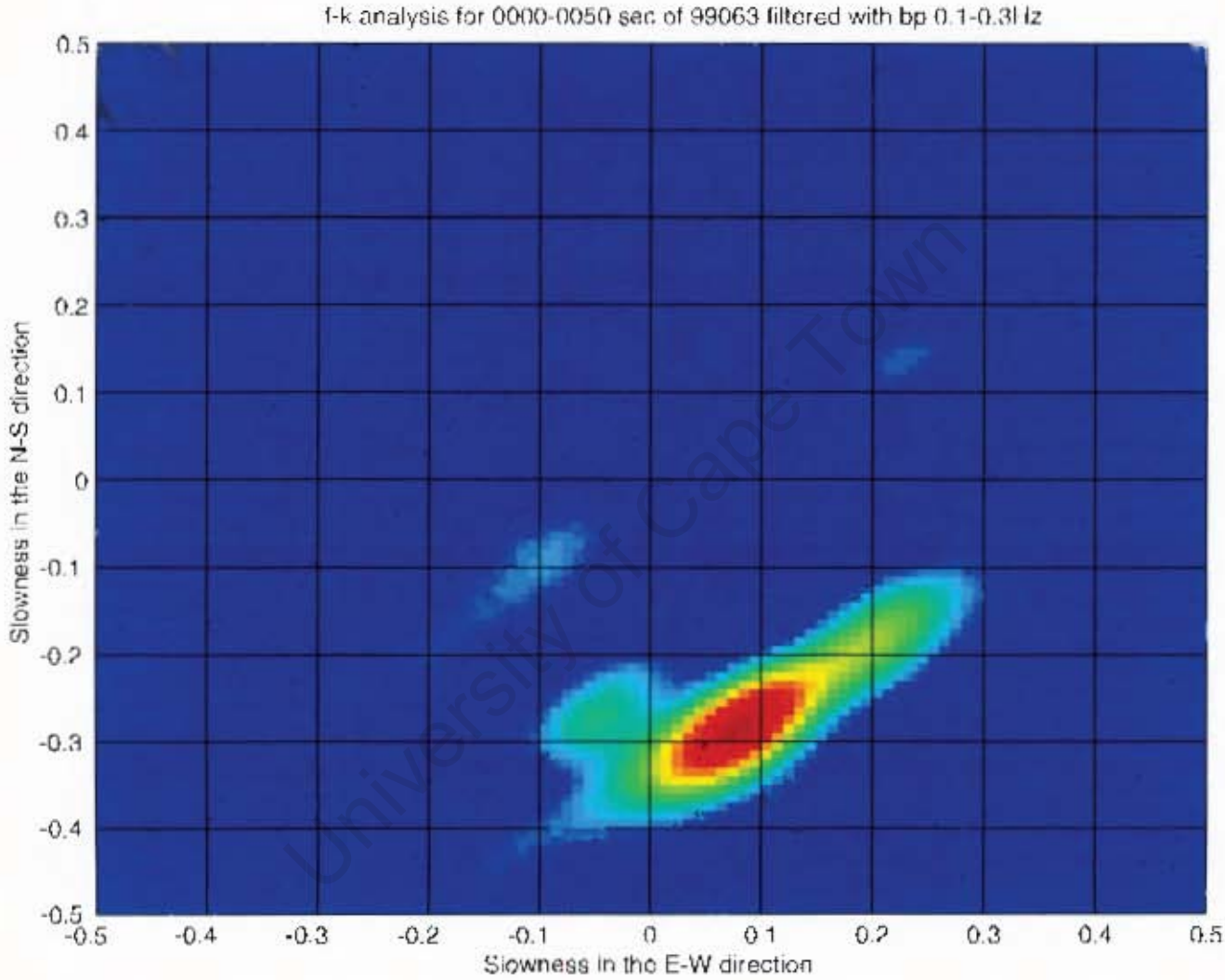

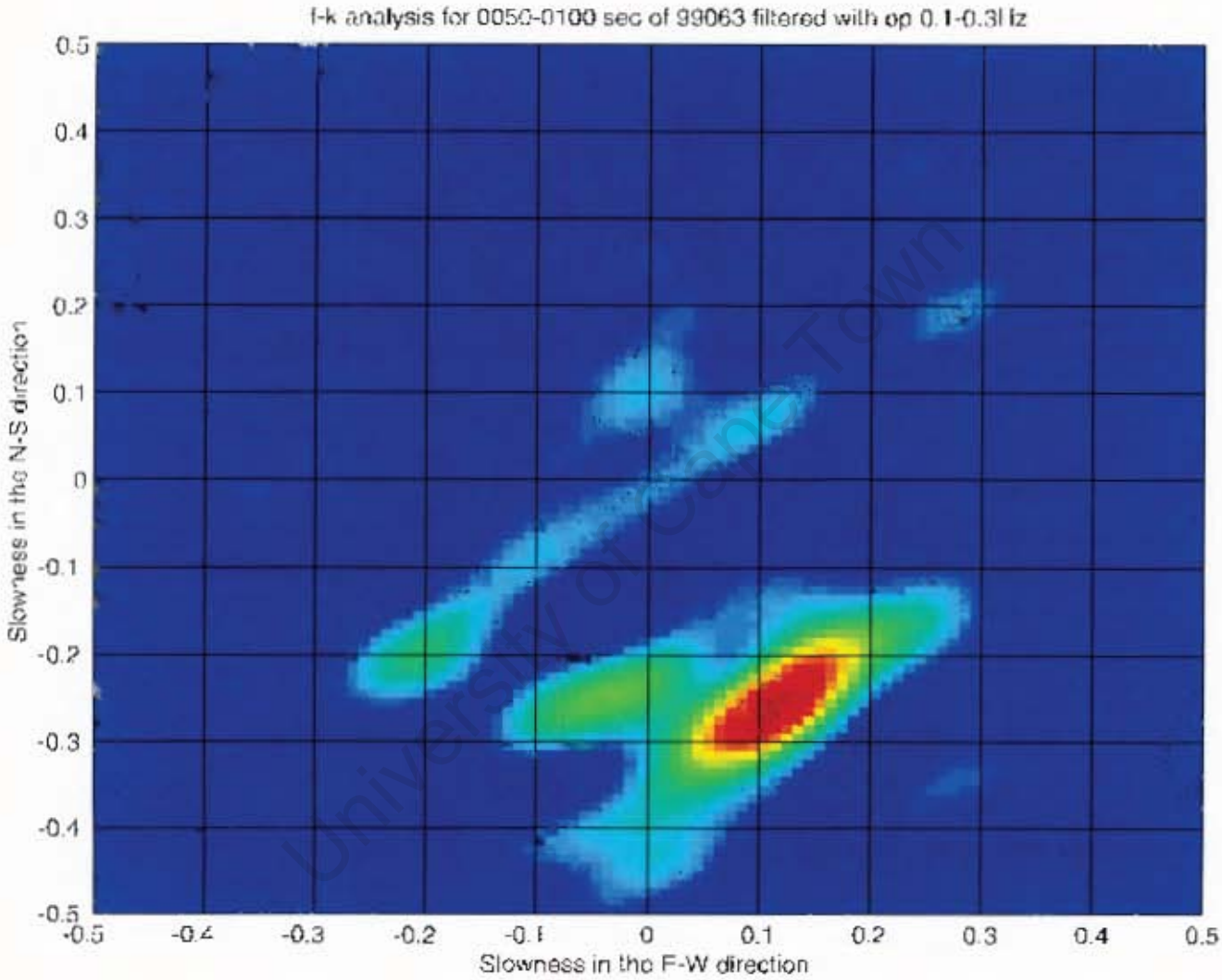

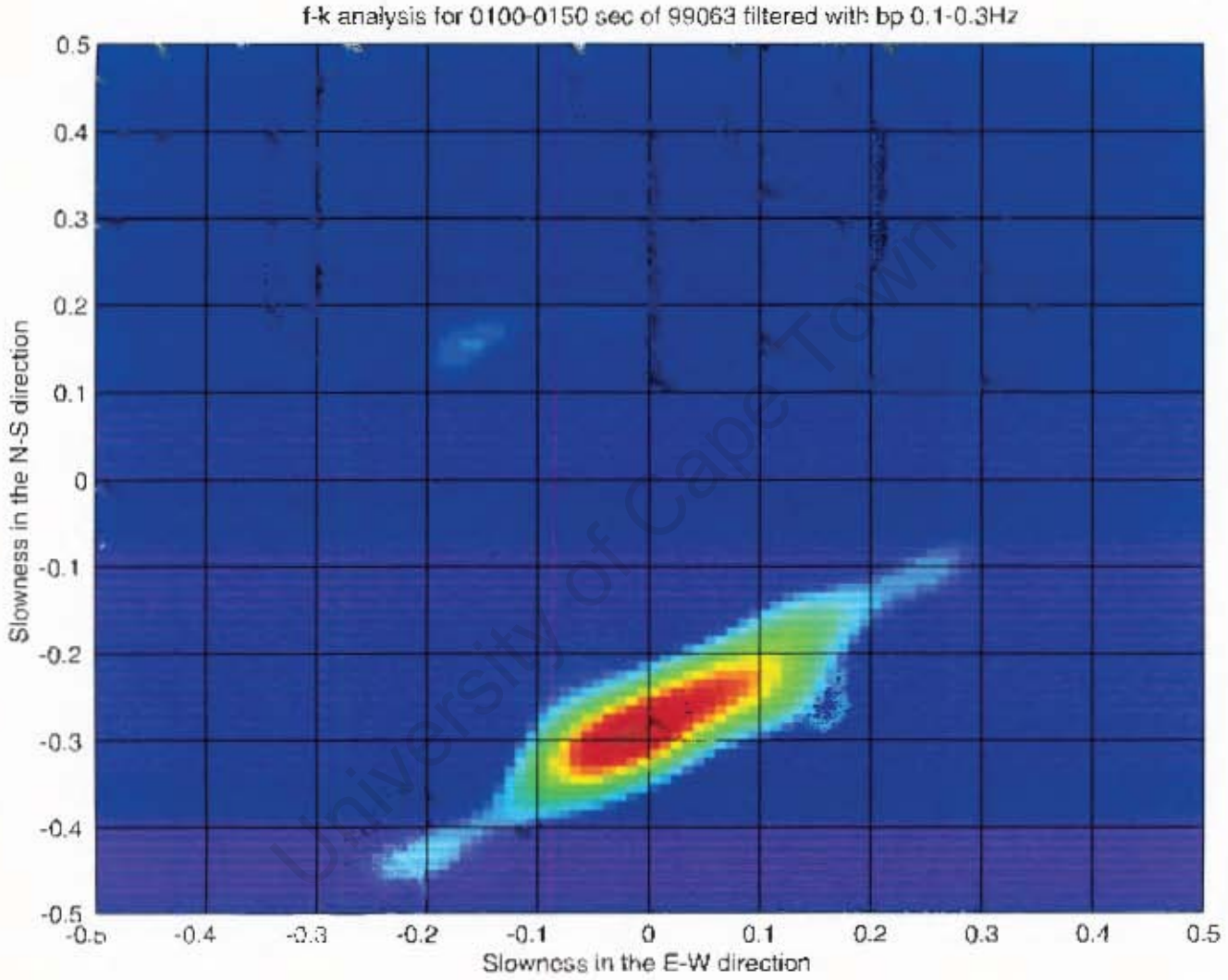

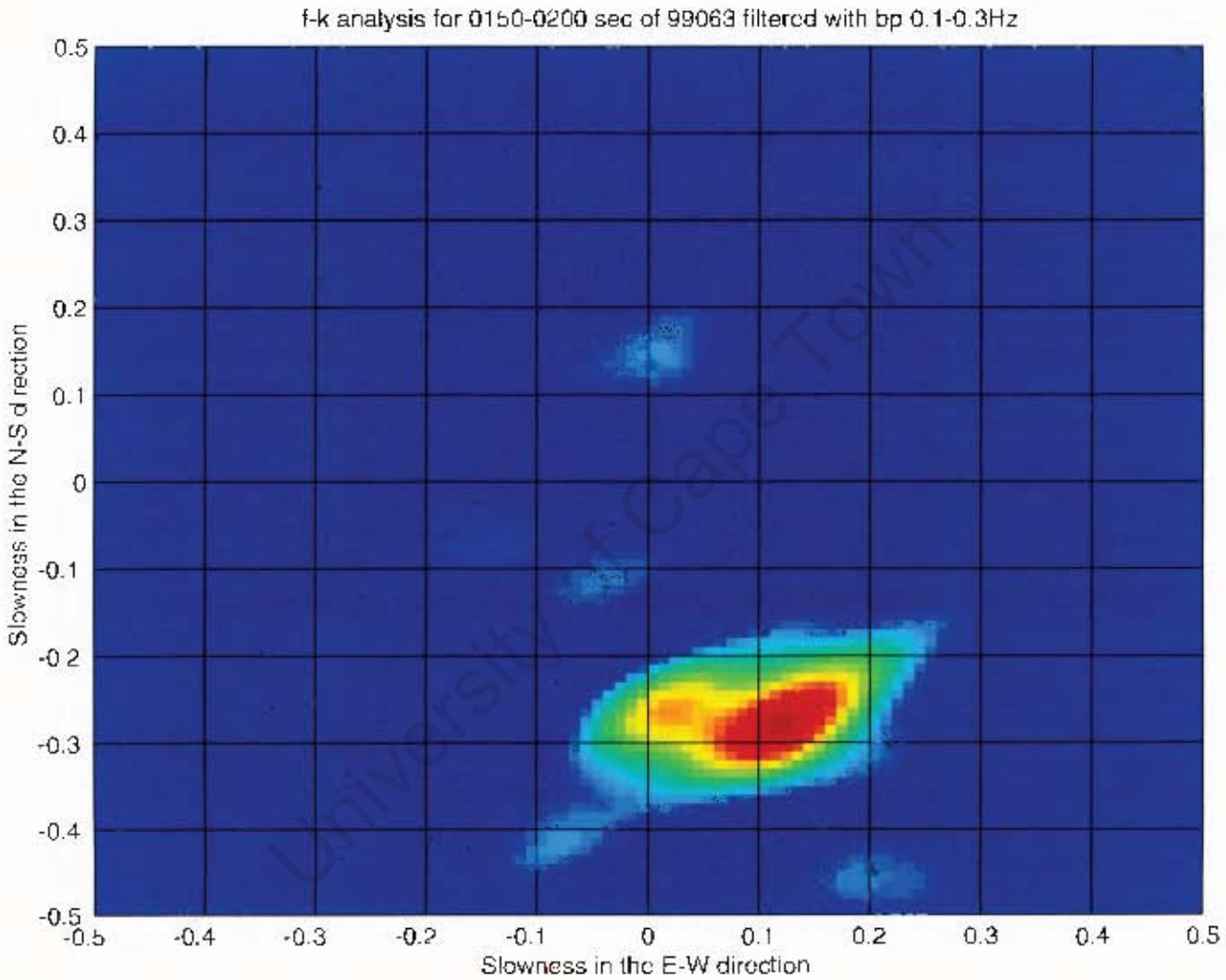

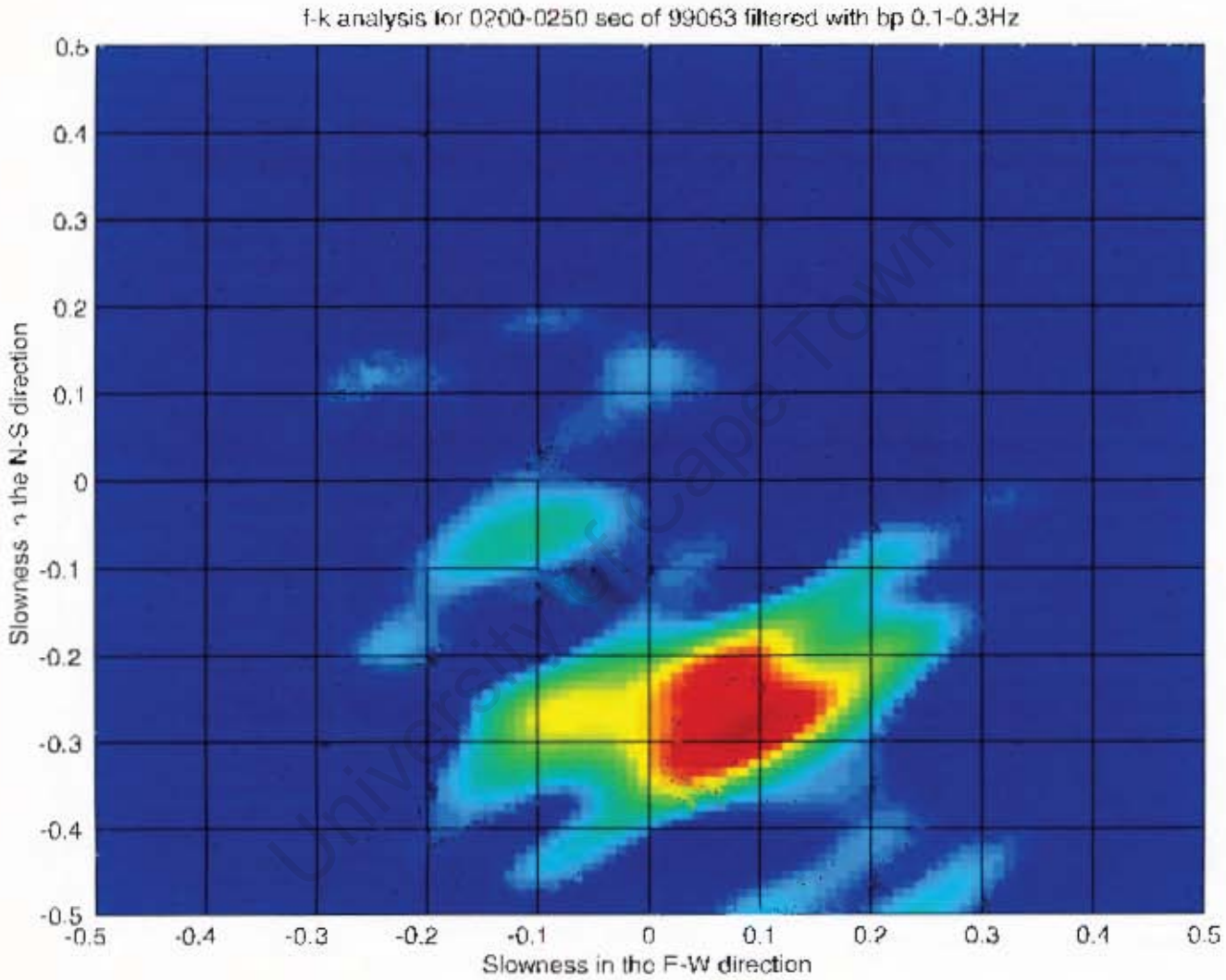

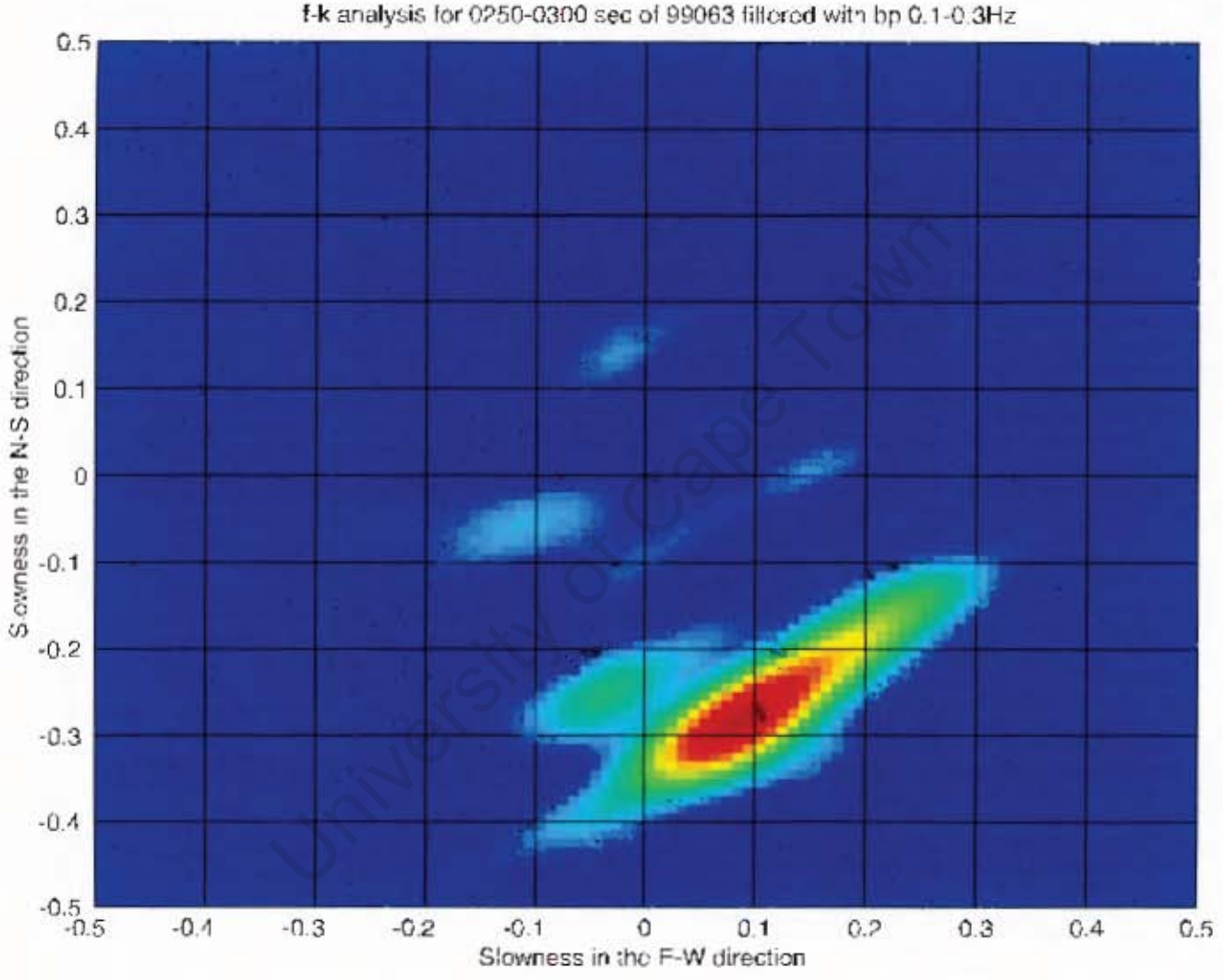

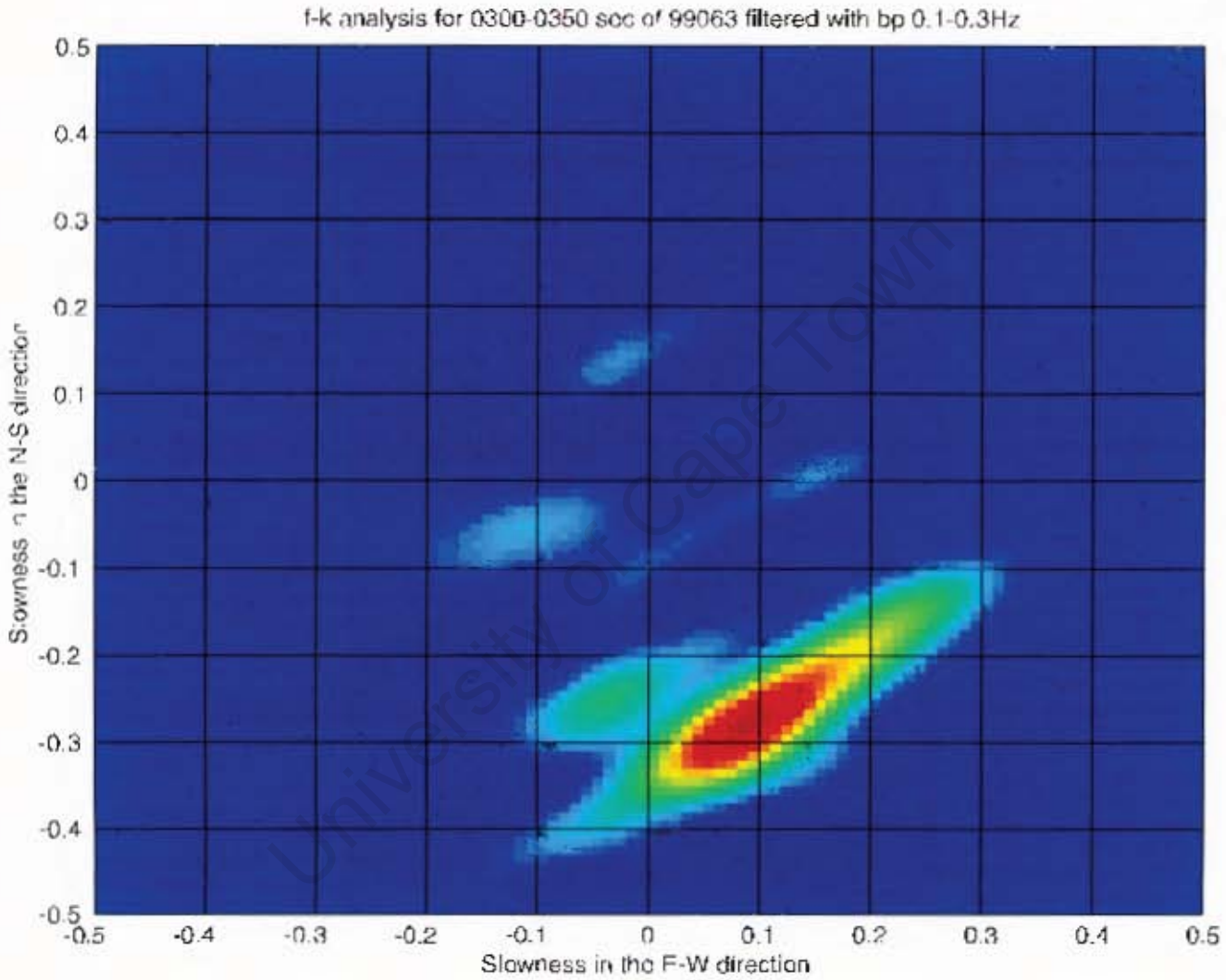

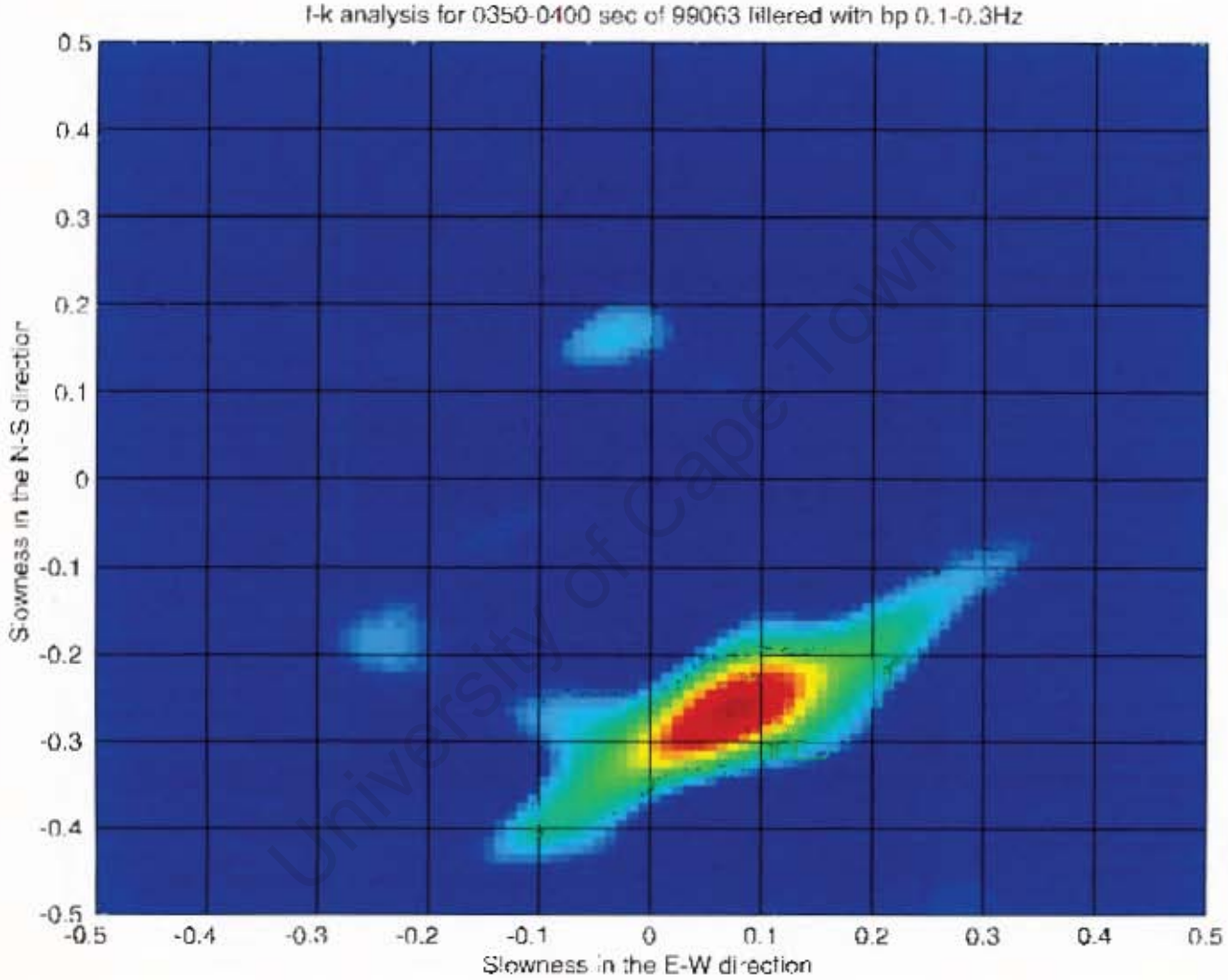

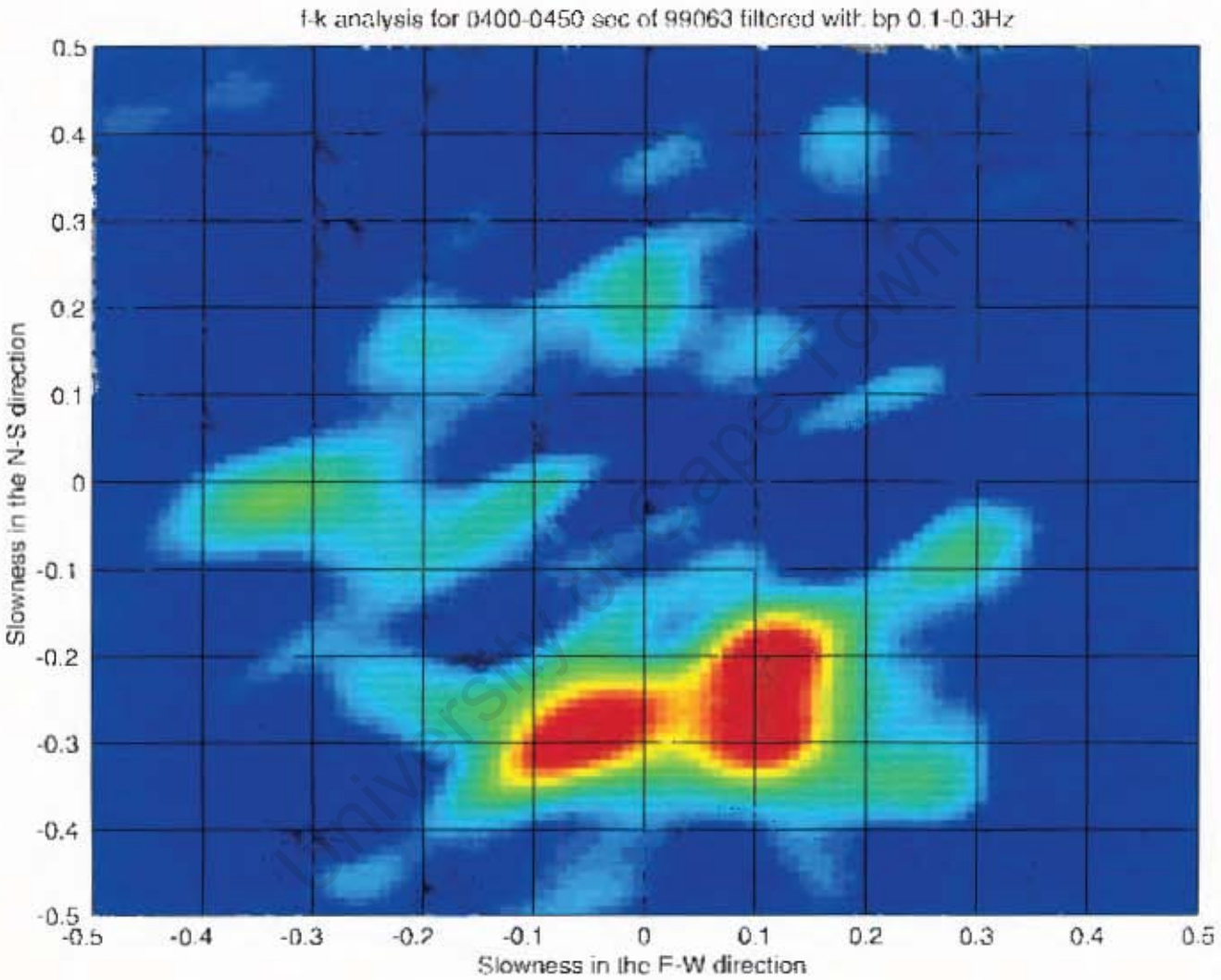

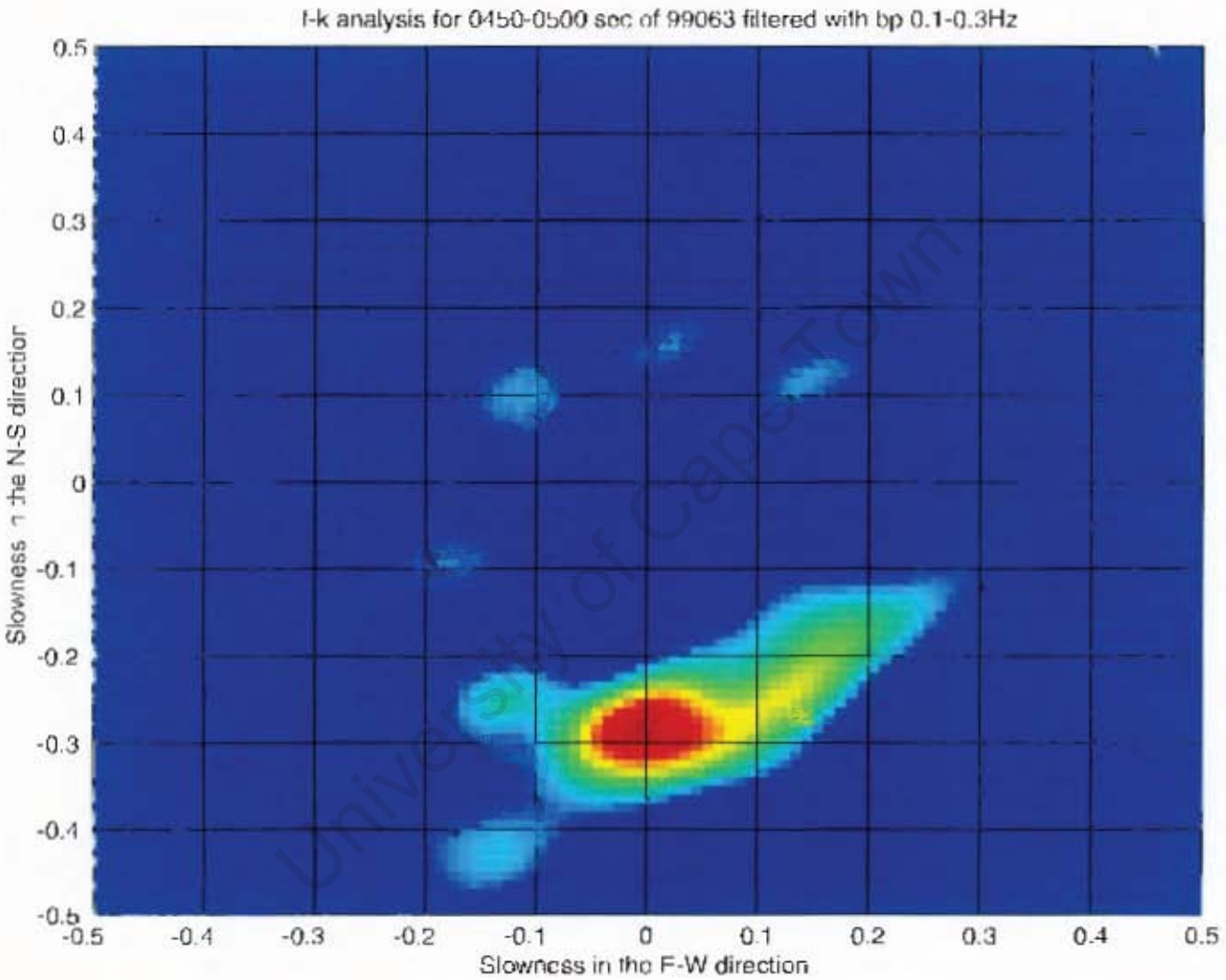

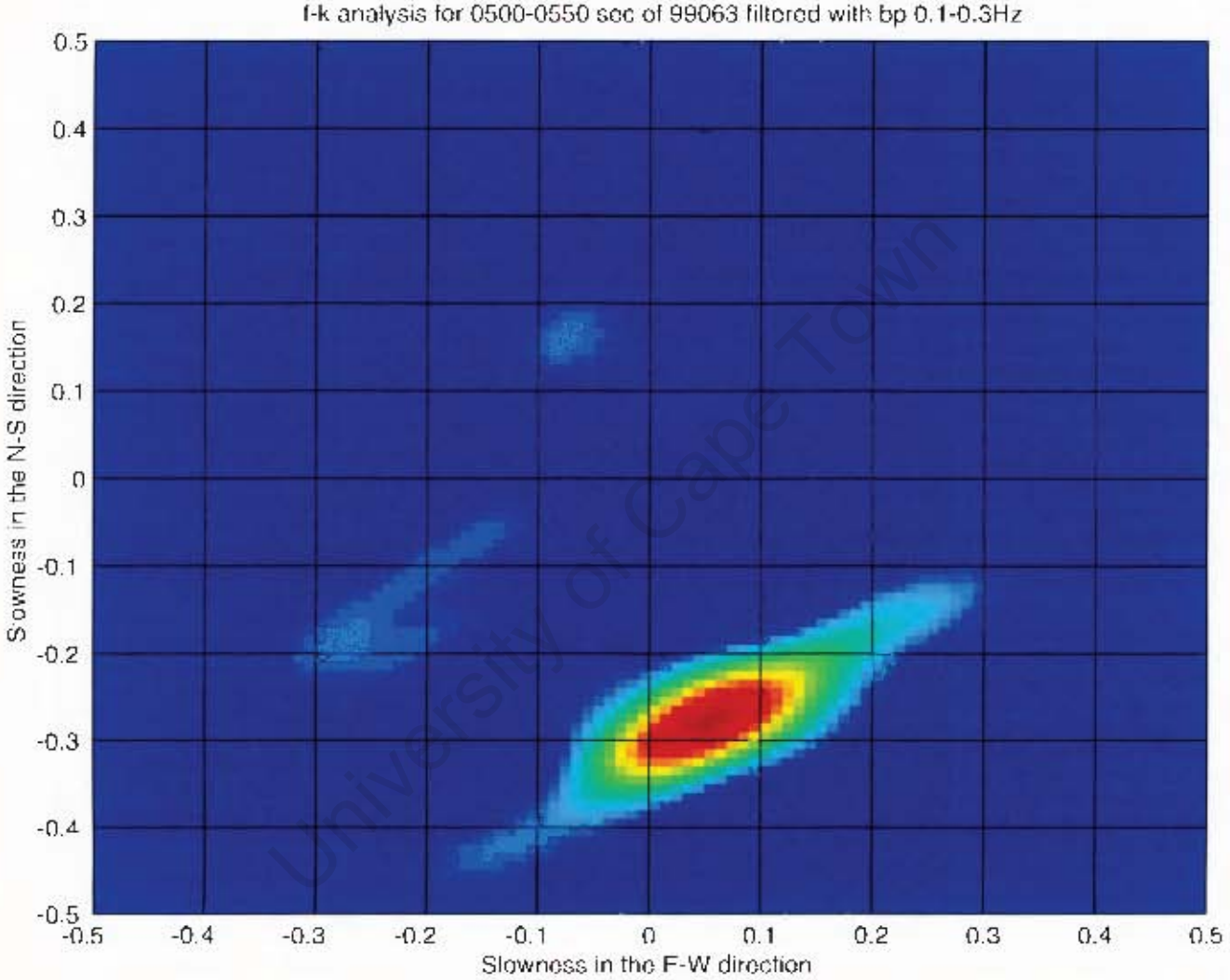

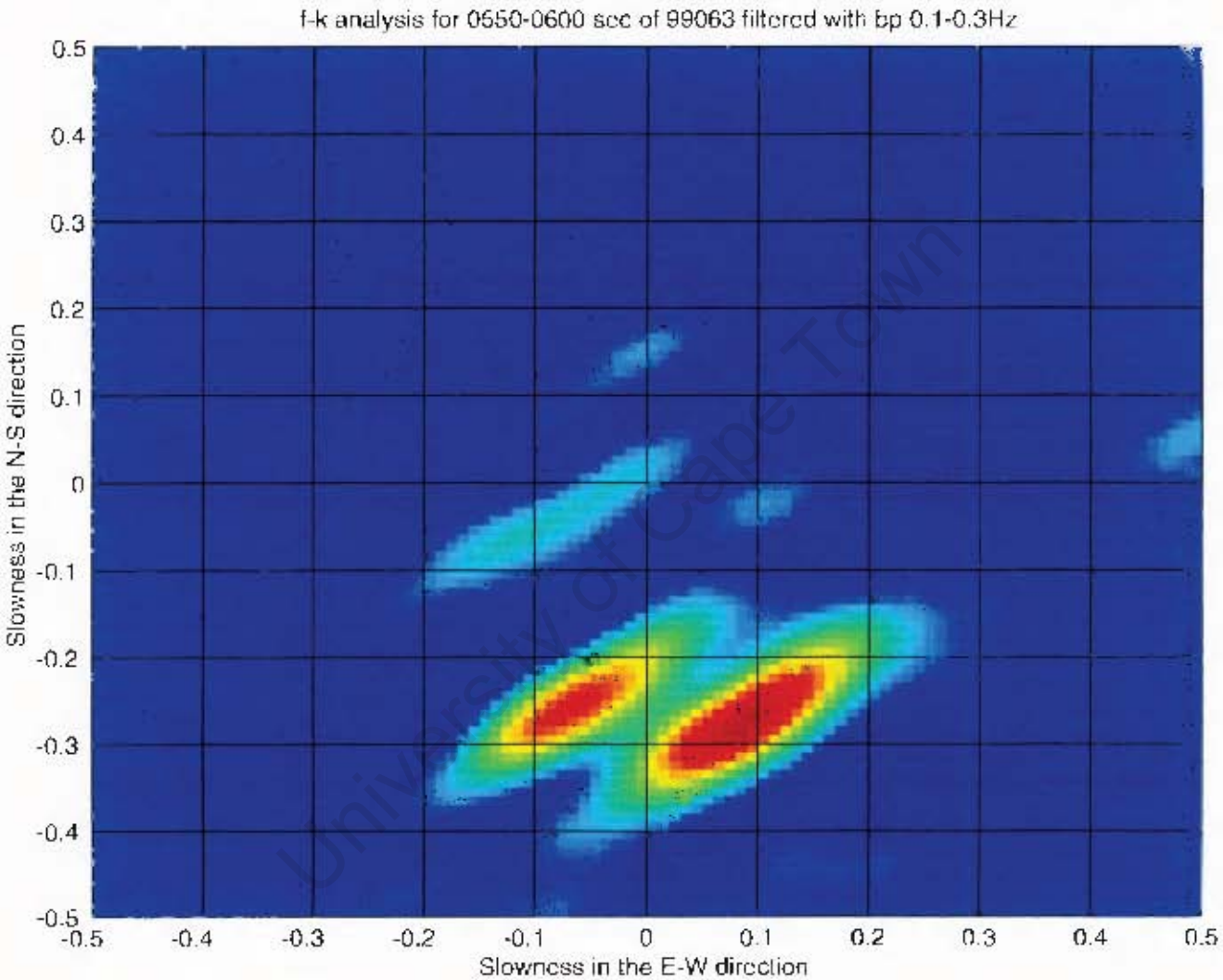

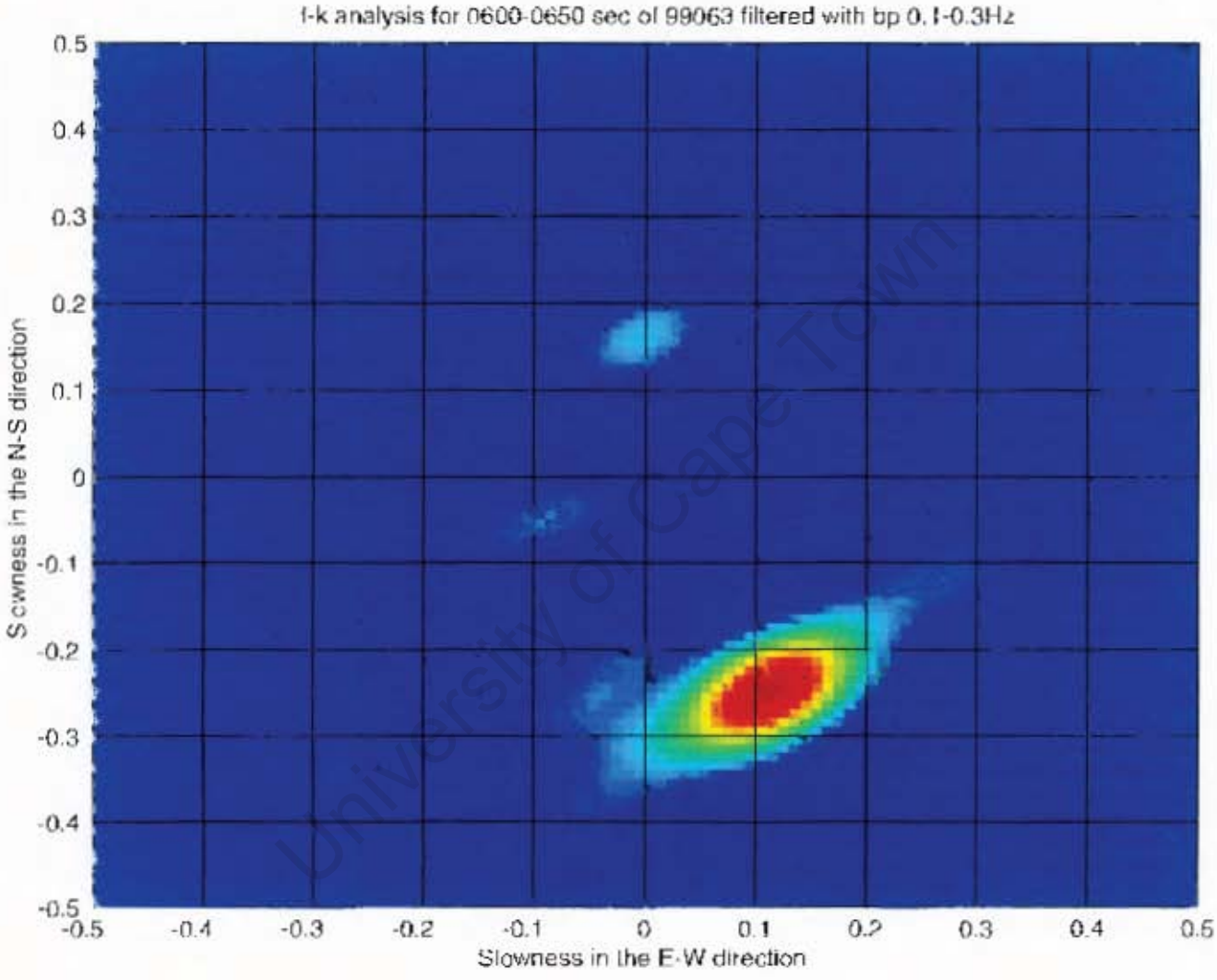

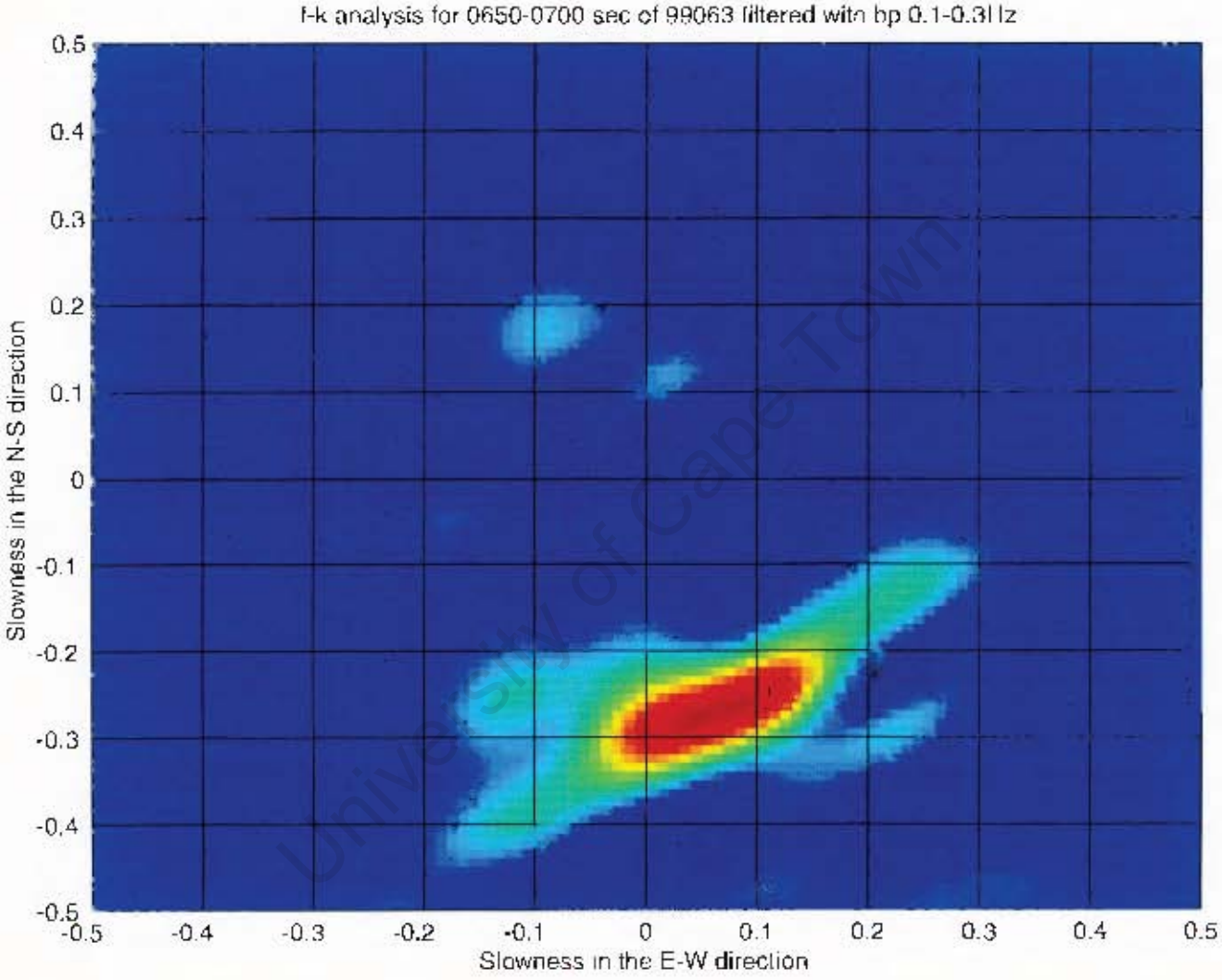

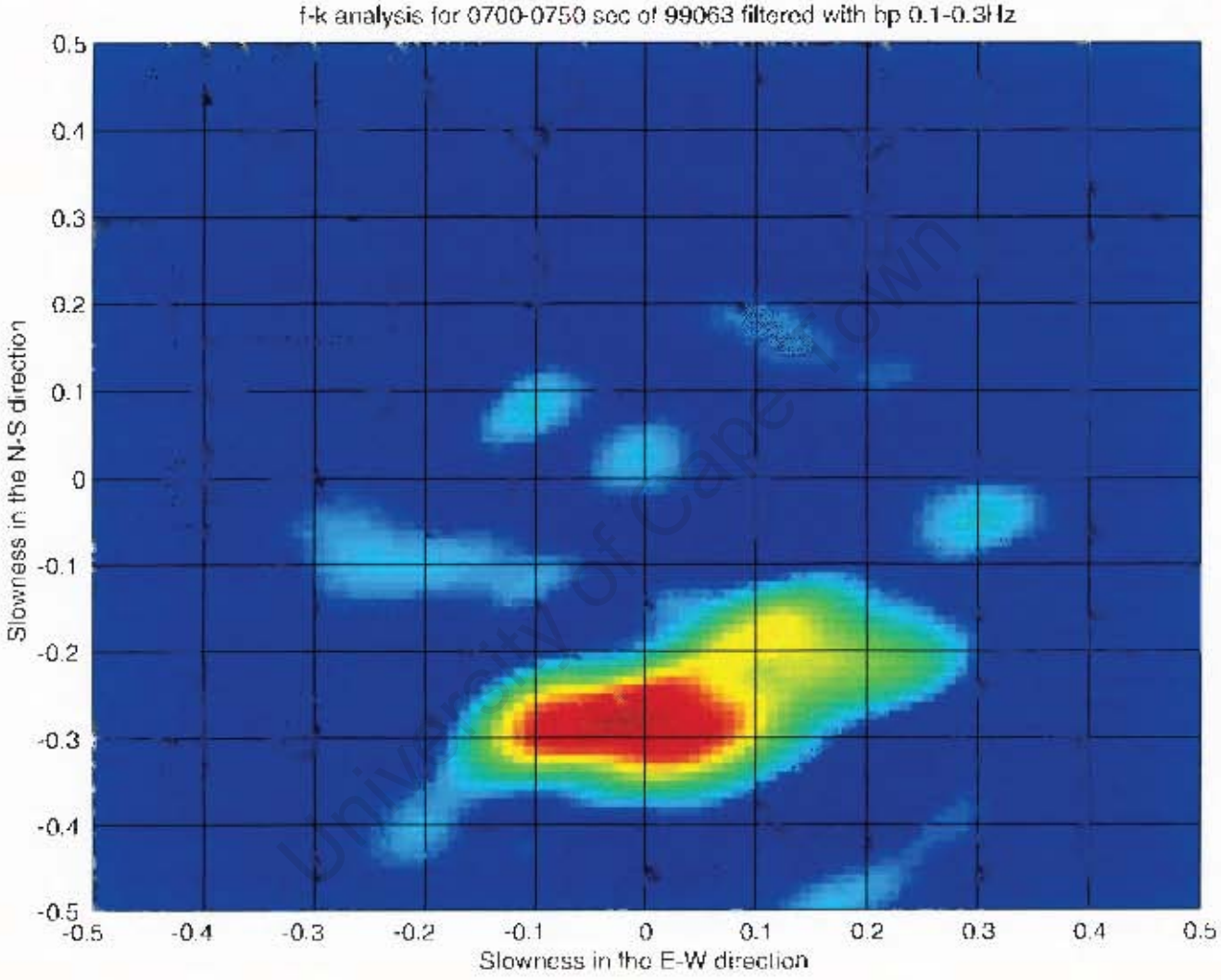

Appendix F

Particle motion graphs for the two identified surface waves.

0.05-0.1 Hz frequency band
time window: 0-30 seconds

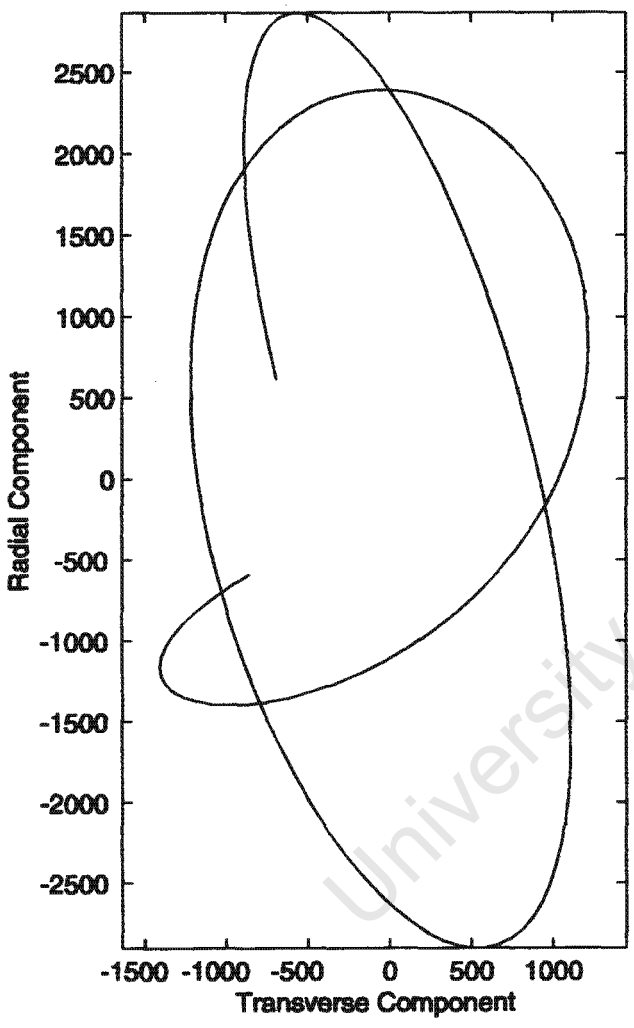

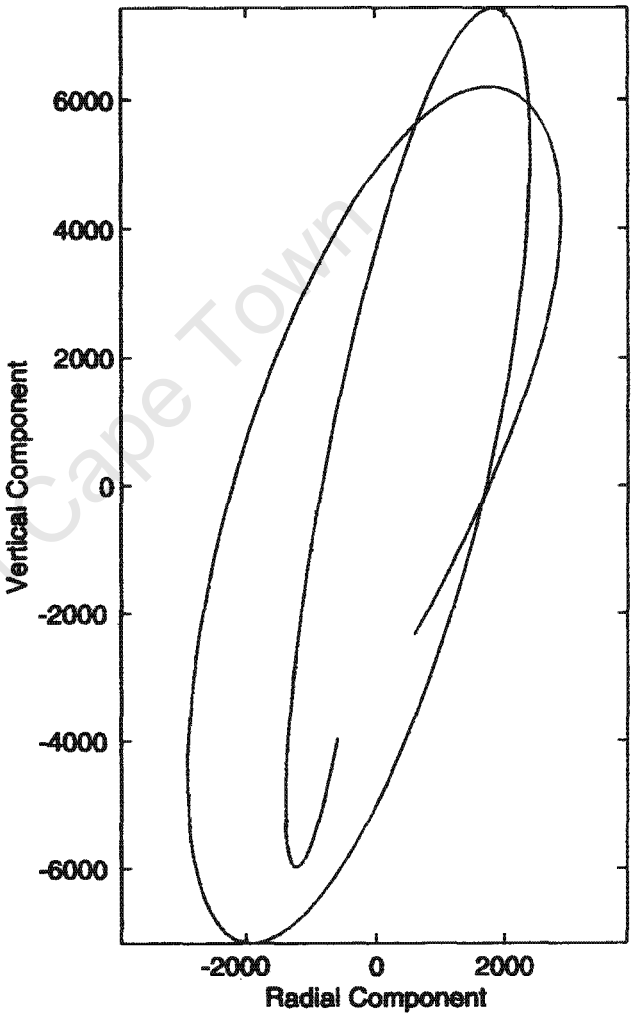

0.05-0.1 Hz frequency band
time window: 120-150 seconds

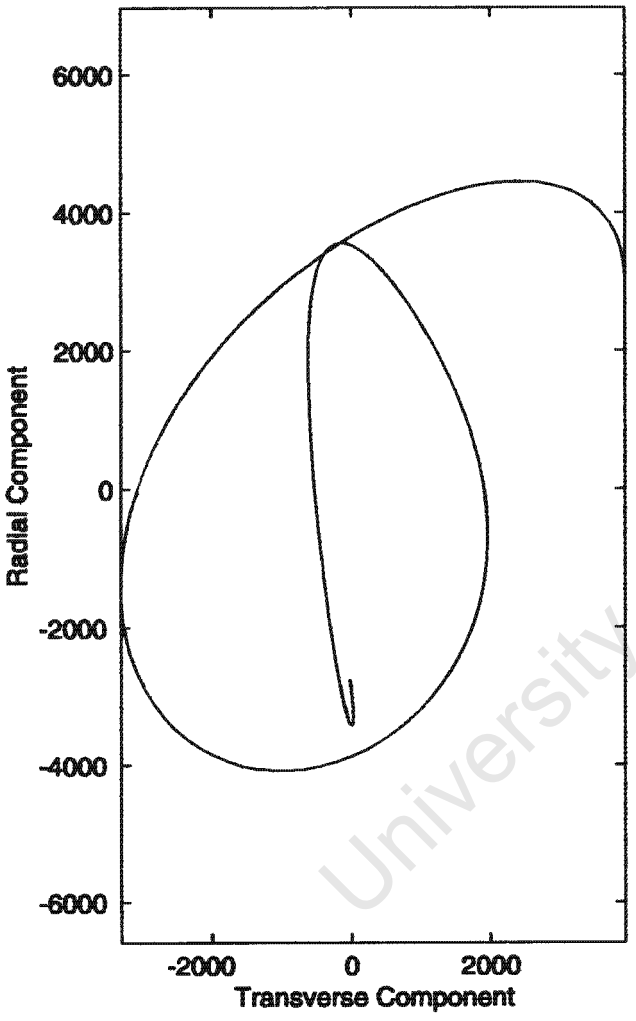

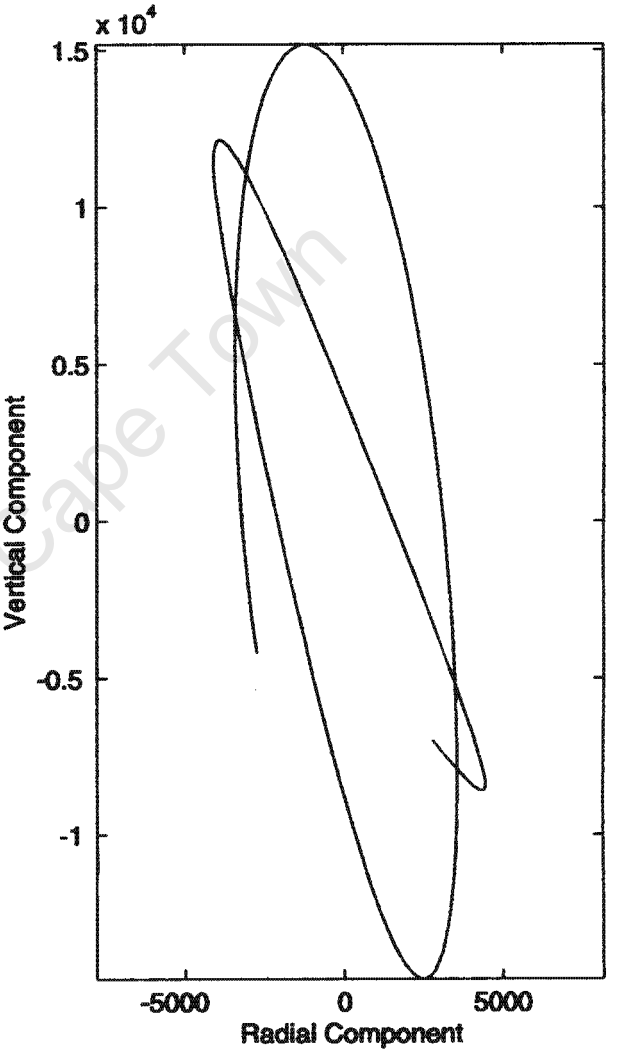

0.05-0.1 Hz frequency band
time window: 150-180 seconds

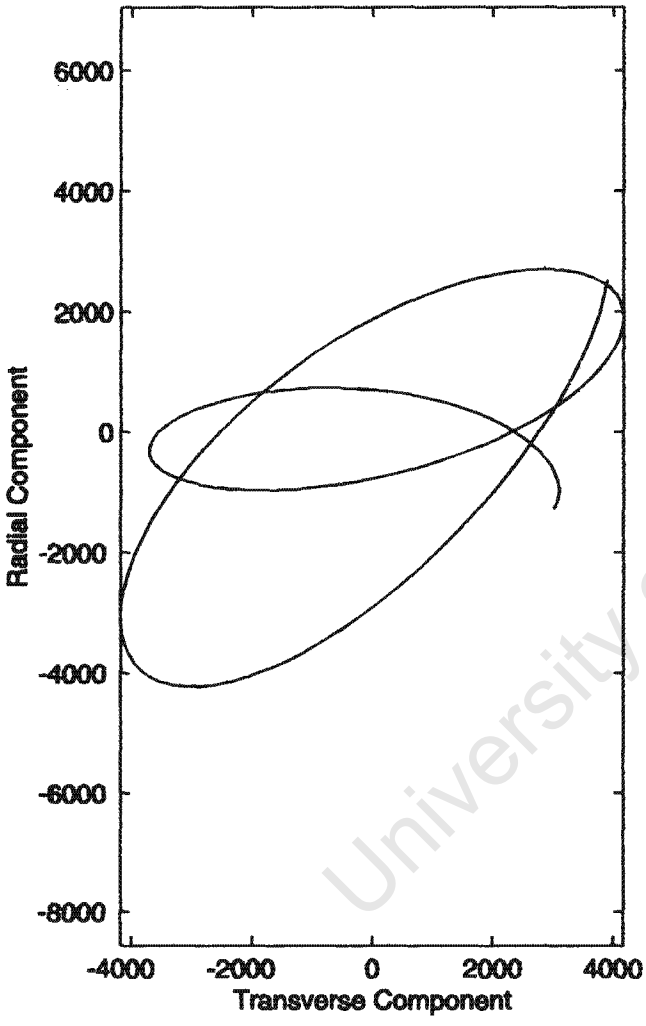

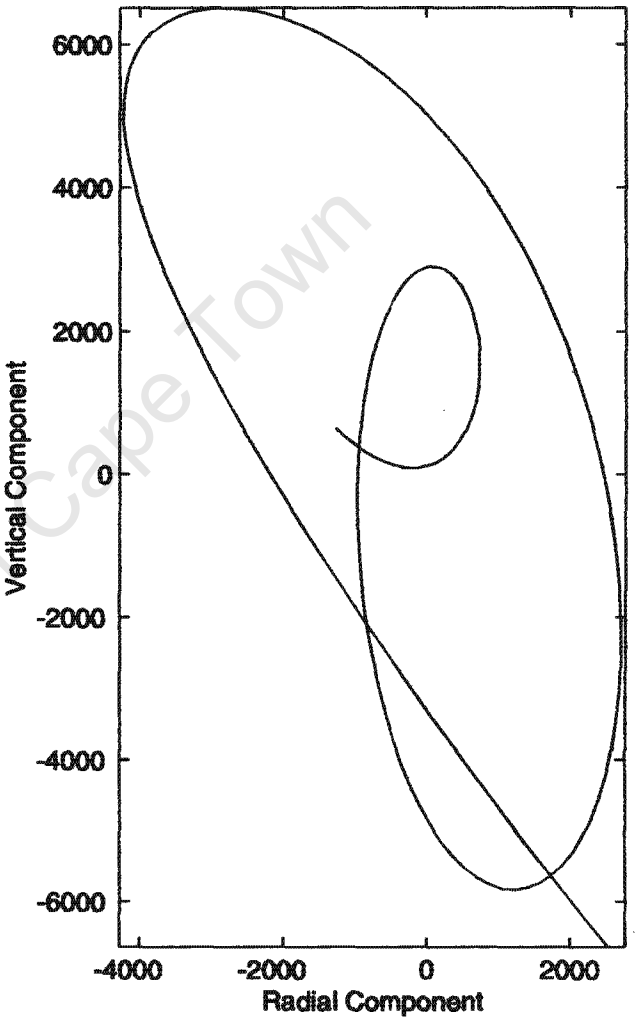

0.05-0.1 Hz frequency band
time window: 180-210 seconds

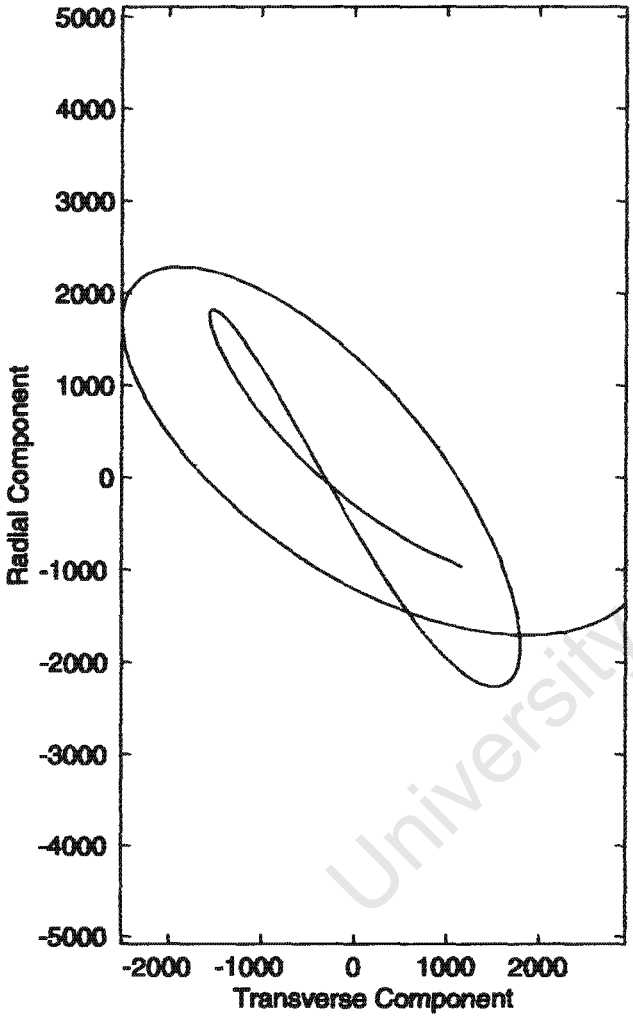

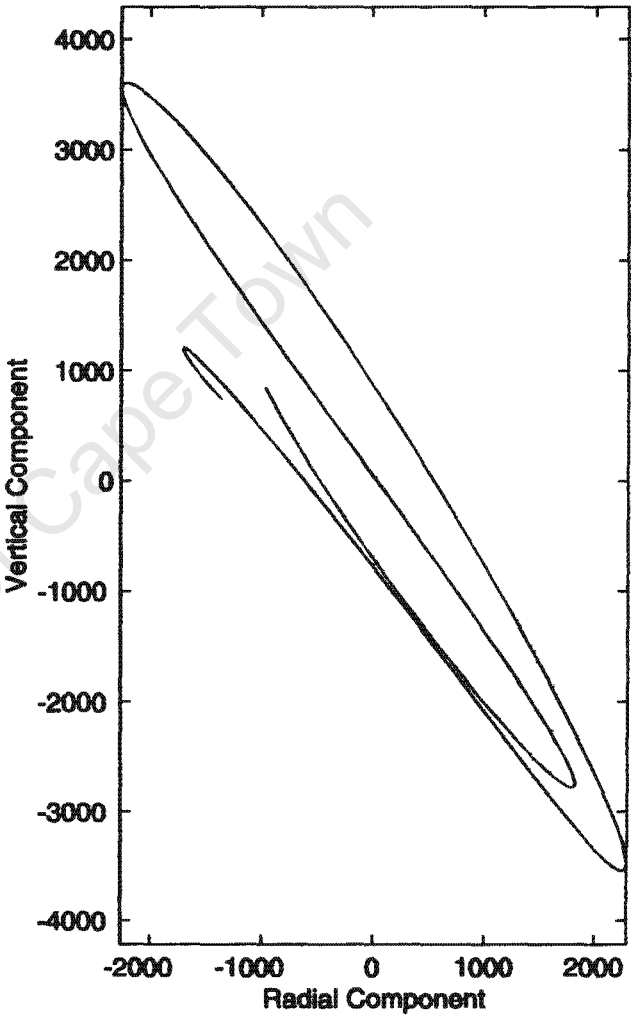

0.1-0.3 Hz frequency band
time window: 15-30 seconds

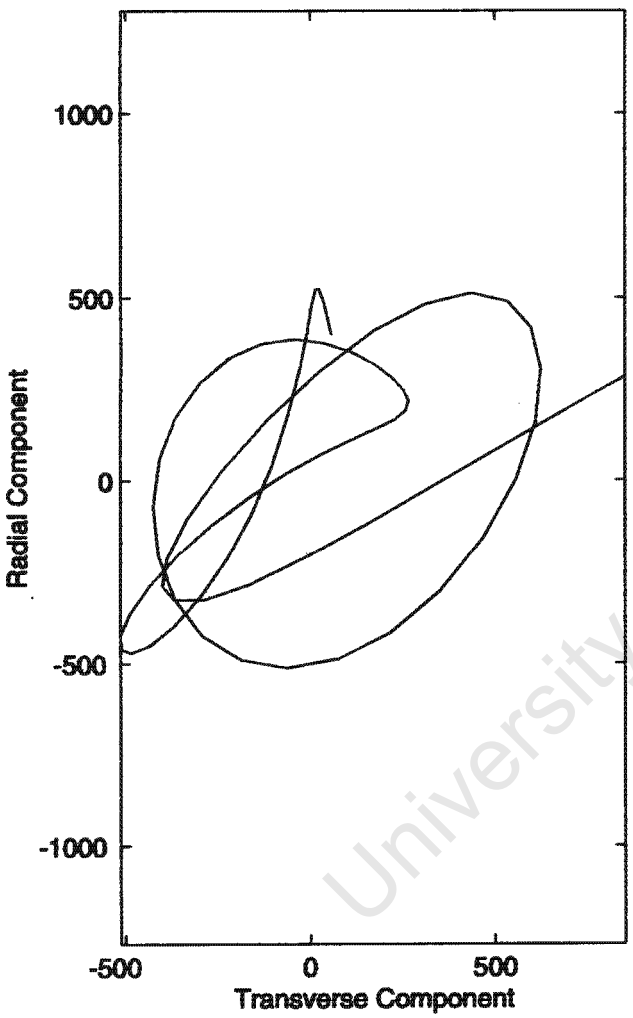

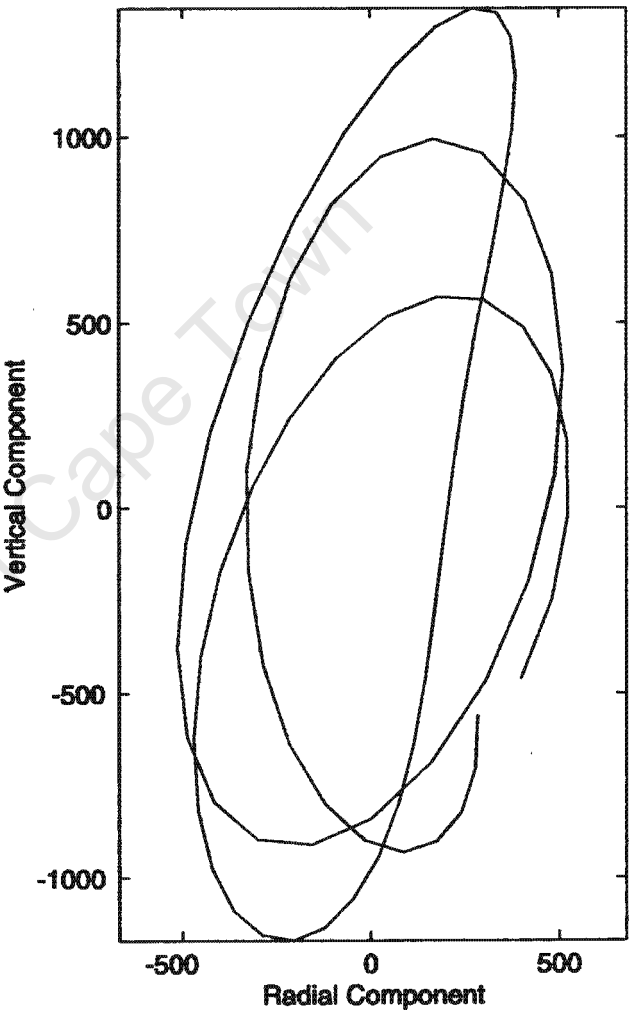

0.1-0.3 Hz frequency band
time window: 250-265 seconds

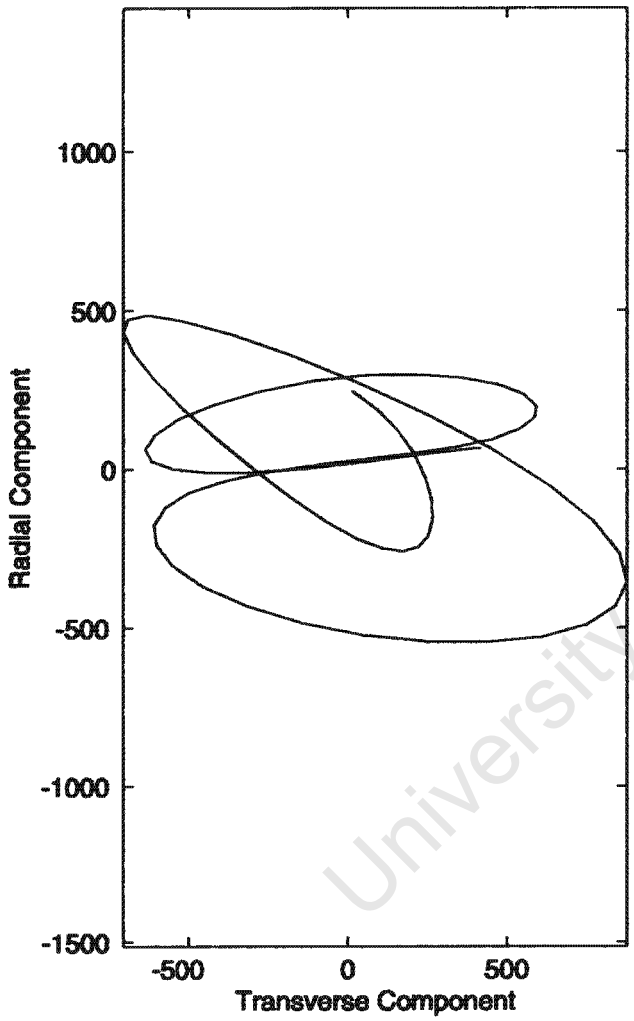

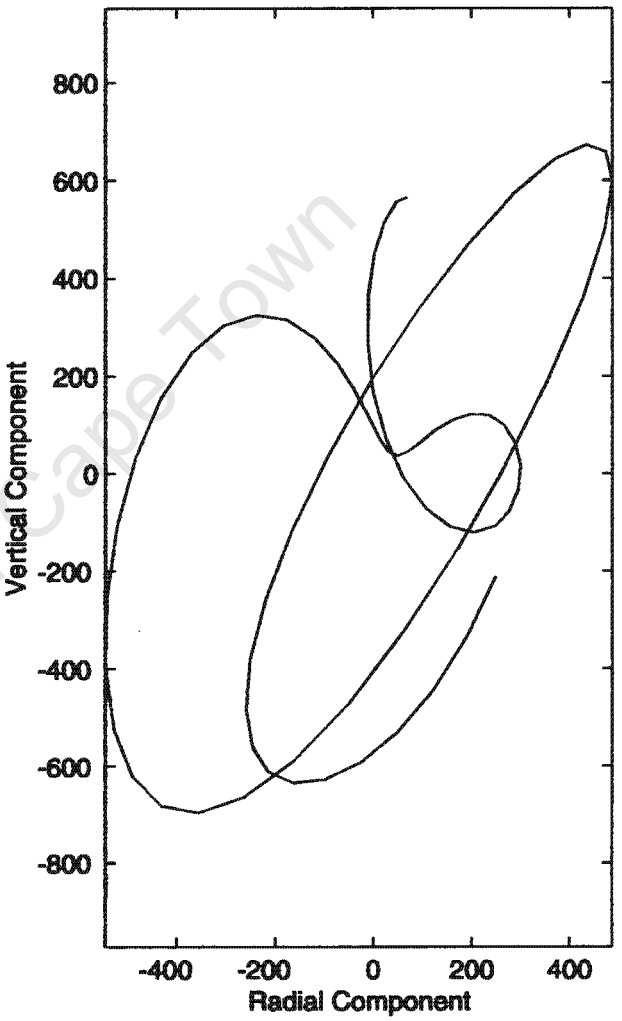

0.1-0.3 Hz frequency band
time window: 265-280 seconds